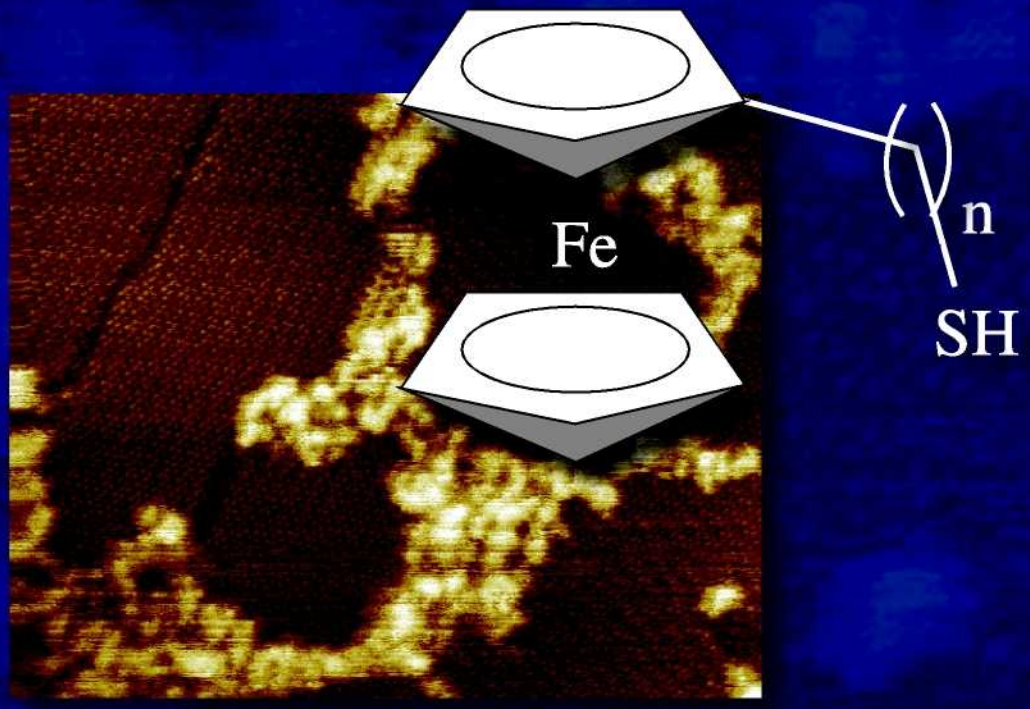

Ferrocenes as Potential Building Blocks for Molecular Electronics

Self-Assembly and Tunneling Spectroscopy

Lars Müller-Meskamp

Mitglied der Helmholtz-Gemeinschaft

JÜLICH
FORSCHUNGSZENTRUM

Schriften des Forschungszentrums Jülich
Reihe Information / Information Band / Volume 1

Forschungszentrum Jülich GmbH
Institut für Festkörperforschung (IFF)
Elektronische Materialien (IFF-6)

Ferrocenes as Potential Building Blocks for Molecular Electronics Self-Assembly and Tunneling Spectroscopy

Lars Müller-Meskamp

Schriften des Forschungszentrums Jülich
Reihe Information / Information Band / Volume 1

ISSN 1866-1777 ISBN 978-3-89336-509-8

Bibliographic information published by the Deutsche Nationalbibliothek.
The Deutsche Nationalbibliothek lists this publication in the Deutsche Nationalbibliografie; detailed bibliographic data are available in the Internet at http://dnb.d-nb.de.

Publisher and Distributor:	Forschungszentrum Jülich GmbH Zentralbibliothek, Verlag D-52425 Jülich phone:+49 2461 61-5368 · fax:+49 2461 61-6103 e-mail: zb-publikation@fz-juelich.de Internet: http://www.fz-juelich.de/zb
Cover Design:	Grafische Medien, Forschungszentrum Jülich GmbH
Printer:	Grafische Medien, Forschungszentrum Jülich GmbH
Copyright:	Forschungszentrum Jülich 2008

Schriften des Forschungszentrums Jülich
Reihe Information / Information Band / Volume 1

D 82 (Diss., Aachen, RWTH, 2007)

ISSN 1866-1777
ISBN 978-3-89336-509-8

The complete volume is freely available on the Internet on the Jülicher Open Access Server (JUWEL) at http://www.fz-juelich.de/zb/juwel

Contents

Acknowledgements

During my work on this thesis, I received support and motivation from many people. Without them, this thesis would not have been possible. I would like to thank all of them.

Prof. Rainer Waser for providing me the chance to work on this interesting topic, for his enthusiasm and for creating a stimulating environment for research within his institute.

Prof. Ulrich Simon for his interest in this work, for providing the molecules for the experiments and being the co-examiner.

Dr. Silvia Karthäuser, my supervisor, for her inspiration and enthusiasm. I owe a lot to her contribution of time, motivation and support.

Dr. Björn Lüssem for countless hours spent together in front of the STM and in discussions, learning new things about the experiments.

Christina Lennartz for her successful cooperation, large contribution and everyday motivation.

Prof. Krzysztof Szot for his help and scientific support.

Dr. Melanie Homberger, Dr. Serguei Prikhodovski, Jutta Kiesgen and Birgit Hahn for the collaboration within the IFMIT framework and providing the molecules for the experiments.

Dr. Nicolae Atodiresei for his collaboration and explanations.

Prof. Ulli Englert for the x-ray crystallographic measurements.

Prof. Szade for the XPS measurements.

Hans Haselier for evaporating countless gold electrodes.

The IFF workshop and the IFF construction; Kurt Hirtz, Herbert Feilbach and their teams for their help with the construction of the new vacuum system.

Janet Carter-Sigglow for language support

My friends and colleagues: Peter Kowalzik, Dennis Bräuhaus, Patrick Neubauer, Helge Lüders, Dr. Andreas Rüdiger, Serge Röhrig, Dr. Stephan Kronholz, Maria Garcia, Manfred Gebauer, Hermann Bierfeld, Marcel Gerst, Holger John and everyone else at the institutes, for their help and support.

Last not least I would like to thank my parents and family for everything and Monika Brechtken for her patience and support.

1 Organic molecules for information processing

1.1 Perspectives, applications and present status

Information in all its different forms is obviously an omnipresent aspect of modern life. The advances in information storage, processing and manipulation have propelled our society into the information age and made the world a "global village" with wireless broadband communication, internet companies, and information processing devices in everybody's hand. These considerable changes in the last few decades have been driven by the evolution of information technology. The integrated circuit and the modern microprocessor started their technological revolution with the principles of von Neumann, 1945 [1] and the invention of the transistor by Shockley, Bardeen and Brattain in 1948 [2]. Highly specialized computing machines the size of small houses gradually turned into powerful hand-held devices for everyday use and will evolve further into smaller and more powerful devices, creating an environment with ambient intelligence. The task of finding information about a specific subject has changed into the task of selecting relevant information from the huge amount of data available anytime. This technical evolution proceeding at an unparalleled pace continuously demands for more processing power, additional storage capacity and new smart concepts, extending the range and intelligence of the systems. In the future, the interdiffusion of the information sphere and the real world in the form of more and more people spending time in purely virtual space, as well as robots, smart sensors and actuator systems interacting with reality, will continue the demand for processing power.

The technological evolution of modern integrated circuits has driven the latest generation of silicon CMOS ICs into extreme dimensions. The reduction of the power dissipation per logical operation is one of the

most important goals for future processor generations, allowing a higher integration of the circuits and improving the useability for mobile applications. The feature size for the latest experimental devices and in particular the gate oxide thickness, have reached dimensions that can be expressed as integer multiples of a few crystalline unit cells and reach the fundamental limits of the materials employed. The production of these highly integrated devices has become enormously complex, resulting in extreme costs for the manufacturers. The ever increasing demand for processing power and further development of silicon technology lead to an intensifying search for alternatives and additions to the standard silicon technology, permitting a decrease in costs and power consumption, while further increasing the processing power.

One promising technology is the use of organic materials with a wide range of applications. Organics offer vast opportunities for cheap and large electronic circuits, as well as for high-performance devices, leading to a high potential for industrial applications. The advent of organic electronics came with the discovery of conducting polymers by Heeger, MacDiarmid and Shirakawa in 1977 [3], for which they received the Nobel Prize in chemistry in 2000. The technological development of organic thin films has now led to organic light-emitting diodes (OLED), which in form of OLED-displays are the first organic products to enter the market in larger numbers. Thin films of organic molecules offer a high potential for various applications. They are cheap, can be used for printed circuits and possible applications on flexible substrates or even on fabrics and in different forms not yet imagined. Therefore, the short-term goals for the application of organic thin films are cheap, large-scale electronics. However, technical development will lead to thinner films with optimized intermolecular interactions, both structural and electronic, to achieve higher performances. At a certain point, with a thickness in the range of one to several monolayers and increasingly ordered thin films, the top-down development of thin film organics will meet the bottom-up technological development starting from the properties of single molecules. The bottom-up branch in the development of organic electronics tackles technical development from the other side, starting with the smallest structures. The analytical power available for modern scientific measurements, especially the use of scanning probe microscopes, enables access to the properties of single, small molecules, down to individual atoms. Starting with the electronic and structural properties of single small molecules and progressing to ordered monolayers and other self-assembled structures, the characteristics of organic materials are explored.

The bottom-up branch of organic electronics or molecular electronics focusses on the production of building blocks for electronic devices like diodes, switches or more complex functionalities in single molecules or small assemblies [4]. A closely related activity, often pursued together with the above mentioned tasks is the creation of larger supra-molecular structures using the inherent properties of the molecules. Large-scale systems are synthesized as grid-type metal ion arrays by Lehn et al. [5] or large, macroscopic molecules of extended π-systems, which were used to form supra-molecular assemblies by Muellen et al. [6]. By supra-molecular chemistry, several molecular building blocks can be combined to form large-scale patterned surfaces, as shown for rectangular and triangular molecules linked with hydrogen bonds to form a hexagonal pattern, as reported by Rabe et al. [7]. Various molecule-substrate systems spontaneously form self-terminating, self-assembled monolayers of highly ordered structures like alkanethiols on gold, representing a first step towards the integration of ordered molecular layers with high density, quality and anisotropic behavior.
The idea of molecular electronics arouse in the famous paper by Aviram and Ratner in 1974 [8], theoretically describing a molecule with donor and acceptor parts that forms a donor-bridge-acceptor molecule with diode behavior thus representing a molecular rectifier. Reed and Tour [9] further pursued the search for functional molecules and their electrical characteristics. Voltage-controlled conductance switching of functional molecules was observed by Szuchmacher Blum et al. for different junction types [10]. An impressive system for possible applications is the complete framework set up by Stoddart, Kuekes, Williams and Heath [11]. Switchable junctions, containing rotaxane molecules, which are not the source of the switching effect [12–14], are combined to form reconfigurable cross-bar architecture together with fault-tolerant algorithms for computing and storage.

1.2 Self-assembled monolayers

Organic thin films on various substrates, such as an oil film on water, have probably always attracted people's curiosity. Starting with particle and oil films on water in 1917 [15], the pioneering work by I. Langmuir and K.B. Blodgett [16, 17] provided for the first time enabled an understanding and thus led to the manufacture of organic layers with a defined thickness of a discrete number of molecular monolayers, so-called

Langmuir-Blodgett films (LB films). Early experiments already showed interesting surface properties, e.g. a high hydrophobicity for stearic acid on copper, which was studied as a condensation promoter in the era of the steam engine [18]. Later monolayer deposition from solution was discovered by Bigelow et al. for long-chain alcohols [19] in 1946. In 1978, spontaneously ordered monolayers of silanes were studied by Sagiv and Polymeropoulos [20], for which the term "self-assembly" was used for the first time [21]. Complex organic layers are also a very basic principle in nature, e.g. lipid bilayers forming cell membranes represent an ordered molecular bilayer, studied in modern biology. Today, self-assembly is a widely investigated topic in modern science. The fascinating process of spontaneously emerging order in the form of self-assembled monolayers has been shown for a variety of molecule-substrate systems. These include alkanoic acids on AlO_x [22], selenols and alkanethiols on Au [23,24], alkanethiols on Pd [25], Cu [26], on Ag [27,28], on GaAs [29], on Hg [30] and silanes on hydroxylated Si surfaces, [23,24] as well as many more.

All these molecule-substrate systems require a few basic preconditions. The most important condition for the formation of molecular order is the interaction between the molecules via van der Waals forces, $\pi - \pi$ interactions, hydrogen bridges or other intermolecular forces. In the case of SAMs, the molecules can be divided into three functional parts. The large, central part of the molecule, responsible for the molecule-molecule interaction and for most of the intrinsic electronic properties, is called the molecule body. The bottom group chemisorbs to the substrate and contributes to the structural order by substrate-molecule interactions. These become especially important for weaker intermolecular interactions as in the case of very short chain alkanethiols like methylthiol. The bottom group also determines the coupling of the molecule to the substrate and therefore defines the charge transfer properties between molecule and substrate. The top group determines the surface properties of the monolayer thus offering a wide range of possibilities. The surface can be hydrophilic or hydrophobic, it can provide a chemically active surface for template growth of thin films or provide catalysts, enzymes or active sites for chemical surface reactions or provide many other surface functionalities. In addition, the top group is crucial for interface properties and charge transfer to a top electrode of any kind. Self-assembled monolayers present a possible way of integrating molecular properties into larger-scale electronics. They provide the opportunity of employing asymmetric molecules and offer the chance to produce layers with well-defined structural and electrical properties.

SAMs can provide customized functional surfaces, used as catalysts, sensors or as substrates for the deposition of various materials. Aromatic thiols act as a high-resolution resist for surface patterning [31]. Functionalized organic layers also offer great opportunities in combination with nanoparticles, creating regularly spaced assemblies with tunable properties. In this way, self-assembled monolayers represent a powerful tool for future applications of organic molecules in industry.

1.3 Outline of the thesis

Organic materials with macroscopic material properties are already being successfully employed in industry. To extend the possible fields of application to smaller scales and higher performances, our understanding of properties on the nanoscale has to be increased. The construction of larger scale functional units from small building blocks by self-organization represents a powerful tool for the fabrication of circuits using the full potential of molecular electronics. To create a toolbox for nanoconstruction, we have to study different kinds of building blocks and how they can be combined [32]. Well-behaved molecular insulators such as alkanethiols, semiconducting molecules with π systems like benzoic or terephthalic acid and charge transfer complexes like ferrocenes are investigated in this thesis as potential molecular building blocks. In order to glue or click them together, the molecular interactions are studied. The van der Waals forces in alkanethiol monolayers, the interaction of π systems in benzoate monolayers or the interactions between ferrocenes represent strong forces which could be used for molecular assembly. The properties of the chemical bonds between copper and carboxylate or sulfur and gold represent possibilities of coupling them to metal electrodes. The behavior of a free carboxylic acid moiety on top of a terephthalic acid monolayer enhances our understanding of how molecules can be further combined. The structural and electronic properties of the above mentioned systems are studied in the form of pure and mixed monolayers, forming ordered structures on crystalline substrates. To gain insight into true nanoscale properties the molecules are studied by STM, which has the highest resolution available for scanning probe microscopes.

1.3.1 Substrates

Clean, crystalline surfaces with a low surface roughness have to be provided to enable high-resolution studies of a self-assembled monolayer. The fabrication of Au(111) thin films on mica substrates by electron-beam deposition in vacuum is described and discussed. As a new material system, copper crystals with a (110)-surface are prepared. The oxygen adsorption on the surface in vacuum is studied by XPS to establish a process window for deposition and measurement. STM measurements are performed to optimize an argon sputtering and annealing procedure resulting in clean surfaces with large terrace sizes.

1.3.2 Construction of a new UHV system

A new vacuum experimental system is constructed to ensure a complete in vacuo processing of the samples, increasing the purity and the quality of the monolayers. The new system features a detached chamber for vapor phase deposition of organic molecules, a load lock chamber, a storage chamber and a measurement chamber. It integrates facilities for sample heating, sample cleaning by argon sputtering, tip heating and tip sputtering.

1.3.3 Self-assembled monolayers of alkanethiols

Alkane chains represent the ultimate molecular spacer. They can be used to separate functional parts of a larger molecule, to form an ordered spacer layer and to spatially stabilize assemblies. Alkanes are easy to synthesize, they are chemically inactive and can be produced in the desired lengths. As of alkanethiols on Au(111), they form ordered, insulating layers with characteristic surface structures. Even though alkanethiols have been extensively studied, the origin and exact properties of the surface corrugation and thereby the layer structure still leave open questions.

1.3.4 Structural and electrical properties of ferrocenes

Ferrocene is a very stable electro-active, metal-organic complex, offering interesting molecular properties for incorporation into organic systems.

Whereas its application as a spin valve [33] is certainly more exotic, ferrocene can act as a donor in larger donor/acceptor systems, forming charge transfer complexes. Before larger systems can be studied, the electronic and structural properties of the ferrocene moiety have to be investigated by STM. Ferrocenes and chemisorbed monolayers of them have been studied by various techniques, but no data regarding the local structure of a chemisorbed monolayer is available in the literature. Therefore in the present work the exact structure of the ferrocene layers had to be determined before spectroscopic measurements could be performed. For the different ferrocene derivatives, ordered monolayers and mixed structures are prepared and characterized, leading to a large number of newly discovered structures. For the first time, a current-decay constant is assigned to the ferrocene moiety by current-distance spectroscopy and the charge transfer behavior is studied by voltage-dependent measurements.

1.3.5 Self-assembled monolayers of carboxylates on copper

Carboxylates on Cu(110) represent an interesting alternative to the sulfur gold chemistry, used so far for chemisorption. Copper is a material which is already integrated into standard semiconductor processes and therefore available for the integration of organic monolayers. Copper carboxylate bonds are more rigid on the surface than sulfur gold bonds, due to bonding at both oxygen atoms, therefore allowing interesting structural properties. Directed surface structures evolve especially in combination with the rectangular surface symmetry of the Cu(110) surface. This effect of modifying a monolayer by imposing a structured substrate or a surface energy modulation onto it represents a powerful technique for achieving large-scale order and anisotropic properties in the monolayer. Another reason for the use of copper is the lower computing effort associated with it, thus enabling theoretical support for the interpretation of the measurements.

2 Charge transfer on the nanoscale

Determining the charge transfer properties of individual molecules or small assemblies is of strong scientific interest, to understand and create nanoscale electronic devices. While the charge transfer mechanisms of bulk materials can be well described, the properties of nanoscale assemblies are still under investigation [34–36]. Recently, the potential of molecular electronics and the achieved structural sizes in semiconductor technology have led to an increase in research activity, important for a large field of possible applications ranging from solar cells and sensors to information processing devices. As the number of possible applications, the number of systems studied and the methods used, are manifold and range from electrochemical experiments in solution to femtosecond and terahertz spectroscopy in the gas phase. The selection presented here is focused on studies of molecular junctions.

2.1 Types of junctions

The charge transfer through a molecular junction strongly depends on its type and especially on the contact properties [37]. The junction techniques used, can be divided in two types. One way to access the electrical properties of a small number of molecules is the formation of ordered monolayers on electrodes and creating an optimized, small point of contact. The other alternative is the use of sharp, pointed electrodes and contact individual molecules directly.

Monolayer junctions are formed by mercury drop electrodes [30], crossed wire junctions [38], in wire junctions [39] or nanopores [40]. These setups are generally stable and can be cooled down for measurements without problems, except for the rather simple mercury drop electrodes. The biggest drawback of monolayer junctions is the fact, that a real single molecule measurement is not possible and always a small number of

molecules is measured in parallel. True single molecule measurements can only be performed, if pointed electrodes in the size of the molecule to be contacted, are used. These could be the tip of an AFM [41] or STM [42], directly above a monolayer or with an additional, chemisorbed nanocluster as topelectrode [43]. Alternatively, two pointed electrodes may be used to study single molecule conductance, as in the employment of mechanical break junctions [9] or nanogaps with gate electrodes [44]. These types of junctions can be used in liquid, vacuum or cryogenic environments. The scanning probe microscope based setups have the advantage of flexibility and imaging capabilities, while the fixed junctions have a small stability advantage, the possibility to measure molecules, which are chemisorbed to both electrodes and the possibility of a gate implementation.

2.2 Charge transfer in general

For the charge transfer through a molecular junction which is not metallic or semiconducting, a few basic mechanisms or a superposition of them are possible (table 2.1). The most frequently observed mechanism, especially for smaller molecules, is tunneling transport, as for alkanethiols and oligo-phenylthiols on gold (for the different tunneling regimes and their current-voltage characteristics see table 2.2). Alternatively hopping conduction, as proposed for DNA-molecules in solution [34] or thermionic emission, probably increased by field effects are possible conduction mechanisms. To elucidate the dominant charge transfer mechanism through a given molecular junction, the current dependence on voltage or temperature can be measured and compared with the characteristics of the transport types, as given in table 2.1.
When measuring the properties of nanoscale devices, the behavior of the whole system is of great importance and the extreme dimensions have to be considered. Already for the application of moderate voltages to nanoscale junctions, immense electrical fields are generated in the gap, resulting in high forces on the electrodes and molecules. Depending on the environment, the electrical field might cause a chemical change of the junction, as turned out to be the reason for a NDR-effect, observed in ferrocenes (See chapter 7). The contact of the molecule to the electrodes may be modified [45], the electrodes themselves may be altered, due to electromigration, or the molecule itself can be geometrically varied.

Conduction mechanism	Characteristic behavior	Temperature dependence	Voltage dependence
Direct tunneling	$J \sim V \exp\left(-\frac{2d}{\hbar}\sqrt{2m\Phi}\right)$	none	$J \sim V$
Fowler-Nordheim	$J \sim V^2 \exp\left(-\frac{4d\sqrt{2m}\Phi^{\frac{3}{2}}}{3e\hbar V}\right)$	none	$ln\left(\frac{J}{V^2}\right) \sim \frac{1}{V}$
Thermionic emission	$J \sim T^2 \exp\left(-\frac{\Phi - e\sqrt{eV/4\pi\epsilon d}}{kT}\right)$	$ln\left(\frac{J}{T^2}\right) \sim \frac{1}{T}$	$ln(J) \sim V^{\frac{1}{2}}$
Hopping conduction	$J \sim V \exp\left(-\frac{\Phi}{kT}\right)$	$ln\left(\frac{J}{V}\right) \sim \frac{1}{T}$	$J \sim V$

Table 2.1: Possible conduction mechanisms for a molecular junction [40]. (J, current density; V, bias voltage; T, temperature; d, distance; Φ, apparent barrier height; m, electron mass; e, electron charge; k, Boltzmann constant)

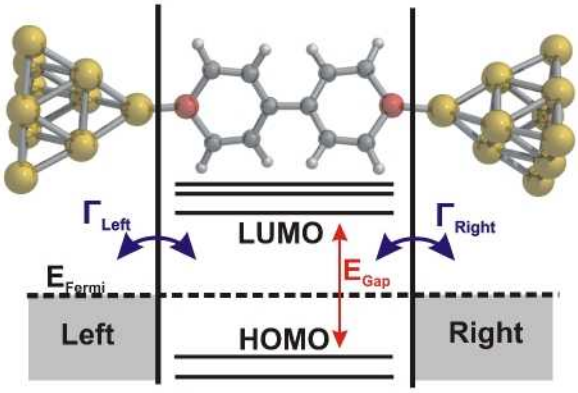

Figure 2.1: Schematic of tunneling through a molecular device. Two electrodes are separated by a molecular barrier. Both electrodes are connected and in thermal equilibrium, sharing the same fermi energy (E_{Fermi}). When a bias voltage is applied, the energy levels of the electrodes are shifted against each other, and all states in the energy range contribute to the tunneling current. The HOMO and LUMO states of the molecule in the barrier are far away from the fermi energy and do not contribute to a low bias tunneling current. The coupling Γ of the molecule determines the injection rates on both sides and influences the current.

Similarly, the current, driven through a nanoscale junction causes in a high power density in the junction, resulting in a local increase in temperature [46], which has to be considered during the characterization. The material of the electrodes plays an important aspect as well, since an electrical switching observed in a molecular junction might be attributed to oxide layers on the electrode or metal diffusion as well [14].

2.3 Tunneling through a molecular device

For most molecular junctions, elastic tunneling is the dominant charge transfer mechanism. In a simple approximation, the molecule represents a barrier between two similar metal electrodes (See figure 2.1). In thermal equilibrium, the energy states of the system are filled up to the fermi

	Low voltages $V \ll \phi/e$	**Intermediate voltages** $V < \phi/e$	**High voltages** $V > \phi/e$
Models			
Current	$J = GV \exp\left[-\beta(\phi)z\right]$ $G = \frac{e^2}{h^2}\frac{\sqrt{2\phi m}}{z}$	$J = J_0 \exp\left[-\beta(\phi)z\right](V + \delta V^3)$ $J_0 = \frac{3}{2}\frac{e^2\sqrt{2m\phi}}{h^2 z}$ $\delta = \frac{A^2e^2}{96\phi} - \frac{Ae^2}{32\phi^{3/2}}$ $A = \frac{4\pi\gamma z\sqrt{2m}}{h}$	$J = J_0 \exp\left[-\frac{4\beta(\phi)\phi z}{3eV}\right]$ $J_0 = \frac{e^3V^2}{8\pi h\phi z^2}$
Voltage dependence	$J \propto V$	$J \propto (V + \delta V^3)$	$\ln\left(\frac{J}{V^2}\right) \propto \frac{1}{V}$
Distance dependence	$J \propto \frac{1}{z} \exp\left[-\beta(\phi)z\right]$	$J \propto \frac{1}{z} \exp\left[-\beta(\phi)z\right]$	$J \propto \frac{1}{z^2} \exp\left[-\beta(V,\phi)z\right]$

Table 2.2: Approximations for the tunneling current through a planar junction and similar electrodes for different voltage regimes (J.G. Simmons [47]). For dissimilar electrodes see [48]. (J, current density; V, bias voltage; z, distance; Φ, apparent barrier height; m, electron mass; e, electron charge; k, Boltzmann constant; h, Planck's constant; γ, correction factor ~1; β tunneling-decay constant)

energy (E_{Fermi}) as marked in grey. Both electrodes are assumed to have a continuous and infinite density of states, so the electronic structure of the electrodes does not contribute to the current. When a bias voltage is applied to the junction, the energy levels of the electrodes are moved against each other by the amount $e \cdot V$ and a tunneling current of electrons from occupied states of the negative electrode to unoccupied states of the positive electrode starts to flow. Thus as a first approximation, the tunneling current is depending on the barrier height, on the barrier thickness and on the applied voltage. If the barrier between the electrodes is not vacuum, but a molecule, free and occupied states of the molecule are introduced into the junction. Most organic molecules studied are band insulators, i.e. show a relatively large energy gap between highest occupied molecular orbital (HOMO) and lowest unoccupied molecular orbital (LUMO). The existence of the molecular states in the barrier changes the effective barrier height from vacuum level to the energy levels of the molecule. To consider HOMO and LUMO states in the barrier, the more complex Franz two-band model can be used, but as shown for alkanethiols [40] the consideration of the contributions of the energy level closer to the Fermi energy are usually sufficient. For bias voltages below the conduction onset through a molecular orbital, the tunneling current can be described by the approximations of J.G. Simmons [47] for a planar tunneling barrier, as given in table 2.2.

2.4 Conduction through a molecular device

If one of the energy levels of the molecule enters the applied energy interval, the current increases and the charge transfer changes from tunneling to resonant tunneling. For the strong coupling limit, i.e. the molecule is strongly bound to the electrodes, the transmission $T(\epsilon)$ of the channel determines the conductance G which is given by the Landauer equation [34]:

$$G = \frac{2e^2}{h} T(\epsilon) \tag{2.1}$$

with the elementary charge e and Planck's constant h. For an unobstructed channel without scattering, the conductance is given by [49]:

$$G = \frac{2e^2}{h} \equiv G_0 \tag{2.2}$$

with G_0 being defined as the quantum of conductance.
If the molecule is only loosely attached to the electrodes and can be treated as an independent system, the current is determined by the transfer rates Γ between molecule and electrodes, with the charge residing on the molecule for a short time. In the weak coupling limit, the current across a single molecular level is given by [50]:

$$I = \frac{2\pi e}{h} \left[f(\epsilon_M - \mu_R) - f(\epsilon_M - \mu_L) \right] \frac{\Gamma_M^L \Gamma_M^R}{\Gamma_M^L + \Gamma_M^R} \tag{2.3}$$

with the electrode potentials μ_L, μ_R, the conducting molecular energy level ϵ_M and the fermi function f.
A typical example for a weakly coupled contact is an STM tip, which is located at a distance above a molecular layer. A typical strongly coupled contact is e.g. a strong chemical bond between a molecule and electrode, which connects the electronic states of the electrode and the molecule and thereby ensures an unhindered charge-transport. Most scanning probe studies of chemisorbed monolayers form asymmetrically coupled systems. Thus, for real experimental junctions, the circumstances are more complicated, but the simplified equations are adequate for a basic understanding. For a more detailed analysis, a complete treatment of the junction, including a part of the electrodes, with theoretical methods like density functional theory (DFT) is needed.

3 Scanning Probe Microscopy

Scanning probe microscopy (SPM) is one of the most recently developed, widespread surface analysis methods with numerous variations for different applications. Since the invention of the scanning tunneling microscope (STM) in 1981 by G. Binning and H. Rohrer [51, 52] and the invention of the atomic force microscope (AFM) by G. Binnig, C. Quate and C. Gerber in 1986 [53] the SPM technology turned from an exotic experiment to a mature surface imaging technology. SPM measurements always represent local interactions between probe and sample allowing to access certain properties with unrivalled precision. SPM measurements can show localized information about topography, conductivity, band structure, magnetism and optical properties of the sample with a fascinating resolution up to single atoms. Nowadays, different, specialized SPMs are used for surface analysis in semiconductor technology, physics, chemistry, biotechnology and medicine. [54–56].

In all SPMs, a probe is scanned over the sample surface at a low distance and the interactions between probe and sample are recorded, to obtain am image of the properties on the surface. One primary interaction, such as force with the AFM or tunneling resistance with the STM is used to control the distance between probe and sample and record a primary map, usually proportional to the sample topography (figure 3.1).

Depending on the method used, the resulting signal maps need to be interpreted carefully, because several sample properties and influences of the measurement setup are entangled with each other. Furthermore the local measurement usually delivers only small signals which are, in combination with the high precision positioning of the probe head, very susceptible to disturbing influences from outside. In addition, the principle of moving the scanner over the surface is prone to mechanical instabilities, causing a distortion of the image. I.e. a constant drift between probe and sample during the measurement causes a axial compression or elongation plus an angular abberation.

The resolution of a SPM is determined by the sensitivity of the probe head, by the exact positioning of the probe head above the sample and

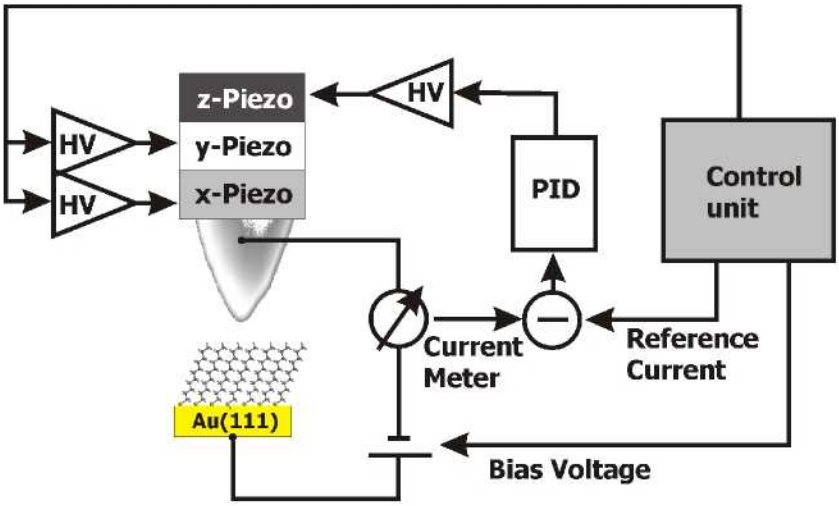

Figure 3.1: Principle of a scanning tunneling microscope. A bias voltage is applied to the tunnel junction, creating a small current, converted into an electrical signal. For other SPMs like the AFM, this signal can be created from different probe-sample interactions like a force on a cantilever. The measured signal is compared with the setpoint, filtered and feed back to the z-positioning piezo of the probe. A control unit provides ramp signals to the x and y positioning piezoelements of the scanner, to scan the surface. The primary signal or the error signal are recorded during the scan, resulting in a surface map of the probed properties.

by the electronic signal processing. The probe must be positioned and moved within fractions of a nanometer above the sample surface. This precision is achieved by the use of piezoelectric actuators, which can be designed as single-tube, sheared-stack or tripod-scanner. In addition, a coarse positioning mechanism is necessary to move probe and sample on a larger scale. Coarse positioning can be realized by worm drives, stepping motors, piezo motors or other methods. The whole assembly needs to be protected from vibrations which is crucial for high-resolution. Vibration isolation ranges from a rubber chord suspension to the ceiling and a cover, to shield acoustic oscillations from air, for a simple AFM up to air-damped systems in a silenced room with separate foundation and an eddy-current damped spring suspension system as last suspension stage.
Next to pure surface analysis a modification of the surface is possible, depending on the probe used. With STM surface adatoms [57] and small molecules [58] can be moved around and smallest structures can be build. With AFM a movement from small molecules up to larger assemblies like small polystyrene balls and surface modification by scratching becomes possible. Surface structuring on a larger scales can be achieved by local modification of a suitable interlayer, e.g. the oxidation of a titanium layer under the tip of an STM. With conductive AFM electrical structure changes can be imposed on suitable materials, e.g. ferroelectric thin films and with magnetic force microscopy, magnetic structures can be written.

3.1 Scanning tunneling microscopy

The scanning tunneling microscope is the ancestor of all modern scanning probe microscopes. Despite its considerable age and many advances and enhancements in the field of scanning probe microscopy, the STM still is the microscope which offers the highest resolution, down to molecular orbitals in real space, and rich information about the electronic structure of the sample [59].
The basic physical principle of the STM is the tunneling effect. As shown in figure 3.2. A tunneling current flows between two electrically biased metals or semiconductors, that are separated by a thin insulating barrier. In equilibrium, the energy-bands on both sides of the junction are filled up to the Fermi energy E_F. Upon applying a bias voltage to the junction, the bands are moved in energy, and an energy range $\delta E = eV_{Bias}$ is

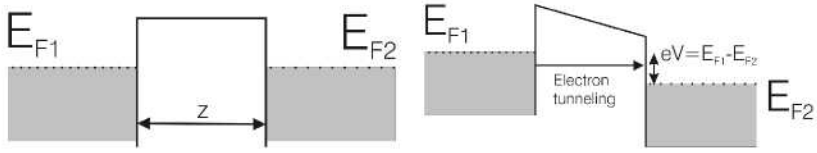

(a) equilibrium (b) bias voltage V

Figure 3.2: The tunneling effect: Two conductors are separated by a thin insulating barrier. The energy bands are filled up to the Fermi energy E_F. When a bias is applied, the equilibrium Fermi energies are shifted against each other and in the range of the energy difference, electrons can tunnel from occupied states on the negative side of the junction into unoccupied states on the positively charged side.

generated, in which electrons can tunnel from occupied states on the negatively charged side into unoccupied states on the positively charged side of the junction. The amplitude of the current depends on the applied bias, the local density of states in the tunneling energy range and the overlap integral of the wave-functions of both involved states.
The solutions of the Schroedinger-equation for valence electrons inside the insulating barrier are given by:

$$\Psi(z) = \Psi(0)e^{-k_{eff}z} \tag{3.1}$$

with the effective decay length:

$$k_{eff} = \frac{\sqrt{2m(V-E)}}{\hbar} \tag{3.2}$$

with m denoting the electron mass, $\hbar$ Planck's constant, E electron energy and V the barrier potential. The transmission probability of an electron through the barrier determines the tunneling current and declines exponentially with the barrier width z.

$$I \sim e^{-2k_{eff}z} \tag{3.3}$$

For STM imaging, the tunneling current through a small gap between a sharp tip and the sample is measured under constant bias voltage

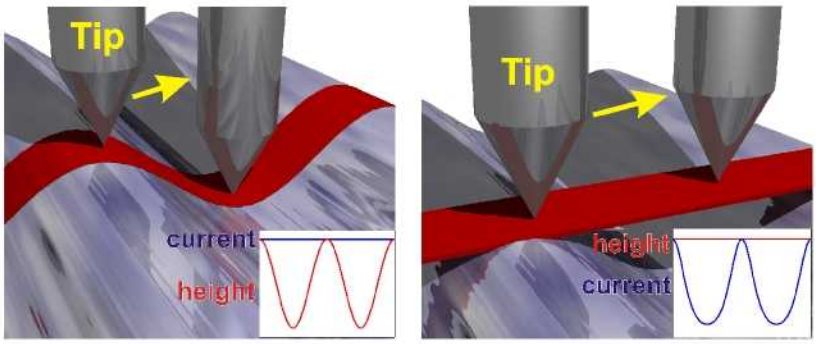

(a) elastic (b) inelastic

Figure 3.3: a) constant-current mode, the tip follows the surface corrugation and the tip height signal is used as topography image. b) constant-height mode, the tip height is kept constant and the current fluctuations due to changing tip sample distance are recorded. Note the current signal distortion due to the exponential dependence on the tip sample distance.

and is used as image and feedback information. For small biases[1], the tunneling-current can be approximated using the assumptions of Tersoff and Hamann [60]. The electrons tunnel from occupied metal surface-states of the tip into unoccupied states of the sample near the Fermi energy (E_F). The tip can be approximated as spherical s-orbital with the radius $\mathbf{r}_0$. Thus the current is proportional to the local density of states (LDOS) of tip ρ_{tip} and sample ρ_{sample} at the point of contact between orbital sphere and sample surface.

$$I \sim V \cdot \rho_{sample}(W_F) \cdot \rho_{tip}(\mathbf{r}_0, W_F) \cdot e^{-2k_{eff}z} \tag{3.4}$$

The exponential distance dependence of the tunneling current restricts the conduction path to the outermost micro-tip of the STM needle, consisting of a single atom in the ideal case. Thereby the current flow is laterally confined to a very small area and a very high-resolution can be achieved [4], [54].
The STM can be used for measuring in constant-height or constant-

[1]The applied bias voltage has to be a lot smaller than the work function

current mode (figure 3.3) [52,54,55]. In constant-current mode the junction bias and current are predefined and the tip sample separation is controlled during the scan to keep the current constant. The control signal for the tip height position is recorded as topography signal. For flat samples, the tip can be scanned over the surface in a constant-height, whereas the current fluctuates due to the changing tip sample distance. The current is recorded and produces a constant-height current image. STM images do not show purely topographical properties of the sample surface, but a mixture of local electronic properties and topography. Therefore STM measurements always need a careful interpretation and comparison to theory or previous experiments. Contrast and topography of an STM image depend a lot on the applied bias. Since the energy states around the applied bias contribute at most to the tunneling current, the structures shown, vary with applied bias. Depending on the materials used, some surface features may emerge or vanish upon variation of the bias voltage, depending on the position of the energy-states associated with them. Once the energy of a surface state is outside the tunneling energy interval, it simply disappears in the image. In addition, STM pictures are prone to typical corruptions of scanning probe microscopes, due to drift or tip imperfections like a multi-tip, which can result in misleading scans. Scanning tunneling microscopy is limited to conducting or semiconducting tips and samples with only small highly resistive structures or very thin insulating layers. If the overall resistance of the sample structure gets too high, the tunneling current is too small to be detected.

3.2 Scanning tunneling spectroscopy

The strong dependence of an STM image on the bias voltage offers the possibly for spectroscopy studies of electronic sample properties. Scanning tunneling spectroscopy (STS) measurements record the electronic structure of the sample, are performed locally and can be repeated on different surface sites. Different types of spectroscopic measurements are possible, for current-distance (I/S) measurements the bias is kept constant, whereas the tip sample distance is varied and the current is recorded. For current-voltage (I/V) measurements, the separation is kept constant and the bias voltage is modulated. By current-distance spectroscopy, the current decay parameter β of a surface can be determined. The surface state wave-functions of the sample material decay

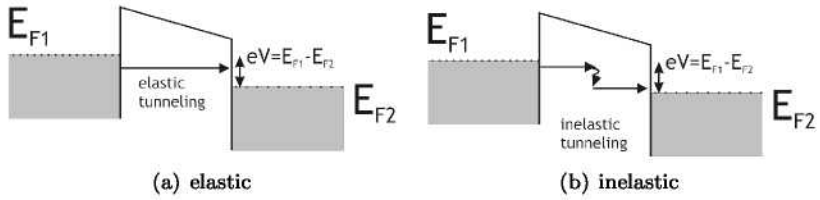

(a) elastic (b) inelastic

Figure 3.4: Elastic vs. inelastic tunneling. In the elastic case, the electron passes the barrier without interaction, for the inelastic case, the tunneling electron loses energy in the barrier, e.g. to a vibrational state.

into the vacuum with an exponential dependence on the distance. The proportional conductance $G = G_0 e^{-\beta z}$ depends on the constant quantum conductance G_0, the distance z and the material specific decay constant β. For a layered system that can be penetrated with the tip without damage and tunneling as the dominant charge transfer mechanism, the transconductance of a tunneling junction plus an insulating layer can be approximated by the product of both conductances $G_{Total} = G_{Gap} * G_{Film}$. Each conductance depends on the tunneling distance z and on the tunneling decay parameter β: $G = Be^{-\beta z}$. In case of molecular monolayers the tip can penetrate the layer and it is possible to measure the charge transfer properties of the molecules [36,61]. The current-decay parameter β depends on the apparent tunneling barrier height of the molecule, determining the tunneling current. Current-voltage spectroscopy measurements record the current while the voltage is modulated. Since the tunneling current is proportional to the LDOS of tip and sample at the contact point, the LDOS can be recovered from the measurements [62,63]. In first approximation, the LDOS is proportional to the normalized first derivative of the current versus voltage characteristic. For current voltage spectroscopy the LDOS of the tip becomes important, so tip material and shape play a greater role in spectroscopy measurement, than they do for straightforward imaging.

A special mode of operation for current-voltage spectroscopy is the current imaging tunneling spectroscopy (CITS) mode. During a CITS scan a topography image is acquired and at every single imaging point an I/V curve is measured. By using this measurement mode, spatially varying electrical properties can be assigned to local topographical features

with high precision. Unfortunately this measurement mode decreases the resolution of the image and of the spectra taken, since the tunneling setpoint cannot be optimized for spectroscopy and the frequent voltage modulations are likely to cause disturbances.
With low temperature high-resolution measurements, inelastic tunneling spectroscopy (IETS) can be performed. When tunneling elastically, the electron moves though the barrier without loosing energy. For inelastic tunneling, the electron looses energy in the barrier to excite a vibronic state of the material in the tunneling gap, leaving a unique footprint that can be compared to simulations, or other spectroscopic measurements like raman spectroscopy. For inelastic tunneling an extremely stable, helium cooled STM is necessary to provide the necessary resolution during long term measurements.

4 Construction of a new UHV-STM System

The scanning tunneling microscope is a specialized surface analysis tool with unrivalled precision and resolution. Its extreme sensitivity down to the atomic scale leads to an increased susceptibility to errors. Atomic imperfections, impurities or contaminations can be studied or if they are not objects of interest, lead to unwanted local effects which may even obstruct a whole measurement. Under normal atmospheric environment adsorbate layers are formed instantly on any surface and alter its properties. Especially the local density of states or the surface reconstructions are altered by adsorbates or even chemical reactions can take place on the surface, changing the material in a even more profound way. In addition a thin layer of water molecules, which is always present on any surface constricts the imaging resolution. In case of especially sensitive surfaces like copper, which is oxidized easily, the amount of oxygen present has to be reduced as much as possible to ensure a clean and unchanged surface during the course of a measurement. Upon cooling of the sample, the adsorbate issue becomes even more serious, since residual contaminants condensate on the sample. For high-resolution measurements of sensible surfaces at lower temperatures an ultrahigh vacuum (UHV) environment is needed. For our measurements an UHV-recipient with a base pressure of 10^{-10} mbar is used, ensuring a reasonable storage time for organosulfur monolayers on gold and a process window for the evaporation of carboxylate monolayers on sputter cleaned copper surfaces. Pressures in this range can only be achieved by use of special pumps and materials, suitable for UHV construction. Furthermore the design of moving parts in vacuum is difficult, since no lubricants may be used and all parts need to withstand elevated temperatures during bakeout. The interior of a vacuum system remains unreachable for the operator during the course of an experiment, so everything needed has to be provided by means of more or less complicated feed-throughs for motion, gases and electrical signals.

4.1 Motivation and concept

For preparation of high-quality organic monolayers, vapor deposition in a vacuum environment has proved superior to deposition from solution. By vapor-deposition, large uniform domains with sizes up to the substrate terrace size can be achieved, whereas solution deposited monolayers form much smaller domains with a higher defect density. In addition, the substances can be further cleaned by freezing-thawing cycles preceding a vapor deposition process, further reducing the defect density. Furthermore, it is possible to achieve very low surface coverages by using vapor deposition, simply by controlling the amount of material deposited, whereas for solution deposition the first adsorption step is very fast and e.g. full-coverage alkanethiol phases form within a few seconds. In case of vapor-deposition of carboxylates on copper, the deposition chamber has to be connected to the measurement chamber, to provide complete in-vacuum processing of the sensible copper surface. Thus an evaporation chamber had to be integrated into our existing STM setup, which proved difficult. To enable the use of copper single crystals as substrates for carboxylate monolayers, facilities for sputter cleaning and annealing of the sample had to be integrated as well. For the first measurements of solution deposited monolayers a commercial recipient was used, which has been shared between AFM and STM experiments and which had to be refitted every time upon change of the setup. Existing migration plans to improve the situation plus the demand for a deposition chamber and the use of single crystal substrates, requiring sputtering facilities led to the construction of a new experimental UHV-system. The technical design of the chambers and the large storage carrousel body was done by the IFF construction team and the required parts were fabricated in the IFF workshop, under scientific supervision of Prof. K. Szot. The requirements for the new system include the ability for complete vacuum processing of the copper single crystal substrates, featuring a sputtering source and vapor deposition plus sample and tip storage capacity and a heating stage for tip cleaning. The system had to incorporate an existing JEOL UHV-STM measurement head and thus use the given sample and tip transfer mechanism, as well as to use two existing main chambers with pumps and an available damping system.

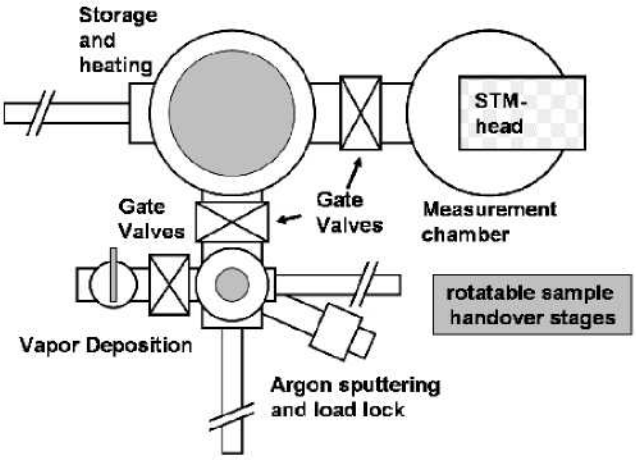

Figure 4.1: Schematic overview of the UHV System, showing the layout of all four chambers and the rotatable turnover points (grey).

4.2 Setup

The system is designed as a four chamber setup (See figure 4.1). The two main chambers, one for measurement and one for storage, are equipped with ion getter pumps. The load lock chamber, which houses the sputter cleaning system is attached to the storage chamber and is evacuated by a turbomolecular pump (TMP). A smaller vapor deposition chamber is attached on its side and pumped with a separate TMP. The vapor deposition chamber is isolated from the rest of the system to keep contamination as low as possible and to allow a separated bakeout for cleaning, without affecting other samples in the main chambers.

4.2.1 Sputter cleaning and load lock

The load lock chamber (figure 4.2) is equipped with a turbomolecular pump, reaching a base pressure of $< 5 \times 10^{-9}$mbar after bakeout. It features a front loading system for tips and samples and enables rapid insertion into the UHV storage chamber without affecting the samples by a bakeout. Additionally the chamber is equipped with an argon

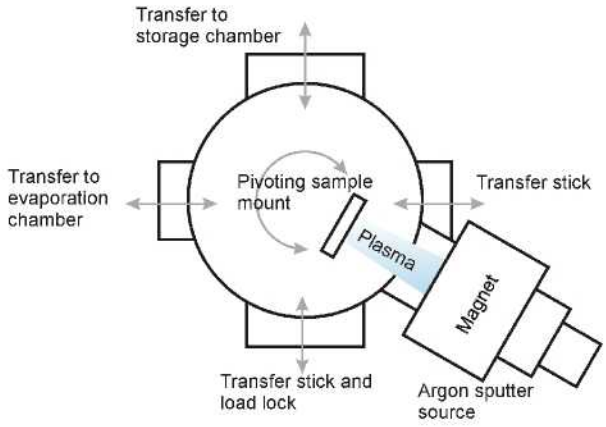

Figure 4.2: The loading and sputtering chamber is equipped with two transfer sticks and a rotating stage for sample handover and positioning. On the side an argon ion source is fitted for sample cleaning.

plasma source (Vacuum Generators Ag 21), which is operated from 8×10^{-7} mbar to 2×10^{-5} mbar at energies from 0.8 to 10 keV reaching a sample current up to 50 μA. For sample positioning during sputtering and as a handover position for transfer, the loading chamber is equipped with a rotating stage and two transfer sticks for transfer to the main and the deposition chamber. For pressure monitoring a full range pressure sensor is mounted.

4.2.2 Vapor deposition chamber

The vapor deposition chamber (figure 4.3) is parted from the load-lock by a gate-valve and is equipped with a detached pumping system, reaching a base pressure of $< 1 \times 10^{-8}$ mbar. The chamber consists of two separated volumes. The upper one is housing a rotatable sample stage to adjust the sample tilt during the evaporation. The stage provides electrical connections for sample heating as a preprocess to desorb surface adsorbates or for annealing during or after the deposition. The lower compartment is separated by an electro-pneumatic gate valve and contains the molecules. The molecules are kept in a glass vial at the

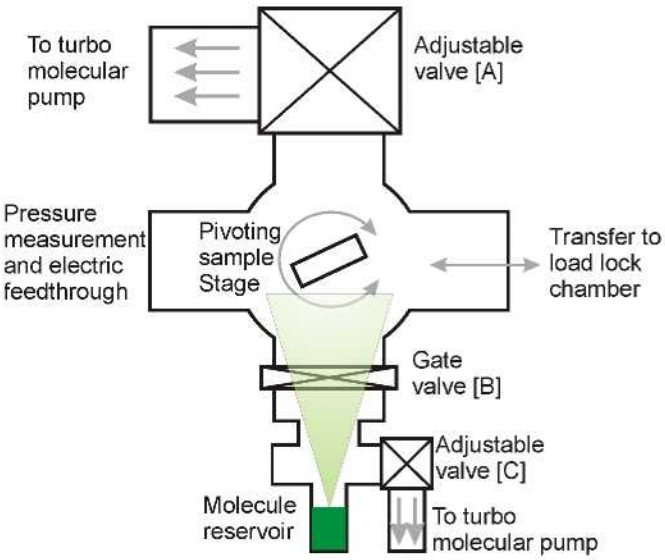

Figure 4.3: Evaporation chamber, consisting of two volumes separated by a gate valve [B]. The sample is introduced into the upper part and tilted towards the molecule reservoir. The lower part can be pumped separately to reduce contaminations. The molecules are kept in a glass vial at the bottom, which can be cooled or heated from the outside. With the adjustable valves [A,C], the volumes can be pumped separately and the deposition rate can be adjusted.

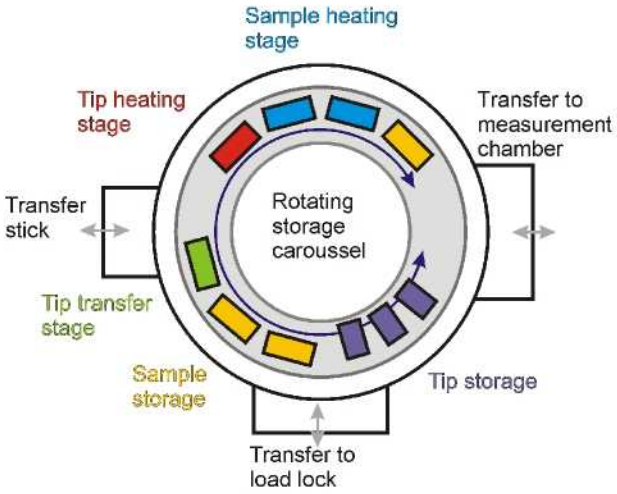

Figure 4.4: Storage chamber with a large carrousel for sample handover. On all rectangular stages, samples can be kept. On two stages, samples can be heated and on one, tips can be heated by a tungsten filament.

bottom, enabling access for cooling or heating from the outside. The lower volume can be independently pumped by a bypass from the TMP, to allow cleaning of the molecules by freezing/thawing cycles under vacuum or a lowering of the deposition pressure by differential pumping. For pressure monitoring a full range pressure sensor is mounted as well. For most substances the vapor pressure of the molecules is high enough to ensure full monolayer deposition in reasonable process time. When necessary, the vapor pressure can be increased or decreased by heating the glass vial in an oil or water bath or cooling it in ice-water or over a bath of liquid nitrogen.

4.2.3 Storage chamber

From the load-lock, the samples are inserted into the storage chamber through another gate valve. The storage chamber houses a large carrousel with a variety of sample and tip mounts. The carrousel enables handover of the samples for transfer into the measurement chamber by

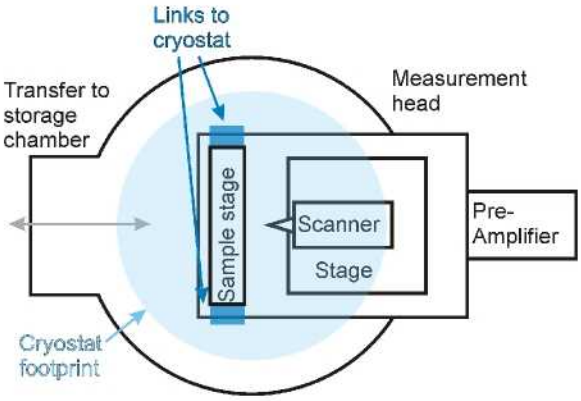

Figure 4.5: The measurement chamber houses the STM measurement head with the scanner and a sample stage plus a large cryostat on top.

another transfer stick. On the carrousel two simple storage stages and two stages providing electrical contacts for sample heating can be found. In addition three tip storage holders and two tip heating stages, equipped with a tungsten filament, are mounted together with a special mount for tip or sample handover. In the actual configuration, up to six samples and four tips can be kept on the carrousel. The storage chamber is equipped with an ion getter pump and reaches a base pressure of $< 1 \times 10^{-9}$ mbar.

4.2.4 Measurement chamber

The measurement chamber houses the commercial STM head JEOL STM-4500S and the associated cryostat. The sample carrier is inserted into the sample stage from the storage chamber through a gate valve. The sample stage is connected to a large liquid helium cryostat with liquid nitrogen shielding, which is mounted on top the measurement chamber. The measurement chamber is equipped with an ion getter pump and a titanium sublimation pump and reaches a base pressure of 5×10^{-11} mbar.

4.3 Sample and tip carriers

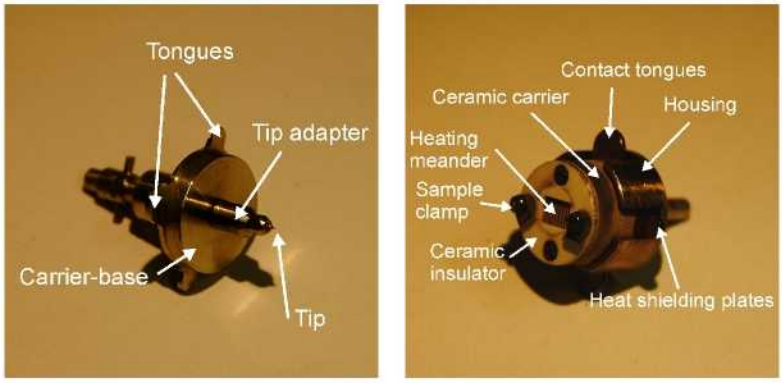

(a) Tip carrier (b) Sample heating carrier

Figure 4.6: Both carriers are designed to fit into the existing transfer and mounting mechanisms.

Transfer and mounting of tips and samples inside an UHV system represent an underestimated problem for the design of a system, due to the limited access inside the recipient and construction restrictions by the vacuum system. The transfer system, used for compatibility with the commercial JEOL measurement head, features different carriers on which the sample is mounted. The carriers can be fixed on special mounts inside the system by a nut and tongue principle and are grabbed and transferred by a claw on the transfer stick. The tip is clamped in a special adapter which is moved with the tip inside the transfer claw and that can be fastened on threaded mountings inside the UHV system.

4.3.1 Tip carrier

In the existing system, tips on their adapter are moved with the tip inside the claw of a transfer stick. To allow tip processing by sputtering and heating, a tip carrier is designed with the IFF-construction (4.6), which allows to move and mount the tip with an exposed apex, so it can be reached by the sputter beam or can be heated by a filament. To ensure compatibility with the existing principle, the system is completed with

a double sided mount on the storage carrousel, that allows in vacuum mounting of the tip on the carrier for processing and dismounting it again afterwards.

4.3.2 Heating carrier

The preparation of clean and defect free single crystal substrates requires not only a sputter-cleaning of the surface, but a thermal treatment for surface annealing as well. To heat the sample up to 1100 °C for a reasonable time a sample heating carrier was designed (figure 4.6) with the help of the IFF workshop, using a patented resistive heating design. The carrier does not exceed the standard carrier dimensions of 16 mm core diameter. The surface is heated resistively by a metal filament, mounted on a ceramic support with additional heat shielding plates. The heating carrier is suitable for heating in UHV and does not produce gases, when heated.

(a) The complete experimental system with pump control and cryostat

(b) Sputter chamber with the argon ion source with magnet, on the right

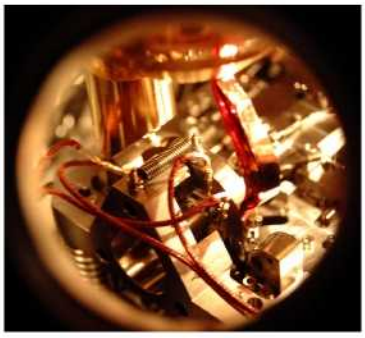

(c) Sample stage inside the measurement chamber, as seen through a viewport in vacuum

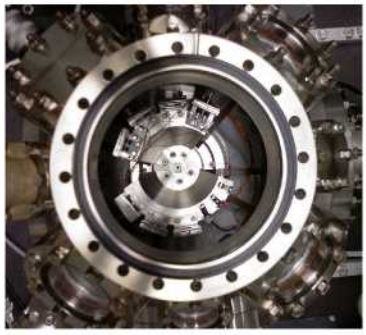

(d) Storage carrousel inside the chamber, as seen through an open port during assembly

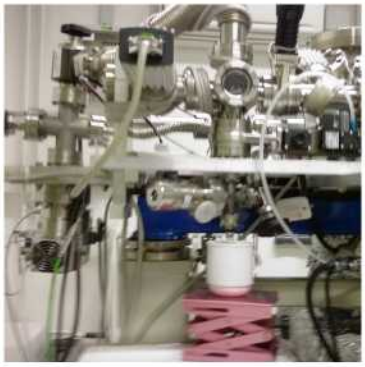

(e) Evaporation chamber, with the molecule reservoir below, cooled in a cup of iced water

(f) Heating carrier in operation, mounted on the storage carrousel in vacuum, emitting IR-radiation

Figure 4.7: Images of the complete UHV recipient, showing details of the setup from outside and inside.

5 Substrates

The inherent capability of an adequate molecule-substrate system to generate highly ordered structures on a larger scale is a fascinating power of nature. Only a fragile balance of interacting forces results in spontaneously emerging order in self-assembled monolayers (SAMs). Especially for creation of long-range ordered structures, the substrate properties become increasingly important. The surface lattice and the superstructure unit cell need to be consistent to ensure commensurate monolayer growth with a low tensile strain in the monolayer. Furthermore a reasonably low energy barrier between adjacent binding sites promotes the regularity of the thin film, by increasing the surface-mobility of chemisorbed ad-molecules during deposition. Single crystal substrates for the study of organic monolayers by STM need to be atomically flat, showing only terraces of the desired crystal orientation. Highly ordered crystalline monolayers as alkanethiols on gold are the result of delicately balanced interactions between molecules and substrate. Therefore, small substrate distortions are fully resembled by the SAM structure and decrease the local order and introduce imperfections. Thus the substrates have to be exceptionally clean and free of defects, since every defect or impurity influences the monolayer on top of the crystal. In this thesis thiols on gold and carboxylates on copper are studied.

5.1 Gold thin film substrates

An important aspect for STM studies is a continuously conducting substrate. As this is inherently fulfilled by a crystalline or polycrystalline metal substrate, the conduction of a metal thin film can vary locally. Especially gold deposited on the insulating mica substrates grows in island mode and is likely to form disconnected local crystallites, which can cause local nonconductive areas resulting in a tip crash during a STM scan. Another prerequisite for STM studies is the existence of well-defined, atomically flat terraces of sufficient size. Granular, rough layers make it necessary to increase the dynamic range of the scan and

increase perturbations to much, to achieve molecular resolution. Thus the surface has to be crystalline, showing a RMS surface roughness in the range of a few times the height of a single atomic step.

The lattice structure of a gold crystal is face centered cubic (fcc) with a lattice constant of a=0.408 nm. The (111)-oriented surface shows a hexagonal close packed (hcp) lattice with an in-plane lattice vector of a=0.286 nm and an out-of-plane lattice vector of b=0.24 nm.

For simple electrochemical studies of self-assembled monolayers of alkanethiols on gold, well cleaned and polished polycrystalline gold electrodes provide proper substrates [28,64], since these measurements are averaging over the whole electrode. For more sophisticated measurements with increased sensitivity to local structures and layer defects, crystalline gold thin films of a selected orientation are used. These can be fabricated by evaporation of gold on mica [65], gold on silicon [66,67], gold on glass [68] or by template transfer methods from glass to silicon [69]. Thin film substrates are commercially available or can be prepared with reasonable effort. They can be processed in large quantities and are mainly used if a liquid environment is used during deposition or measurement. As ultimate substrate single crystals are also used, mostly for studies under ultra high vacuum conditions [70].

For our studies gold thin films have been chosen. Thin film substrates show a high quality surface are cheap and available in large quantities. The samples can be mounted straightforward onto carriers for vacuum transfer after solution deposition. If solution deposition is used with single crystals, the samples need to be removed from the vacuum system frequently for cleaning and deposition, inducing stress to the crystal surface. For the alternative, complete processing under vacuum conditions, no facilities have been available at the beginning of this work. As substrates either mica or silicon are widely used, but for gold thin films on silicon unavoidable diffusion of silicon into the gold layer is observed and even on the surface of the gold-film, silicon impurities can be measured [71]. Therefore mica, on which epitaxial, well-oriented, high-quality thin films can be grown, is used as substrate [65]. Mica is a natural mineral with variable compositions and colors. A special type of mica named Muscovite, ($KAl_2[(OH)_2|AlSi_3O_{10}]$), with transparent, slightly brownish optical appearance is used. Mica crystals consist of thin sheets and can be cleaved easily along the (001)-plane. The freshly cleaved surface provides an ultra-clean, defect free and atomically flat surface which is dominated by oxygen atoms of the SiO tetraeders. The distance of the oxygen atoms in the crystal lattice is 0.255-0.286 nm,

which promotes (111)-oriented epitaxial growth of Au(111) with an in plane lattice constant of 0.286 nm [72].
The gold on mica substrates are manufactured by using an modified recipe developed at our institute [50,73] using the two step method originally proposed by Höpfner et al. [72]. The actual procedure involves 5 steps. The temperatures, times and the preparation steps of the procedure have been modified during the course of experiments, to optimize the results. Ultra-clean muscovite mica from Plano GmbH with a thickness of 0.2 mm is used as substrate. The sheets are cut to the desired size to fit onto the STM sample carrier, by laser cutting under nitrogen atmosphere. Laser-cutting has shown to be superior to mechanical cutting or sawing, since the mechanical integrity of the samples remains intact and the slightly burned sample edges increase the inter-layer adhesion of the mica substrates and thus their stability upon exposure to solvents or water. Immediately before insertion into the vacuum system the samples are freshly cleaved to prepare a flat and clean surface. Before gold deposition the samples are held in ultrahigh vacuum (UHV) at 8×10^{-8}mbar overnight and are heated to deposition temperature three to four hours before deposition. During this preliminary step residual gasses and moisture are desorbed from the surface (figure 5.1). Additional preheating has shown to improve the layer quality and is used, when available. The actual gold deposition is done by electron beam evaporation at a substrate temperature of about 830 K (heater temperature, the actual substrate temperature is lower, around 400 K). The thin film is deposited in two steps. First a layer of 150 nm is deposited at a high rate of 5 nm/s to achieve a continuous gold layer and a better adhesion between thin film and substrate. Immediately afterwards 50 nm are deposited with a very low evaporation rate of 0.05 nm/s. During the second step the thin film growth is much slower and remaining holes and rough features from the first step are leveled off. Finally the substrates are annealed at deposition temperature for 1-2 hours and then cooled down during two hours to room temperature. After removal from the vacuum-system, the samples are used immediately.
The substrates prepared by this procedure meet the high demands on thin film substrates for STM study. The two step deposition procedure combines the strengths of a high rate deposition and very careful low rate deposition. Under the conditions used for manufacturing gold grows in island mode [72,74], as expected for the thin film deposition of metals on insulators. The first step in island growth mode is the nucleation of small clusters on the substrate. The clusters and adatoms diffuse and

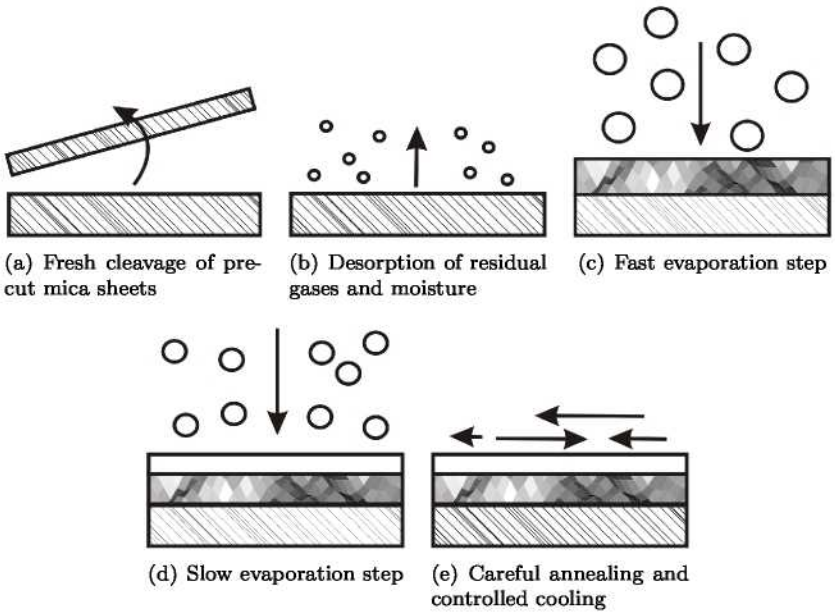

Figure 5.1: Au(111) thin film deposition procedure. Immediately before insertion into the vacuum system, the mica sheets are cleaved, to yield a clean and flat surface. Afterwards the substrates are heated in vacuum, to desorb remaining moisture and adsorbates. The actual deposition takes place in two steps with a subsequent annealing step, to optimize the surface roughness and crystallinity.

collide until they reach a critical nucleation size and grow into islands. Upon a certain thickness the islands start to coalescence into a continuous film with remaining, deep trenches until a full coverage film is formed and the growth mode changes to a 2d wetting mode. This critical thickness depends upon the material system and on the surface mobility of the adatoms and the deposition rate [50, 74]. Since the surface mobility increases with temperature, the critical film thickness increases with temperature as well and makes a lower deposition temperature desirable. On the other hand a higher deposition temperature promotes the coalescence of the growing islands and therefore leads to a lower surface roughness and less defects [75]. The deposition temperature is further limited by the decomposition of the mica substrate, which starts at around 640 K as measured by QCM [50, 73]. Thus the substrate temperature is chosen slightly below the mica decomposition point. For the first step a high deposition rate is chosen, to promote an early coalescence of the islands and thereby achieve a continuous, conductive layer. After the first step, deep trenches, holes and a few defects remain, which are leveled out during the second, slow evaporation step. During the following annealing step the surface roughness is further decreased.

The crystallinity and orientation of the substrates is verified by XRD [50, 73] and is also evident in the STM images (figure 5.2). The surface roughness is reduced to 0.2-0.3 nm rms/25 μm^2, as shown by AFM in figure 5.2a. AFM and STM measurements of the untreated surface show the characteristics of a clean, crystalline, (111)-oriented gold surface (figure 5.2). The surface is dominated by atomically flat terraces of triangular shape with monoatomic steps of 0.24 nm height, along the $(0\bar{1}1)$, $(\bar{1}10)$ and $(01\bar{1})$ directions of the surface. Upon closer inspection two kinds of terrace structures can be found. Smaller terraces with rounded edges, corresponding to the usual surface structure and long range straight steps, which are attributed to strain relaxation due to the different thermal expansion coefficients between gold and mica [50, 73]. This extended defects are minimized by extending the cool-down time and a better temperature control during the cooling phase.

On the terrace surfaces double lines forming a zigzag pattern with 120° angles can be seen (figure 5.2c). This pattern reflects the $23 \times \sqrt{3}$ surface reconstruction of the gold lattice due to the symmetry break on the surface (figure 5.2e). The reconstruction, first noticed by Perdereau et al. [76] leads to an extra surface atom per 22 regular surface atoms and thus a surface compression of 4.4% [77]. With further increased resolution single gold atoms on the surface can be distinguished.

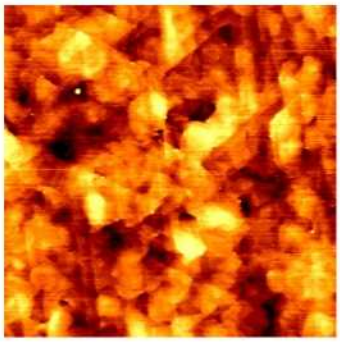

(a) 5 × 5 μm AFM scan, showing triangular substrate terraces

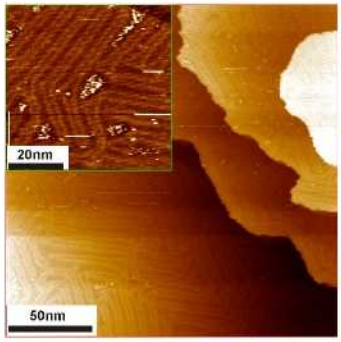

(b) UHV-STM scan of gold terraces showing the surface reconstruction

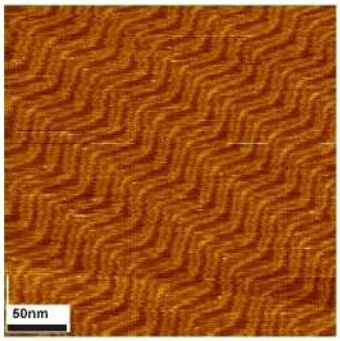

(c) UHV-STM scan, showing the surface reconstruction

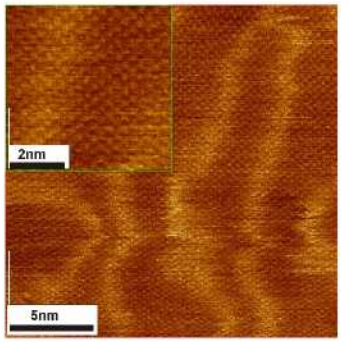

(d) UHV-STM scan with atomic resolution of the Au(111) surface

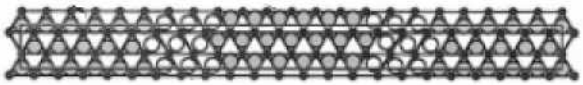

(e) Schematic drawing of the Au(111) 23 × $\sqrt{3}$ surface reconstruction by Poirier et al. [70]

Figure 5.2: AFM and STM scans showing the gold (111) surface of the used thin film substrates. The substrates show the Herringbone reconstruction and terraces with a height of ca. 0.24 nm corresponding to a single monolayer of gold atoms.

The substrates manufactured, using this two step deposition recipe are fully characterized and yield high-quality thin films for STM studies.

5.2 Copper (110) single crystal substrates

To study an alternative system to alkanethiols on gold, carboxylates are chosen, as described in chapter 8. The Cu(110) surface shows a striped surface pattern of alternating higher and lower atom rows. Together with the carboxylate group, which fits exactly on the substrate, the structures formed, are strongly influenced by the surface modulation, which represents a powerful method to achieve larger scale, ordered assemblies. Furthermore, copper is already integrated into silicon technology, at the interconnect level and therefore favorable for future applications. From the theoretical point of view, copper is also favorable to gold, since it has less electrons and requires less computational effort for DFT calculations.

Similar to the substrates for self-assembly of alkanethiols on gold, a crystalline, atomically flat, clean and adsorbate free surface with sufficiently large terraces must be provided. Unfortunately, copper is very prone to adsorbates and oxidizes instantly upon contact with atmosphere. Thus it is not possible to process copper crystals under atmospheric conditions. The single crystals must be kept inside the UHV-setup and cleaned and annealed before use, thereby a sputter cleaning and annealing process as used in literature [78] has to be established. Copper single crystals are grown and cut by the IFF crystal workshop and polished at the IBN crystal workshop at the Research Center Juelich to receive small (110)oriented crystal pieces with a shiny surface. The provided crystals are mounted onto special heating sample-carriers (See chapter cha:uhv-exp) and loaded into the UHV-system for processing. In addition to carboxylates, thiol functionalized molecules can be adsorbed on copper, as well [26, 79, 80].

The copper crystal structure is face centered cubic(fcc). The (110) surface represents a diagonal cut though the unit cell and shows a typical striped surface. The higher surface atoms form rows in $(\bar{1}10)$-direction with $a_s = a/\sqrt{2} = 0.2556\,\text{nm}$ inter-atomic distance and a distance of $b_s = a = 0.3615\,\text{nm}$ in (001)-direction between the lines, with the copper lattice constant of a=0.3615 nm as shown in figure 5.3. The step height of the surface terraces is $h = 0.1278\,\text{nm}$.

Before deposition of the organic thin films, the copper crystal needs to

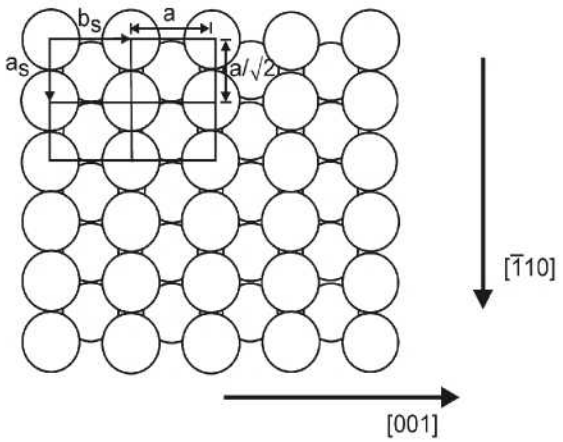

Figure 5.3: Structure of the copper (110)surface. The lattice constants of the surface unit cell are $\underline{a}_s = 0.2556\,\text{nm}$ in $(\bar{1}10)$-direction and $\underline{b}_s = 0.3615\,\text{nm}$ in (001)-direction.

be treated carefully and a procedure for repeated removal of the organic monolayer with following cleaning and annealing cycles needs to be established. Thus achieving comparable measuring conditions for repeated monolayer deposition and characterization. To prepare large contamination free terraces, the substrates are treated differently and studied with XPS and STM. The adsorption behavior of the clean copper surface in vacuum is studied by x-ray photoelectron spectroscopy (XPS). For XPS measurements the crystal is argon sputtered and annealed and the type and amount of adsorbates depending on the vacuum pressure and storage time are monitored. All XPS-measurements are performed at the Institute of Physics, University of Silesia, Katowice, Poland with a Physical Electronics XPS-spectrometer equipped with a Al-K_α x-ray source and a base pressure of 10^{-10} mbar. The sample is cleaned in situ by argon sputtering at a pressure between 10^{-5} and 10^{-6} mbar. The XPS-spectra are recorded at a photon energy of $\hbar\omega = 1487,6\,\text{eV}$ and an incident angle of 45°. The detector is perpendicular to the surface.

After polishing, precleaning and a few weeks storage under argon atmosphere, possible adsorbates can be measured (figure 5.4). The XPS spectrum shows the characteristic peaks of the copper surface

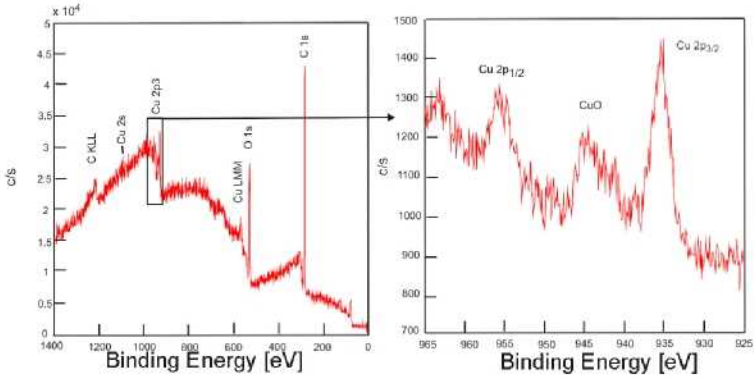

Figure 5.4: XPS-spectrum of a copper single crystal kept under argon atmosphere for a few weeks and an enhanced resolution measurement on the right. Characteristic peaks for carbon and oxygen adsorbates are visible as well as peaks for different bonding configurations of the copper atoms, indicating copper-adsorbate bonding.

(Cu 2s, Cu 2p3) and the related secondary peaks (Cu LMM and Cu KLL). In addition carbon (C1s) and oxygen (O1s) contaminations are measured. To determine the nature of the adsorbates a higher resolution scan in the energy range of the copper bonding orbitals is necessary (figure 5.4 right). In the high-resolution scan, a broad copper oxide (CuO) peak is visible besides the two copper peaks and indicates chemisorbed oxygen on the sample surface. After argon sputter cleaning of the surface at 2 keV for 10 min, the crystal is characterized with XPS again (figure 5.5). After cleaning, the carbon (C1s) and oxygen (O1s) peaks are decreased considerably and the oxide peak (CuO) in the high-resolution scan has vanished, whereas the copper 2p3 peaks are more pronounced and more secondary copper peaks (CuLMM) are visible.

To estimate the influence of the vacuum on the surface, the freshly cleaned sample is stored at different pressures and the evolution of the copper oxide peak is monitored figure 5.6. Compared to the clean surface (dark blue), all peaks of the contaminated sample (red) are shifted

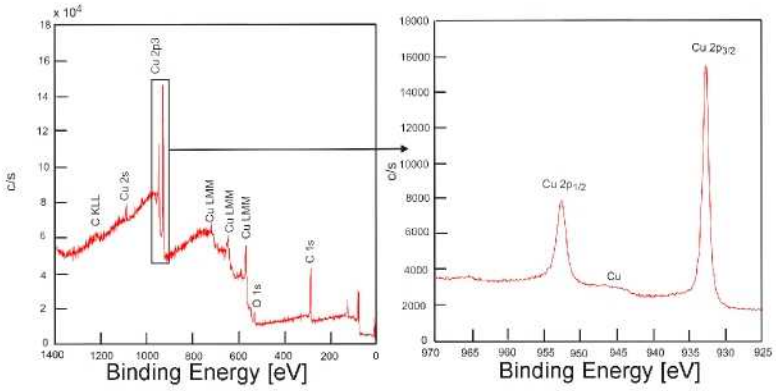

Figure 5.5: XPS-scans of a sputter cleaned copper crystal. Compared to figure 5.4 the oxygen and carbon peaks are decreased considerably, more copper secondary peaks appear (Cu LMM) and the CuO peak in the high-resolution scan has vanished.

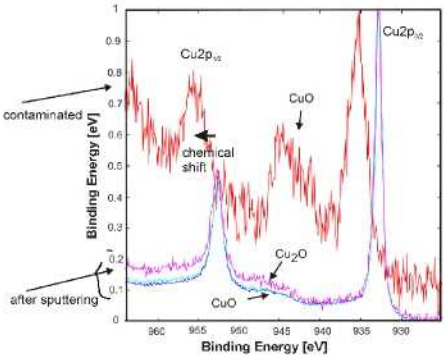

Figure 5.6: High-resolution XPS-spectra for contaminated sample (red), freshly sputtered surface (dark blue), surface exposed to 10^{-9} mbar for two hours (cyan) and exposure to 10^{-7} mbar for 30 min (pink). The chemical shift of the contaminated spectrum is visible, as well as the evolution of the copper oxide peaks upon exposure to vacuum.

to higher energies, due to a chemical shift caused by the adsorbates. After storage at 10^{-9} mbar for two hours (cyan), no effect is visible. After successive storage in another chamber with a higher base pressure at 10^{-7} mbar for 30 minutes, a small shift of the 2p_3/2 peak and a beginning evolution of the copper oxide peaks is visible. These results indicate, that great care must be taken while handling the copper substrates. Handling at 10^{-9} mbar during an experiment is considered safe in terms of oxygen adsorption, whereas for higher pressures the surface is quickly covered by oxygen, and the deposition of carboxylate monolayers is changed.
In addition to XPS-measurements, the clean copper surface is studied by STM, to optimize the sputtering/annealing cycles with respect to the surface morphology. Processing of the copper single crystal is done in the new experimental system, described in detail in chapter 4. The topography is scanned at a pressure of 1.0×10^{-10} mbar, the sample can be sputtered at a pressure range from 10^{-5} to 10^{-6} mbar and the crystal can be heated up to 1400 K in UHV. All scans are done in constant-current mode with a tunneling setpoint of -1 bis -2 V and 1 bis 2 nA consistent with literature values [81]).

Energy	Focus	Pressure	Time	Cycles
1,8 keV	4,8 keV	1.0×10^{-5} mbar	30 min	4

Table 5.1: Sputtering parameters for copper single crystal cleaning.

Current / Temperature	Pressure	Time	Cycles
0,9 A ≅ 960 K	3.0×10^{-9} mbar	25 min	4
1,1 A ≅ 1043 K	3.0×10^{-9} mbar	5 min	

Table 5.2: Heating parameter for two-step annealing of the copper crystal. Current data refers to the heating sample-carrier used.

After variation of the sputtering parameters, pressure, time and energy, a sputtering recipe for the copper surface, as listed in table 5.2 is found.

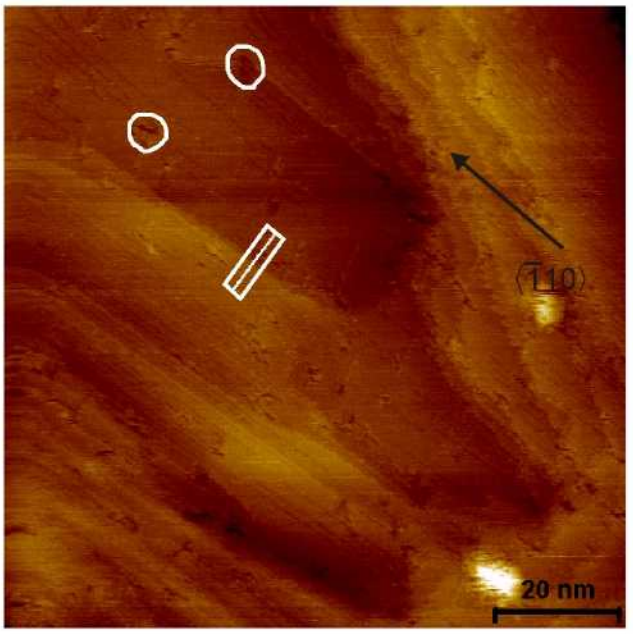

(a)

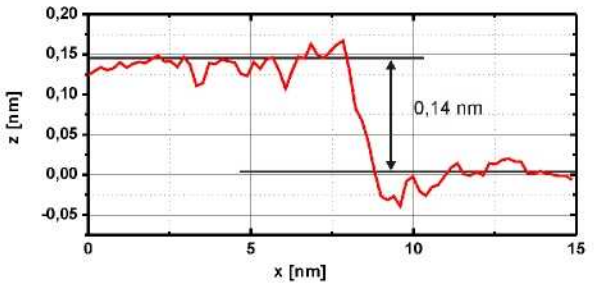

(b)

Figure 5.7: 100×100 nm^2 scan of a copper surface treated with the established cleaning procedure. Large clean terraces with little defect (marked white) concentration can be seen. The profile (marked white) shows the height of the terrace is a single atomic step of 0.14 nm.

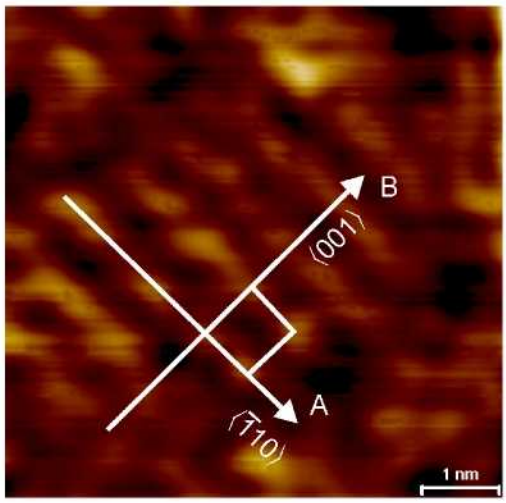

Figure 5.8: 6,4× 6,4 nm^2 STM Scan ($U_T = 0,18\,V$ and $I_T = 280\,pA$) showing an area of oxygen adsorption with a $(3 \times 2)O$ superstructure.

For the alternating annealing steps, the established procedure is described in table 5.2. The given procedure of sputtering and subsequent annealing cycles results in a clean surface with relatively large terraces of 20-30 nm. Longer or stronger sputtering results in larger terraces, but induces more defects [81], which can be difficult to heal. During annealing similar considerations have to be taken into account. Moderate heating heals defects and desorbs adsorbates, but strong heating causes diffusion of buried impurities and defects to the surface. If the temperature exceeds the thermal roughening temperature ($T_R = 1030\,K$), a complete reorganization of the surface occurs and a stepped morphology evolves [82].

After sputtering and annealing by using the established procedure of four alternating sputtering, heating cycles, the surface shows large and clean terraces with little defects and adsorbates. The terrace height corresponds to a single copper layer ($h = 0.1442\,nm$) as shown by the profile in figure 5.7.

After overnight storage a striped structure, indicating oxygen coverage can be found. The observed structure does not cover the whole surface

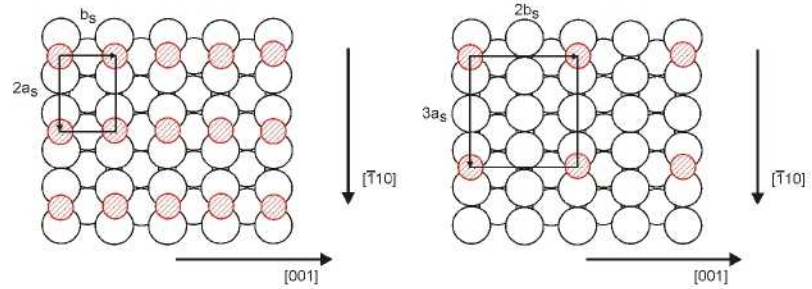

(a) (2 × 1)O reconstruction (b) (3 × 2)O reconstruction

Figure 5.9: Monolayer oxygen coverage on a Cu(110) surface. For full coverages a (2 × 1)O structure (a) is observed, for lower coverages a (3 × 2)O structure is found (b).

and is ordered only in small areas. Scans of the ordered areas show a (3 × 2)O superstructure as shown in figure 5.8. The structure indicates a beginning oxygen coverage, since for full-coverage a (2 × 1)O structure is observed as shown in figure 5.9. These observations show oxidation of the copper surface even at UHV pressure of 1×10^{-10} mbar for several hours and indicate the necessity for quick sample handling to ensure an unchanged surface during the experiment. For an intentional, full oxygen pre-covered surface, the sample needs to be exposed to more oxygen.

A procedure to provide clean and flat surfaces for the deposition of carboxylate monolayers is established for the new UHV system. The described procedure of four subsequent cycles of argon sputtering (1,8 keV, 20μA, 30 min) at a pressure of 1.0×10^{-5} mbar and heating (25 min at 960 K and 5 min at 1043 K) at a pressure of 1.0×10^{-9} mbar is used as a starting point for characterization of the carboxylates. The oxygen adsorption behavior is studied by STM and XPS and oxygen adsorption for higher pressures or longer storage is observed. For immediate characterization in UHV after cleaning, a clean surface is observed.

6 Self-Assembled Monolayers of Alkanethiols on Au(111)

6.1 Introduction

The inherent capability of an adequate molecule-substrate system to spontaneously generate highly ordered structures on a larger scale is a fascinating power of nature (See Chapter 1.2), inspiring to the whole field of science dealing with nanostructures. Starting with the work of Nuzzo, Allara, Whitesides, Chidsey and Scoles [67,83–87], self-assembled monolayers of alkanethiols on Au(111) surfaces became one of the most thoroughly studied self-assembled systems today and a model system for self-assembly in general [23]. The alkanethiol gold system is a simple and robust system which behaves well under laboratory conditions and yields long range ordered monolayers with domain sizes up to around 100 nm. Still, after years of research some details are still not completely understood, making the alkanethiol gold system a perfect system to start exploring the nanocosmos of molecular self-assembly.

Self-assembled monolayers of alkanethiols can be deposited from solution [67,90] or from gas phase [91,92] (See figure 6.1), yielding the same monolayers but a better film quality and a larger domain size for gas-phase deposition [50,93]. The thiols, supplied from solution or gas phase are chemisorbed by the formation of the strong, covalent sulfur-gold bond [88]. For low coverages, the alkanethiols move freely on the surface and form a liquid phase. Upon increasing coverage, the molecules form ordered, lying-down domains with characteristic striped structures [94–98]. Upon further deposition, islands of standing-up molecules form until saturation of the surface and thus a full-coverage monolayer is achieved [92, 99] (figure 6.1). Due to the chemically passive alkane tail-group of the chemisorbed species, the monolayer growth is self-terminating and additionally adsorbed molecules can be removed easily by rinsing or thermal desorption [24, 100]. Thus the formation of bi-layers or adsorbate layers can be excluded. The resulting monolayer

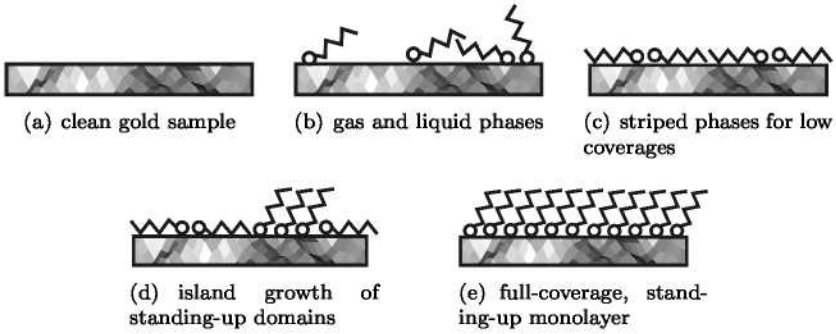

Figure 6.1: Evolution of an alkanethiol thin film, from clean substrate via intermediate phases to a full-coverage self-assembled monolayer.

can be thermally annealed in solution, vacuum or atmosphere, to reduce defects and increase domain size [101–104]. Interesting attempts were made to examine the influence of the deposition environment, e.g. the deposition from a lyotropic phase liquid crystal was described [105] and the use of stabilizing agents to inhibit the degradation of the monolayers was studied [106]. The monolayer formation is governed by intermolecular van der Waals interactions between the alkane chains and by the molecule-substrate interaction, via the formation of the sulfur-gold bond. Due to the strong intramolecular forces the alkane chain is assumed in all-trans configuration. The molecules form a two dimensional polycrystalline layer on the sample surface with three angular degrees of freedom (figure 6.2). Compared to the intermolecular spacing of bulk alkane-crystals, the chemisorbed alkanethiols on the gold surface have a considerable lattice mismatch of more than 10% [107]. This mismatch is compensated by a tilt θ of the molecular axis of 30-34° with respect to the surface normal [23, 88, 107, 108]. Thus the sulfur spacing at the interface is adjusted to meet the energy modulation of the gold surface leading to a footprint of $0.216\,\mathrm{nm}^2$ per alkanethiol or one molecule per three gold surface atoms. The molecular structure of the monolayer for different alkane chain lengths was investigated in great detail [24, 109]. The full-coverage, close packed monolayer shows characteristic topographical properties on the atomic scale, revealed by SPM methods. The SAMs show a special surface texture due to the molecular super-lattice, rotational and

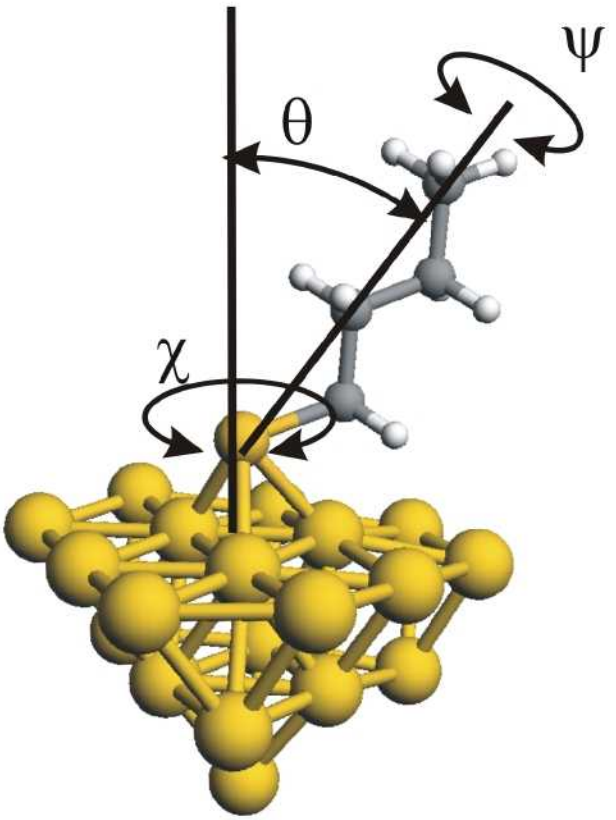

Figure 6.2: Schematic angular degrees of freedom for a chemisorbed and fully stretched alkanethiol molecule. Angle θ refers to a tilt of the molecular axis to the surface normal, χ defines tilt direction of the surface projection of the molecular backbone vs the next-nearest-neighbor direction of the Au lattice and the twist angle ψ describes the rotation of the C-C-C backbone against the plane of surface normal and tilt direction. Common values are θ= 32° χ= 55° ψ= 14° [88,89].

translational domain-structures, etch-pits emerging during the assembly process and surface features of the underlying gold substrate, like atomic terrace steps. As molecular lattice of a saturated monolayer, hexagonal packing of the molecules with an additional c(4×2) symmetry was observed by helium diffraction experiments [87,110] and GIXD [107]. Detailed real space studies are conducted by STM and came up with the internal details of the well known c(4×2) superlattice [108,111], which is formed by alternating heights of the standing-up molecules in the STM. The c(4×2) structure is the most observed and best described structure so far [24, 111–113] and thus became the standard structure assumed for close packed layers. Four slightly different c(4×2) superstructures with the same unit cell, but different height distributions, were observed frequently with STM [99, 114–116] and AFM [113, 117]. For pre-treated samples additional structures with differing unit cells were measured by STM, a $(6\times\sqrt{3})$ final phase after long term storage (6 months) [118], a (3×4) superstructure confirmed by LEED and DFT calculations [119] as well as different structures from theoretical calculations [120, 121], and intermediate standing $(p\times\sqrt{3})$-phases [115]. The nature of the different apparent heights of the molecules in the c(4×2) unit cell is still under discussion. As generally assumed, the height modulation is caused by different twist angles ϕ of each molecule around the molecular axis. However the effect of the molecular twist alone is not enough to explain the amplitude of the height differences. In a recent paper, Liu et al. [122] proposed a new mechanism for the height modulation being caused by a different local density of states inside the c(4×2) unit cell originating from changing hybridization of the sulfur bonding orbitals. In addition, they observed only two different coexisting c(4×2) superstructures each of which can be changed reversibly into the different c(4×2) structures observed by bias modulation.

The situation at the interface between alkanethiols and gold is still under discussion likewise. Although the sulfur-gold bond is very strong and upon pulling, chemisorbed molecules will pull a gold wire out of the surface [123], the molecules are still very mobile on the surface [124, 125] and gold atoms may diffuse under the monolayer [102, 126]. The different possibilities for the adsorption site under discussion are illustrated in figure 6.3. Traditionally, the sulfur end-groups are assumed to bind on the triple hollow sites of the gold lattice, in particular to the fcc-sites [22, 23, 111, 127]. Early indications for sulfur pairing on the surface [128], have been abandoned [24, 90, 120, 127], but strong indications for different bonding sites still exist. A mixed arrangement

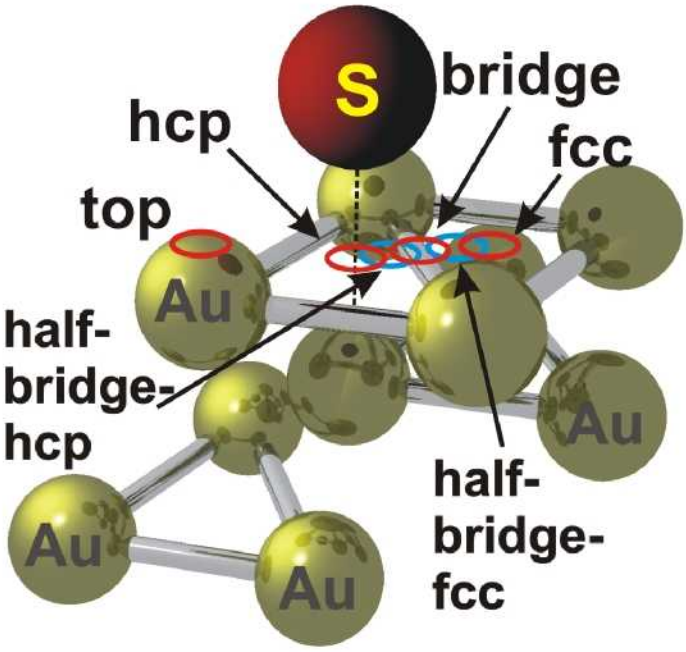

Figure 6.3: Schematic drawing of the different adsorption sites on the Au(111) surface. The picture represents the three uppermost gold crystal layers and one sulfur atom to be adsorbed on top. The sulfur can be bound at different positions: The two slightly different triple hollow sites (hcp or fcc) between three surface atoms, on top an surface atom, at bridge-site, between two surface atom or between bridge and hollow on one of the two half-bridge positions indicated in blue.

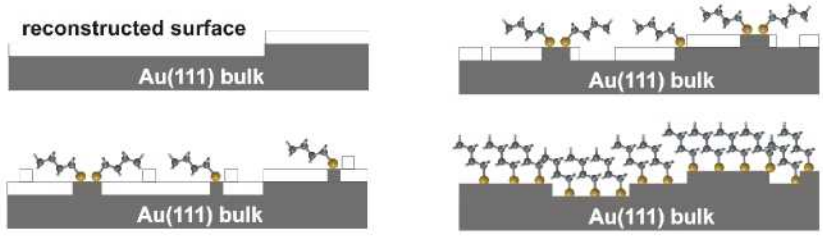

Figure 6.4: Schematic of the origin of the vacancy islands. The outermost layer of a clean Au(111) surface exhibits the herringbone surface reconstruction, marked white. Upon adsorption of alkanethiols the reconstruction is partially lifted and molecules and adatoms diffuse on the surface. With increasing coverage the reconstructed area is decreased and alkanethiols and defect atoms start to form islands, whereas the adatoms, due to higher surface mobility mostly coalesce with the terrace steps. Finally full coverage is achieved and the reconstruction is lifted completely [109].

of varied adsorption sites was suggested upon sum-frequency generation measurements [129] and x-ray standing wave (XSW) measurements [130]. Whereas the fcc bonding sites were observed by grazing incidence x-ray diffraction (GIXD) as the preferential adsorption sites for thiols [131]. Depending on the exact settings, theoretical simulations yield different results like binding to bridge positions [132], hollow site binding [133] or differently tilted molecules on fcc sites [134]. Recently, Yu et al. [135] suggested sulfur-bonding on top of an fcc gold-adatom, as they observed by XSW. In common agrement, alkanethiols are mobile on the surface with reasonably low energy-barriers between adjacent bonding sites and the gold surface imposes a strong ordering force on the monolayer leading to a commensurate superlattice with the c(4×2) unit cell.

Another characteristic feature of alkanethiol monolayers becomes visible when imaged with a local, real-space method like STM. The surface of the monolayer shows many small, dark depressions known as etch-pits or vacancy islands. These pits represent one atom deep depressions in the underlying gold surface, caused by lifting the herringbone surface reconstruction of the gold surface upon chemisorption of the thiols [70,109,136]

(See figure 6.4). Immediately after deposition the vacancy islands exist in large numbers and have small dimensions, whereas upon annealing they undergo an Ostwald-ripening process and coalesce into larger depressions or fuse with terrace steps [103, 137].

6.2 Experimental

The alkanethiol monolayers are deposited straightforward from solution, rinsed with ethanol and directly transferred into the UHV-System. A complete, saturated monolayer of dodecanethiols (Aldrich, >97 % purity, used as purchased) is formed by exposing the sample surface in 1 mmol/l solution of dodecanethiols in ethanol for more than 24h. As substrates electron-beam evaporated gold thin films, as described in chapter 5, are used. The quality of the substrate surface and thus the monolayer quality decay quickly upon exposure to atmosphere. Thus the substrates must be processed immediately after removal from the vacuum system. Unless otherwise noted, the samples are annealed in solution, after a full monolayer has formed to increase domain sizes and decrease defects. After solution processing, the samples are rinsed with ethanol and transferred into the UHV-system. If mentioned, the samples are slightly heated in vacuum again, to desorb remaining surface contaminations and further increase the quality of the thin film. Solution handling and layer processing is done under argon-atmosphere in a glove-box, when technically possible. Handling in argon slightly improved the film quality but is not mentioned explicitly. Alternatively, monolayers are deposited from gas phase as described by Lüssem et al. [50, 116]. As STM a JEOL JSPM 4600 UHV-STM with a base pressure of 3×10^{-10} mbar is used. After technical changes as described in chapter 4, the base pressure is lowered to 1×10^{-10} mbar. Imaging is done with homemade electrochemically etched tungsten tips. All scans are done in constant-current mode with a typical tunneling setpoint of 1.4-2 V and 30-50 pA.

6.3 A new c(4×2) -superlattice, the ζ-phase

As discussed in the introduction of this chapter, a saturated monolayer of alkanethiols on Au(111) forms different variations of the c(4×2) superlattice. The known structures are classified as α to ϵ phases with up

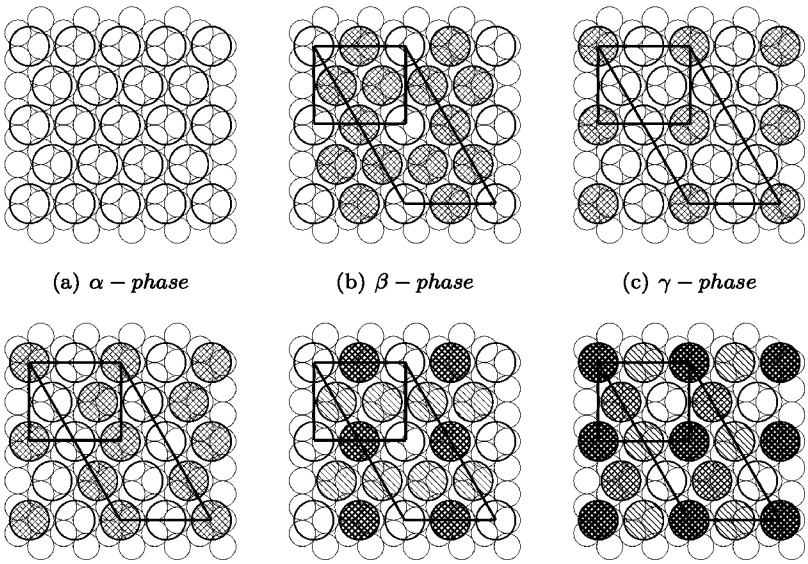

Figure 6.5: Schematics of the different surface structures of an alkanethiol SAM. Higher molecules are shaded darker. ($\sqrt{3}\times\sqrt{3}$) structure (α-phase) and different c(4×2) phases of dodecanethiol SAMs. α-ϵ-phases as described in literature [99,114,115] and the newly discovered ζ-phase (See chapter 6.3), as described in [116].

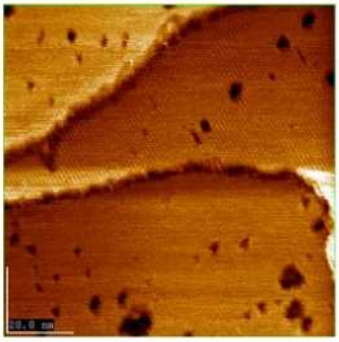

Figure 6.6: $100 \times 100\,nm^2$ STM image of a vapor deposited dodecanethiol SAM. The picture shows the gold terrace structure (large steps) and etch-pits (dark holes). On the terraces a characteristic striped texture, caused by the c(4×2) structure, is observed and a continuous texture without domain boundaries can be seen. Thus the domain-size is limited only by the terrace size.

to three different molecular heights within each unit cell [99, 114]. For vapor deposited layers of dodecanethiol a new c(4×2) structure with four different heights per unit cell is discovered [116] (See figure 6.5).

The vapor deposited films yield high-quality monolayers as shown in a large area scan in figure 6.6. Several substrate gold terraces are visible on the surface. The covering monolayer shows a stripe pattern with a periodicity of 1 nm, which indicates the c(4×2) structure. The domain-size is very large, especially compared to solution deposited SAMs. No domain boundaries can be seen, and the domains extend over the whole gold terrace. Compared to other STM images of SAMs of alkanethiols, the vacancy islands are not connected by domain boundaries and there is a large variation in size of the vacancy islands. Such large domains of alkanethiol SAMs can be grown from solution only by an additional annealing step [100]. Since Kondoh et al. [93] also showed large area domains of a hexanethiol-SAM ($C_6H_{13}SH$) grown by vapor deposition, this effect seems to be due to different growth dynamics of vapor phase growth compared to growth from solution.

In high-resolution images, the c(4×2) reconstruction is visible (See figure 6.7). Two different phases of c(4×2) are shown here: the common α-phase with two different heights in each unit cell and the new ζ-phase

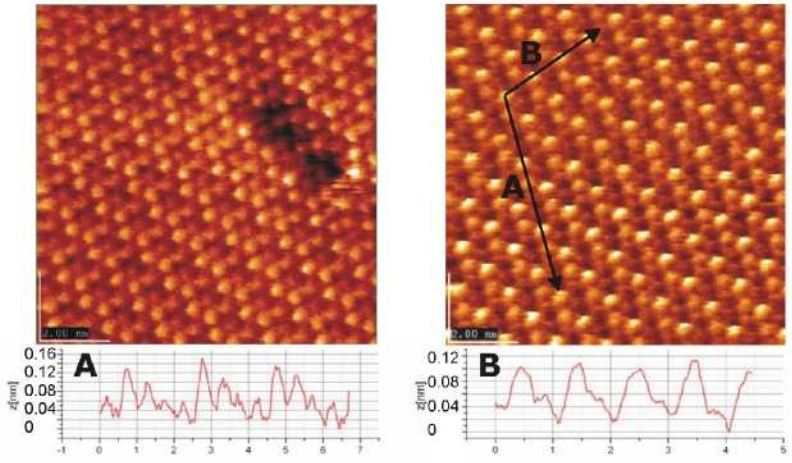

Figure 6.7: Structure of the common δ-phase c(4×2) -structure (left). The new ζ-phase c(4×2)-structure with four different molecules (right). The two linescans represent the profiles marked A and B, showing four different heights per unit cell.

with four different heights. The height differences are shown in the cross sections A and B. Along cross section A, groups of four molecules are visible, in which each molecule appears approximately 0.03 nm lower than the preceding molecule. Along cross section B, one high molecule and one low molecule alternate. The maximum height-difference observed in our structure (0.09 nm) is close to the maximum height difference that can be explained by a twist of the molecular backbone [108]. Because STM cannot distinguish between real height differences due to a twist of the molecules and differences in tunneling conditions due to different bonding states, the structure shown in figure 6.7 can be explained by both theories. For undecanethiol monolayers with an odd number of carbon atoms, causing a different angle of the methyl-group to the surface, a slightly different c(4×2)-structure, with four different apparent heights is observed. To ensure the independence of the height modulation from the scanning direction, the monolayer is scanned in different directions and resulting profiles of the molecular surface are compared (figure 6.8). The profiles show four different heights per unit cell, regardless of the scanning direction. Thus the height modulation is not caused

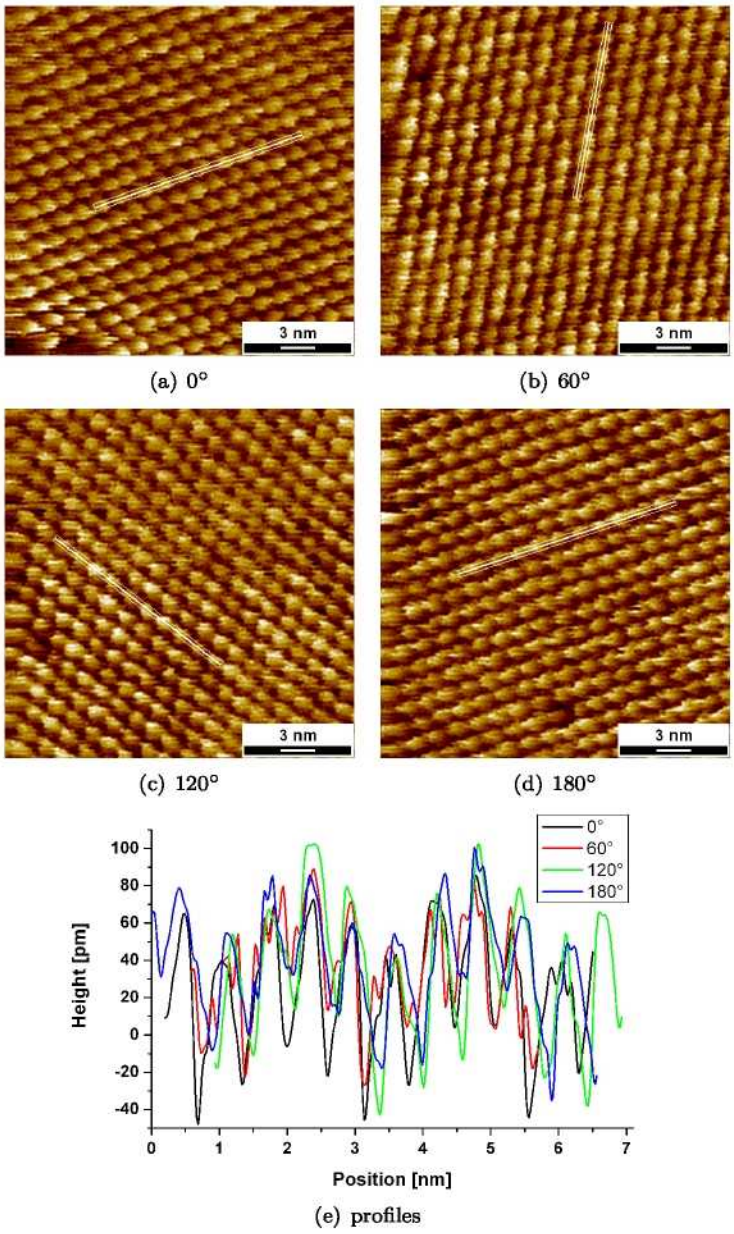

(a) 0° (b) 60°

(c) 120° (d) 180°

(e) profiles

Figure 6.8: Rotated scans of an undecanethiol ($CH_3 - (CH_2)_{10}SH$) SAM on Au(111). The profiles taken at the white bars show four different heights per unit cell regardless of the scanning direction.

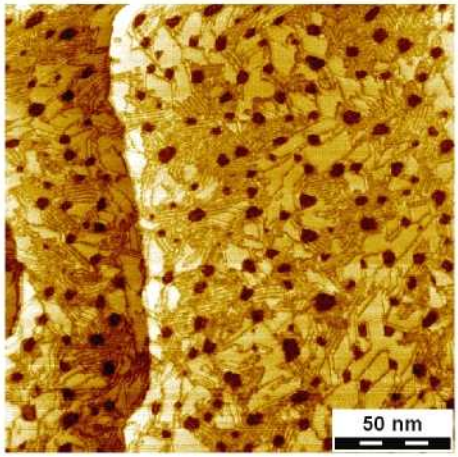

Figure 6.9: STM Topography of a dodecanethiol-SAM annealed for 6,5 h at 79°C in depleted solution. The characteristic features of a solution processed SAM are clearly visible. Besides the substrate step on the left and the small vacancy islands (dark pits), different domains of standing up (homogenous) and lying down (striped) phases can be distinguished.

by directed tip-sample interactions and supports the assumptions made. The new ζ-phase shows, that all four molecules of the unit cell are geometrically or electronically different, pointing towards different bonding to the substrate or different twist angles, supporting the ideas of Liu et al. [122].

6.4 Intermediate $(3\times2\sqrt{3})$-phase

Most experimental studies focus on the assembly process towards saturation and on the structure of a complete monolayer. Long term evolution [125] or even desorption [93, 138] is studied very little, although the structures emerging in these regimes contribute to the understanding of the SAM system by showing structures and dynamics that are not possible or not visible in a complete monolayer. Upon study of long-term annealed SAMs of dodecanethiol on Au(111) by UHV-STM, an intermediate $(3\times2\sqrt{3})$ phase close to desorption is discovered [139].

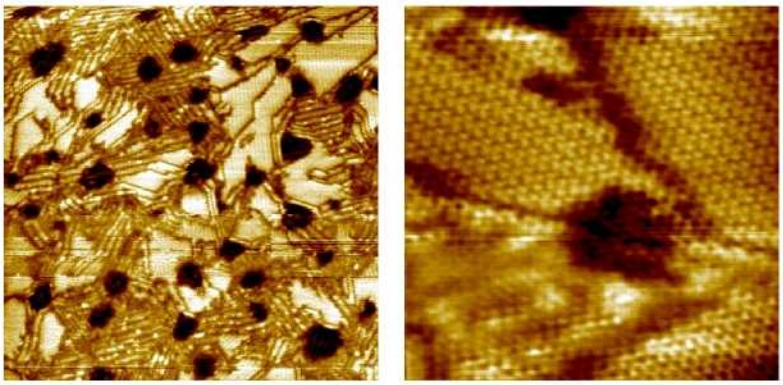

(a) (b)

Figure 6.10: STM Topography scan of a sample prepared as in figure 6.9. In (a) the typical domain structure is visible. The bright, homogenous textures in (a) represent different standing up-phases as the non-hexagonal $(3\times2\sqrt{3})$-phase. In (b) a magnification of the $(3\times2\sqrt{3})$-domains is shown.

In such monolayers with different coexisting phases (figure 6.9), a dense, standing-up phase with a $(3\times2\sqrt{3})$ superlattice is observed. The monolayers are deposited straightforward from solution and annealed in a hot water bath at 77 °C for an elongated period (3-7 h), rinsed with ethanol and directly transferred into the UHV-System.

By annealing under controlled circumstances with a high concentration of excess thiols available in solution very large domains of the c(4×2) - phase, limited only by the terrace sizes of the underlying substrate, are formed. If no precautions are taken the thiol concentration in solution decreases during the annealing process and previously bound thiols are desorbed from the surface. Thus surfaces with sub-monolayer-coverage of alkanethiols, but with very clean and pronounced molecular structures are achieved on the sample. In these layers, domains of different density from lying down and almost completely desorbed phases up to full-coverage phases with saturated density coexist. In our experiment the thiol concentration is depleting incidentally over the course of a long annealing-process (~6:30h) to achieve a partially desorbed monolayer for detailed examination of the various resulting phase structures by STM.

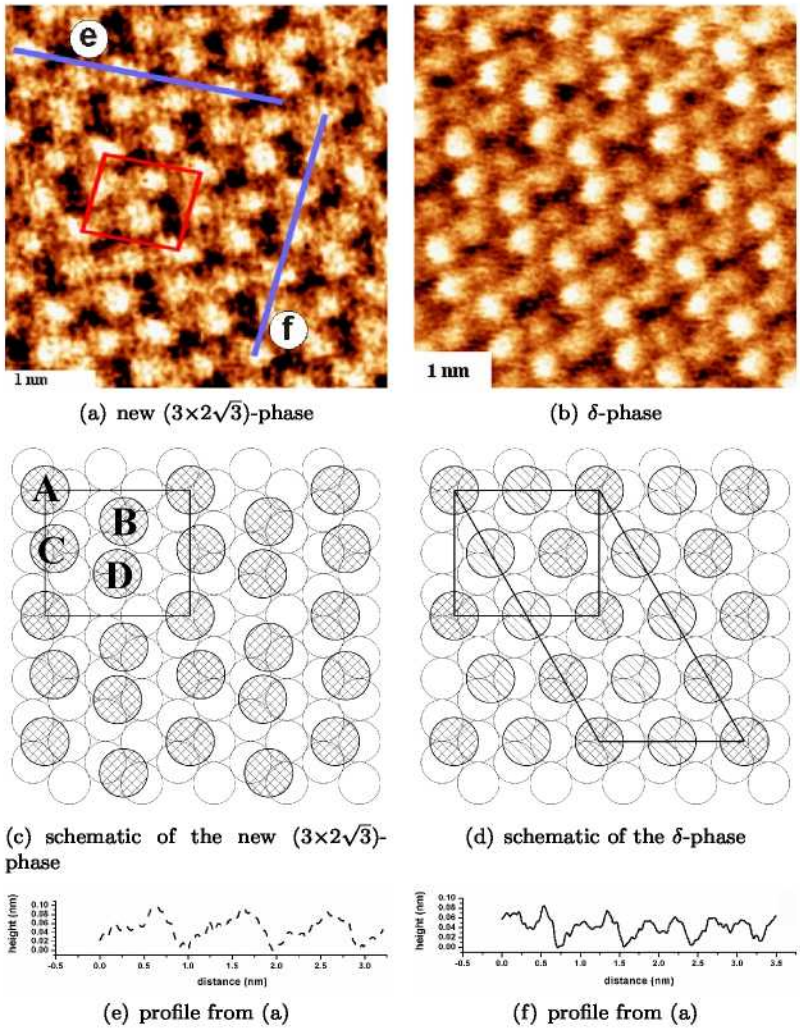

(a) new $(3\times2\sqrt{3})$-phase

(b) δ-phase

(c) schematic of the new $(3\times2\sqrt{3})$-phase

(d) schematic of the δ-phase

(e) profile from (a)

(f) profile from (a)

Figure 6.11: STM scan of the non-hexagonal $(3\times2\sqrt{3})$-phase (a) and the suggested arrangement of the alkanethiol molecules with respect to the underlying Au(111) lattice (c). In (b) and (d) the well known c(4×2) superlattice of alternating heights, which can be named $(3\times2\sqrt{3})$ as well is illustrated. In (a) the lines (e) and (f) mark the profile measurements shown in (e) and (f).

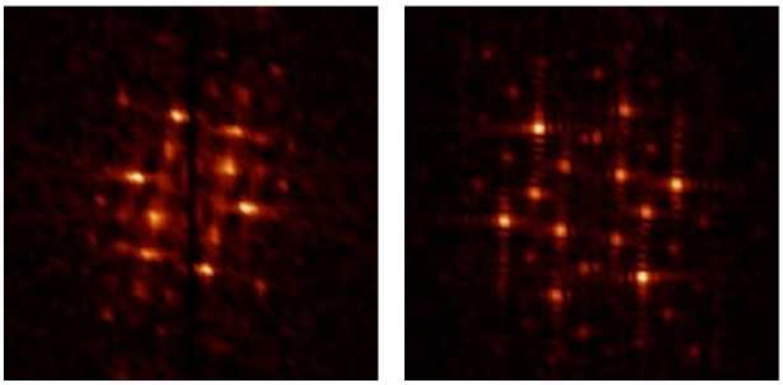

(a) (b)

Figure 6.12: 2d-FFT Spectra of the $(3\times2\sqrt{3})$-phase (a) and the common c(4×2)-phase (b) Taken from the left spectrum (a), the base unit cell vector lengths are 0.849 nm and 0.998 nm compared to theoretical 0.868 nm and 1.002 nm of a suggested $(3\times2\sqrt{3})$-unit cell.

A topography scan of such layers shows features of the underlying gold substrate as well as features of the SAM itself (figure 6.9, 6.10).

The characteristic features, monoatomic terrace steps and vacancy islands are well resolved. On the terraces a mixture of standing-up phases (homogenous texture) and lying-down phases (striped texture) can be distinguished. The domain boundaries are visible as dark lines.

Focusing on full-coverage standing phases, i.e. one molecule per three surface gold atoms or an average area of 0.216 nm^2 per molecule, a new high density structure with a square superlattice is observed. This structure has the same packing density and even the same unit cell size, as the common c(4×2) superlattice structure but does not show hexagonal symmetry[1] (figure 6.10, 6.11). From the Fourier-spectrum (figure 6.12), the size of the unit cell is measured to be 0.849 nm× 0.998 nm compared to theoretical 0.868 nm× 1.002 nm . This difference is within the accuracy of the STM and partially due to limited software resolution of the FFT-spectra. From the surface molecular arrangement it is generally assumed that all sulfur head-groups are bound on three-fold hollow sites

[1]The $(3\times2\sqrt{3})$-phase can also be expressed as a c(4×2)-phase, but is commonly called c(4×2) in literature.

forming a commensurate hexagonal lattice [23]. For the observed, new structure this scheme does not fit. The positions of the molecules in the observed image can not be explained by the common three-fold hollow site placement of the molecules, even if skewing and distortion of the images is taken into account. The relative position of the molecules in the center of the unit cell does not fit. Thus a molecular arrangement as plotted in (figure 6.11) is suggested for the rectangular $(3\times2\sqrt{3})$-structure. The corner molecules (A) are positioned on three-fold hollow sites at the same positions as in the c(4×2)-lattice. In order to match the observed structure, two of the center molecules are placed on a bridge (B) respectively half-bridge (C) position. Molecule (D) is on a different three-fold hollow position. If (A) is on a hcp-site, (D) is on fcc and vice versa (for an illustration of the binding positions see figure 6.3). This structure evolves during the long thermal annealing process in a thermally changed balance between molecule desorption and adsorption. Upon cooling the structure remains in the altered $(3\times2\sqrt{3})$ -state, which is probably stabilized by the observed molecule pairing, more obvious in the line-scans (figure 6.11). Thus we suggest that the described surface phase is an intermediate phase close to desorption. Whether molecule (B) and (C) (figure 6.11) are located on half-bridge or bridge sites is beyond the accuracy of the images obtained. But the experimental observation of bridge-site molecules in a densely packed layer offers new insights into the possible configurations of alkanethiol monolayers, showing that the weak energy barriers between the different adsorption sites can be overcome by ordering forces of the alkane chain and thermal energy. Furthermore the proposed placement reflects a decreased distance between adjacent molecules, like a pairing of two alkanethiols.

6.5 Domain boundaries

Alkanethiol monolayers exhibit a polycrystalline domain structure. The domain boundaries are usually initiated at vacancy islands, larger defects or impurities. Although domain boundaries represent the largest defect area in the monolayer and thus the primary source of errors for possible applications, they are studied rarely. Besides being a difficulty for integration, domain boundaries represent extended defects and offer the opportunity for molecule insertion and surface patterning [140]. In addition, domain boundaries offer the chance to learn about the structure of the molecular layer itself [91,92,122]. Assuming a c(4×2) superstructure

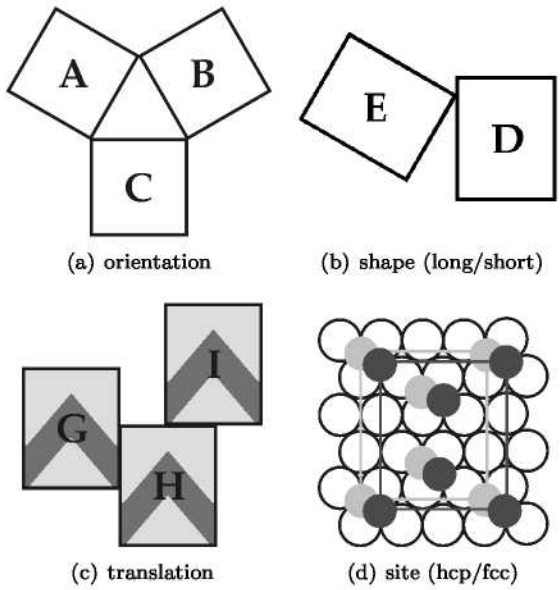

Figure 6.13: Schematics of the basic domain domain boundary types for a rectangular unit cell, due to orientation (a) shape (b), translation (c) and translation plus adsorption site (d).

for the close-packed layer, a variety of different domain boundaries exists, depending on the number of different possible occurences of the unit cell. Rotational boundaries (figure 6.13 (a)) always exist, due to the 120° symmetry of the gold substrate. Since the shape of the c(4×2) unit cell is rectangular, this additional degree of freedom allows a superposition of the rotational and shape depending boundaries, when a rotated domain meets the long side of another domain with its short side (b). If the unit cell consists of different molecules, phase differences due to translation at the domain boundaries become possible (c). Finally the gold offers two different hollow sites for adsorption, allowing for a hcp/fcc shift in the adsorption sites (d). At the boundary between two domains various superpositions of all these differences can meet and form different structures.

The type of transition and thereby the corresponding configurations available for the monolayer can be determined from the molecular struc-

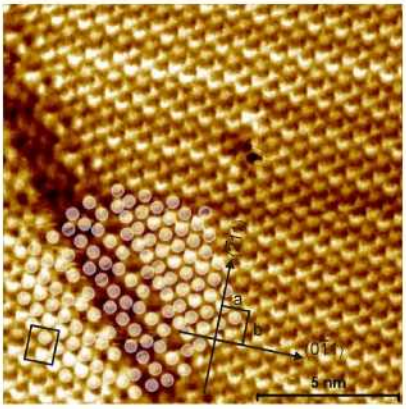

Figure 6.14: $14,1 \times 14,1$ nm^2 STM Topography of a (hcp/fcc) translational domain boundary (darker area). The position of the molecular tail-groups on both sides is emphasized and the unit cells of the respective structure are marked.

ture along a domain boundary. A rotational transition shows a very thin, almost invisible domain boundary, whereas transitions involving a translational difference form a wider boundary up to several tenths of a nanometer [92].

Between c(4×2) domains of a solution processed octanethiol monolayer a translational transition with strong evidence for a hcp/fcc shift is found (figure 6.14) [141]. Both domains to the left and right of the boundary show the c(4×2) structure with a δ-phase characteristic, i.e. two different heights per unit cell (compare with figure 6.5). The unit cell and the gold substrate-vectors are marked in figure 6.14. The tail position of each molecule in the transition region is emphasized by a bright spot. By matching these positions with the substrate lattice, a schematic drawing of the molecular structure can be made (See figure 6.15). The left domain, defined as fcc is marked in red, the right domain, hcp, in blue and molecules in the transition in gray. Taking a closer look at the translational difference between the left and right unit cells reveals a shift of $\frac{1}{3}$ of the a-vector and $-\frac{1}{6}$ of the b-vector, equivalent to a shift of the gold lattice vector a_0 and $\frac{\sqrt{3}}{3}a_0$, leading to a change from hcp to fcc adsorption sites or vice versa. Taking a closer look at the transition

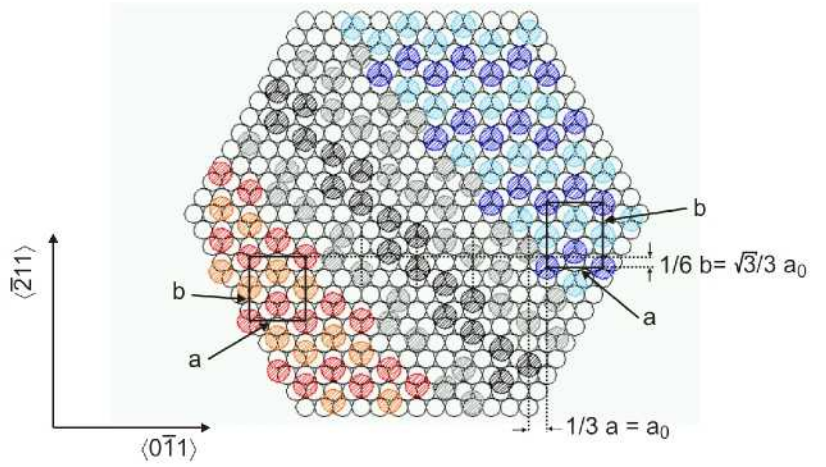

Figure 6.15: Schematic drawing, showing the relation of the unit cells on both sides of the translational boundary observed in figure 6.14. The adsorption sites of the molecules are colored in red and blue, the shade indicating the height of the molecule. The translation of the unit cell is $1/3\,a$ in horizontal direction and $-1/6\,b$ in vertical direction.

molecules, a gradual rearrangement between both domains can be found leading to a line defect with slightly reduced packing density.
This observation of coexisting hcp and fcc phases indicates negligible difference in the binding energies ΔE of fcc or hcp adsorption sites, supporting theoretical calculations with the same result [133, 142].

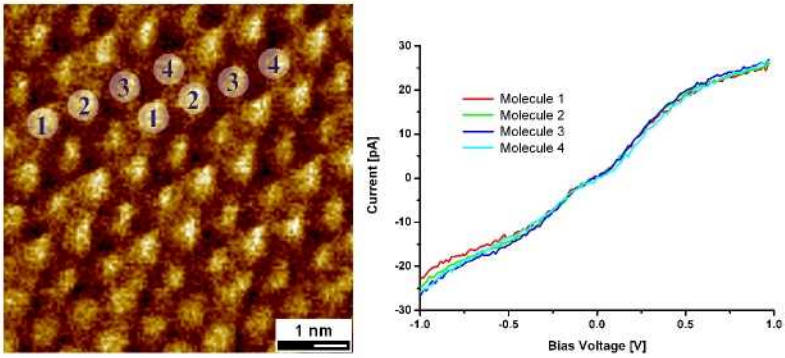

(a) CITS topography image with four selected molecules.

(b) Averaged localized I/V curves from the different molecular sites, denoted as 1-4

Figure 6.16: Atomic resolution CITS measurement of an octanethiol monolayer showing only slight deviations in the conductance, limiting the difference in the LDOS to tiny deviations.

6.6 Spectroscopy

In section 6.3 the different heights of the c(4×2)supercell are discussed. Besides topography measurements spectroscopic measurements at the molecule positions are performed. With CITS (described in section 3.2) multiple I/V measurements with at exact spatial positions are taken simultaneously with the topography signal during one scan. Unfortunately CITS is limited in resolution, since the spectra need to be acquired at a relatively high speed and the tunneling resistance needs to be set higher than necessary for pure spectroscopy, to avoid surface contact during scanning. In the CITS topography shown in figure 6.16a the different molecules of a unit cell are marked 1-4. The (around 100) I/V spectra for the according sites are averaged and displayed in figure 6.16b. The curves show an unusual behavior around the zero point, an artifact due to the low currents and the fast scanning speed. The different curves itself deviate only slightly from each other, leaving room for small variations in the LDOS of each molecule, but eliminating fundamental differences between them.

By current-distance spectroscopy (See section3.2) the current-decay length of the alkanethiols is measured (figure 6.17). Upon approach towards the

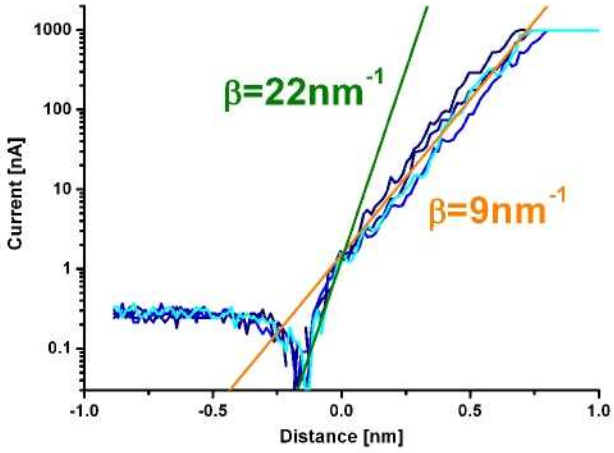

Figure 6.17: Current-distance spectroscopy of a dodecanethiol monolayer, showing a current jump at the point of contact and a current-decay constant of $\beta = 9$ for the monolayer.

surface the current is below the noise limit of the preamplifier and the signal contains only noise. In close distance to the surface the current jumps with the slope of the vacuum decay constant of $>20\text{nm}^{-1}$ until the contact point is reached. From the point of contact the tip starts penetrating the alkanethiol monolayer and the current slope resembles the current-decay constant of the alkane. The experimental value of $\sim 9\text{nm}^{-1}$ is in good agreement with the values reported in literature of $\sim 8.8\text{nm}^{-1}$ [143], $\sim 7\text{nm}^{-1}$ [144] and $\sim 11\text{nm}^{-1}$ [145].

6.7 Conclusion

Self-assembled monolayers of different alkanethiols are assembled from solution onto the surface of (111)-oriented gold thin film substrates. The resulting monolayers are studied by UHV-STM and characterized with molecular resolution. From topographical measurements a new c(4×2) unit cell with four different molecules has been identified and named ζ-phase. Looking at the assembly and annealing process, a second new phase close to desorption is identified, pointing towards the

high mobility of the alkanethiols on the gold surface and a possible variation in the bonding positions. By studying the domain boundaries of alkanethiol monolayers, coexisting domains of hcp and fcc bound molecules are found indicating a negligible difference in binding energy between the two bonding sites. A better understanding of the monolayer properties, especially at the interesting interface has been achieved and published [116, 146], pointing to the existence of four different molecules per unit cell, different possible adsorption sites and indicating the equivalence of the hcp and fcc sites for adsorption. The electrical structure of the distinguable molecules inside a unit cell is probed by CITS measurements, showing only slight differences for each adsorption site. By current-distance spectroscopy, the electronic decay constant of the monolayer is measured and verified with literature values, to serve as spectroscopic reference for future measurements.

7 Structural and Electrical Properties of Ferrocenes

The electrical, chemical and structural properties of molecular thin films, small bundles of molecules or even single molecules receive a lot of scientific attention. Since patterning in the nm-range is possible with advanced lithography methods from semiconductor technologies and scanning probe microscopes with atomic resolution are available, the use of molecular properties for future applications becomes feasible. During the first steps towards a possible integration, the structural properties of a thin film and the molecule itself need to be characterized. For the formation of more complex molecular electronic systems, active elements are needed, besides conducting and insulating ones. One class of molecules, promising the capability to store and manipulate charge are molecules, containing redox active centers as ferrocene. The ferrocene moiety can be easily oxidized and reduced in solution and can act as a donor in larger charge transfer environments.

Ferrocene, an organometallic complex abbreviated as Fc ($FeC_{10}H_{10}$), consists of two negatively charged cyclo-pentadiene rings bound to a central iron ion by coordination bonding. The compound was first discovered by Pauson et al. in 1951 [147], who found a remarkably stable molecule with a strong metal-organic bonding and interesting properties. Strong scientific interest in the new research field led to the nobel prize in chemistry in 1973 for G.Wilkinson for his work on organometallic complexes, especially ferrocene [148]. The prominent feature of ferrocene is its well behaved oxidation/reduction cycle, together with its high stability in different surroundings. Till today, ferrocene is used to provide an internal standard for electrochemical measurements in solution [149].

The idea to combine the electrochemical functionality of ferrocene with the environment of self-assembling alkanethiols was first realized by Chidsey et al. [150]. He successfully prepared mixed layers of mercaptoalkylferrocenes and the corresponding mercapto-alkanes of the same length to achieve self-assembled monolayers with an electro-active surface.

For layers incorporating only a small amount of ferrocenes, the expected undisturbed redox-behavior is measured in solution, whereas for higher fractions the redox-features broaden and shift, showing increasing intermolecular interaction and disorder. This system of a mixed monolayer of ferrocenes and alkanethiols on gold, studied in solution offers an interesting setup to study the charge transfer rates of the spacing layer via electrochemical measurements [151–153]. Furthermore it provides access to the assembly dynamics of a mixed layer by monitoring the redox behavior during layer formation [154, 155]. Ferrocenes are also used as probes for in-situ modification of the SAM surface [156]. Uosaki et al. further studied mercaptoundecanyl-ferrocene monolayers with dynamic ellipsometry and found a film thickness of 2.91 nm, indicating multilayer formation and observed an increase in thickness upon anodic oxidation, attributed to an uptake of ions from solution [157]. Further evidence for the formation of multi-layers and a changing thickness with changing redox state was shown by Viana et al. [158]. The mentioned thickness change, upon oxidation was attributed to a swing of the ferrocene end-group by Yao et al. [159]. In 2001, Gorman et al. discovered a negative differential resistance (NDR) effect for SAMs of Mercaptoundecanyl-ferrocene under dodecane by scanning-tunneling spectroscopy (STS) [160]. This effect was further investigated by Tivanski et al. in 2005, who found a correlation between monolayer charging and the NDR effect [161]. In the same year, Lindsay et al. attributed the NDR effect to oxygen in the measurement environment, causing the electrochemical generation of a conducting path [162]. Ferrocene functionalized monolayers are also manufactured by attaching ferrocenes to functional groups via a surface chemical reaction [156]. As part of a larger charge transfer complex, ferrocene is used as a gateable bridge moiety [34]. Chemisorbed ferrocene thin films are interesting for a wide range of applications, due to their stability and charge transfer properties. They provide a good contact interlayer between organic photovoltaic cells and inorganic substrates [163], might be used for memories [164], as catalysts for chemical reactions [165] or as spin valve in spintronics [33].

7.1 The matrix isolation approach

To study the electronic properties of individual molecules, different setups are used (See section 2). In order to access the electronic properties of a single molecule or a group of molecules organized in a self-assembled

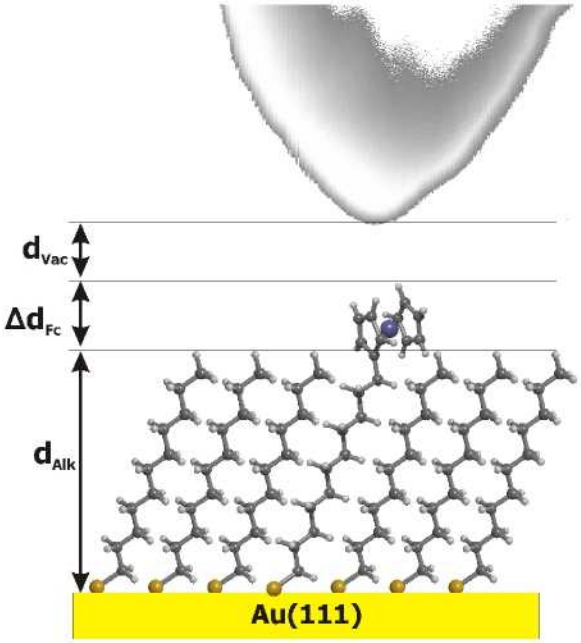

Figure 7.1: The matrix isolation approach for measurements on individual molecules. A insulating and rigid matrix of host-molecules spatially fixes a similar functional molecule or bundle of molecules. By using the STM tip, access to the isolated assembly is possible and electronic properties can be measured.

monolayer, a well-defined and stable environment has to be provided during the measurement. One possible way is the embedment of functional molecules into an insulating matrix and their subsequent characterization by STM [166–170]. In this study, mercaptoalkyl-ferrocenes with an insulating alkane spacer and an electro-active ferrocene moiety as top group are embedded into a topographically well-defined matrix SAM of alkanethiols (See figure 7.1). The alkanethiol monolayer spatially separates the functional molecules and fixes them in an upright and stretched position. The resulting structure provides a defined insulating layer of a thickness d_{Alk} and a ferrocene moiety with the known dimensions of Δd_{Fc} on top. By adjusting the setpoint, the vacuum tunneling distance d_{vac} can be tuned (See figure 7.1). Once a mixed monolayer of reasonable quality is deposited and the molecular features are resolved, the well-known electrical transmission and height of the alkanethiol SAM can be used to evaluate the charge transfer characteristics of the ferrocene moiety, using the surrounding alkanethiols as a spectroscopic reference.

7.2 Structural properties

Organic self-assembled monolayers on various substrates are subjects of a large amount of studies with scanning probe methods, whether as single component or mixed layers [168, 171, 172]. Considerably less studies deal with the adsorption of metal-organic molecules, despite the obvious potentials of such systems. Excellent examples for SPM studies of physisorbed metal-organics are the works of Hipps et al. [42,173]. Even less is known about the structural properties of chemisorbed mercaptoalkyl-ferrocenes. Monolayers of physisorbed ferrocenes on metallic substrates have been studied at low temperature [174–176]. For ferrocenes on Au(111) physisorbed at low temperatures, layers of decomposed ferrocenes are observed by Braun et al. [177]. Physisorbed monolayers of alkyl-ferrocenes and alkane-bridged di-ferrocenes on Ag and HOPG have been examined by Wedeking et al. [178,179] and represent the only real space images of ferrocene-derivative monolayers besides earlier rudimentary studies [180] The structure of bulk ferrocene crystals is studied by x-ray diffraction and a disordered phase is observed at room temperature, whereas at lower temperatures a triclinic crystal structure is described by Dunitz et al. [181,182]. So far no molecularly resolved STM images of chemisorbed mercaptoalkyl-ferrocenes are available and their exact structure is still under debate.

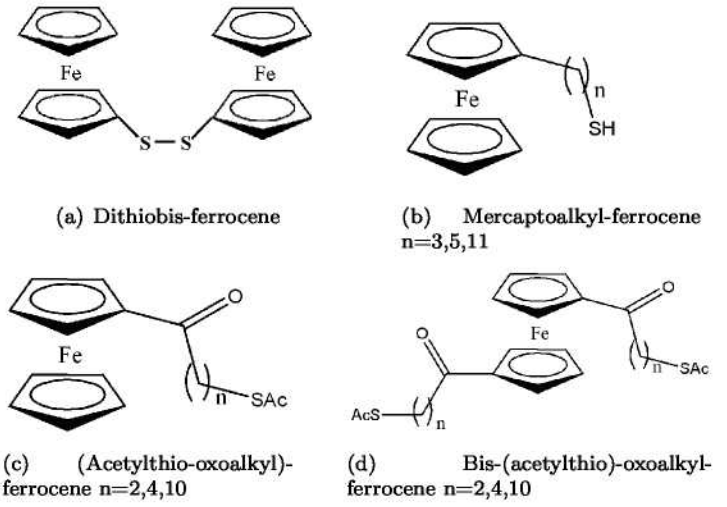

(a) Dithiobis-ferrocene

(b) Mercaptoalkyl-ferrocene n=3,5,11

(c) (Acetylthio-oxoalkyl)-ferrocene n=2,4,10

(d) Bis-(acetylthio)-oxoalkyl-ferrocene n=2,4,10

Figure 7.2: Available ferrocene derivatives. All molecules with alkane spacer are available with different spacer-chain lengths.

7.3 Ferrocene derivatives

To address the structural properties and the balance mechanisms of ferrocene monolayers different ferrocene derivatives are studied. The first substance examined is Dithiobis-ferrocene (as shown in figure 7.2a), two plain ferrocenes linked by a disulfide group. The disulfide splits upon chemisorption [24, 120] and single ferrocene moieties are chemisorbed at the substrate via sulfur-gold bonds. The disulfide form protects the otherwise reactive sulfur sites during storage and deposition. In addition three groups of ferrocenes with different alkane spacers are studied. A homologous series of mercaptoalkyl-ferrocenes (figure 7.2b) with spacer lengths of n=3,5,11 carbon atoms are characterized and for readability abbreviated as FcC3SH, FcC5SH and FcC11SH in the following. For these molecules the assumed NDR-effect was observed [160] and disproved [162]. In addition (Acetylthio-oxoalkyl)-ferrocenes with spacer lengths n=2,4,10 (figure 7.2c) are investigated, representing the molecules originally studied by Chidsey et al. [150]. These molecules contain an additional carbonyl-group between the alkyl-spacer and the ferrocene moiety, which withdraws electrons from the backbone and thereby

changes the molecular electrical properties. The reactive sulfur of the molecules is protected by an acetate protection group, which is removed upon chemisorption. The carbonyl containing molecules are abbreviated as FcOC3SAc, FcOC5SAc, FcOC11SAc. To increase the stability, bis(acetylthio)-oxoalkyl-ferrocenes with two spacer-chains are also examined (figure 7.2d). These molecules are also available with n=2,4,10 and are abbreviated as Fc(OC3SAc)2, Fc(OC5SAc)2 and Fc(OC11SAc)2. All ferrocene derivatives were synthesized and purified at the Institute for Anorganic Chemistry at the RWTH-Aachen according to the methods of Uosaki, Kim, Knox and Chidsey et al. [150, 154, 183, 184].

7.4 Experimental

Monolayers of the above mentioned ferrocene derivatives are deposited from solution on crystalline, (111)-oriented Au thin films, prepared as described in chapter 5 or in [73]. The ferrocene derivatives are synthesized and purified at the Institute for Anorganic Chemistry at the RWTH Aachen and are used as received. For mixed monolayers undecanethiol ($CH_3(CH_2)_{10}SH$) and octanethiol ($CH_3(CH_2)_7SH$) are used as matrix molecules (Sigma-Aldrich). All compounds are solved in ethanol as millimolar solutions. For coadsorption experiments, the solutions are mixed in different ratios and the samples are exposed to the mixture for about 24-48 h. For the insertion experiments, freshly prepared samples are exposed to an alkanethiol solution for 24 h and then transferred to a mixed or a pure solution of alkanethiol and ferrocene for 10-120 minutes. When noted, the samples are heated in solution or in vacuum to increase the layer quality and desorb physisorbed molecules from the surface. During assembly, the samples and solutions are handled under controlled argon atmosphere in a glove-box, if technically possible. After deposition, the monolayers are dipped in hot ethanol, thoroughly rinsed and immediately transferred to vacuum. The samples are characterized with a JEOL 4500 UHV-STM using homemade electrochemically etched tungsten tips in UHV at a base pressure of 5×10^{-10} mbar. Topographical images are done in constant-current mode at bias voltages around $\pm$1-2 V and tunneling currents between 30-100 pA.

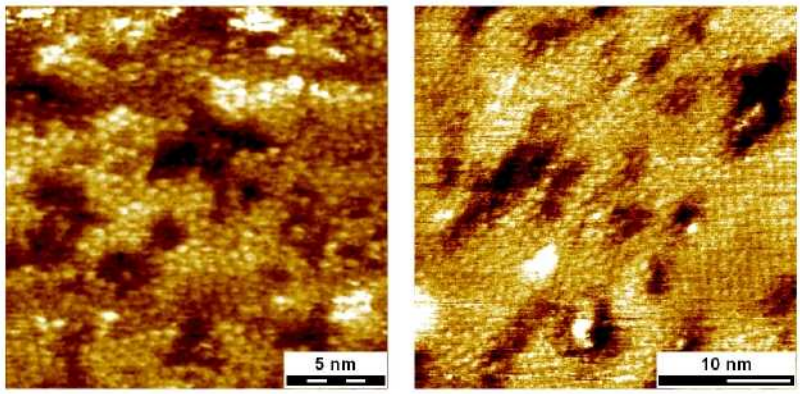

(a) no order visible, blurry features (b) vacuum annealed (15 h, ~150 °C)

Figure 7.3: Chemisorbed monolayer of Dithiobis-ferrocene on Au(111). A knobby surface structure, attributed to single ferrocene molecules can be seen. Upon extended annealing in vacuum, the disordered structure (a) transforms into a ordered rectangular structure (b).

7.5 Ferrocene self-assembled monolayers

7.5.1 Dithiobis-ferrocenes

Upon straightforward deposition, all studied ferrocene-derivatives form chemisorbed, disordered thin films with a blurry and unstable surface. By varying the deposition conditions, ordered monolayer domains are achieved for the ferrocene derivatives without acetate protection group. For extended assembly time (6d) and vacuum annealing (1 h at ~110 °C), monolayers of pure dithiobis-ferrocenes are formed (figure 7.3). Upon further annealing for 15 h at 150 °C, the disordered structure transforms into an ordered structure with a rectangular unit cell. Both structures remain blurry and show only a weakly pronounced surface corrugation, indicating vibrational, rotational or electrical noise in the layer, in accordance to the observations for ferrocene crystals, described in section 7.2. The lattice-vectors of the observed structure are around 0.83±0.05 nm and 0.78±0.05 nm, the slightly hexagonal inter-ferrocene spacing from the disordered monolayer is in the range of 0.7-0.8 nm. Both values are reasonable for the distance between two ferrocene molecules,

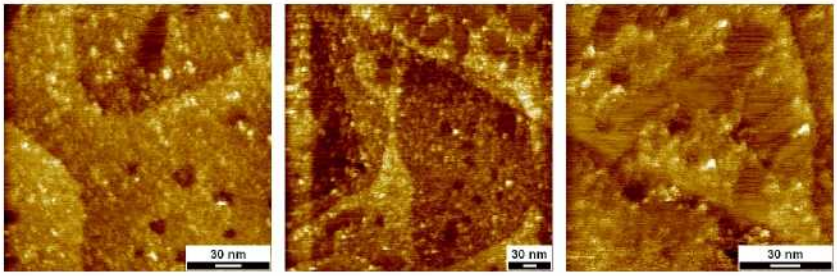

(a) no order visible, blurry features (b) small ordered domains, flat areas in the upper part (c) larger ordered domain with visible substructure

Figure 7.4: Topography of a chemisorbed FcC5SH monolayer after solution annealing. Ordered domains of darker, flat texture in a disordered, blurry environment, which is characteristic for ferrocene monolayers.

indicating a single ferrocene molecule per measured surface bump. The observed ferrocene monolayers are difficult to prepare and a lot of bulky adsorbates are still present on the surface. Furthermore, only small ordered domains together with areas showing only short ranged ordering are found and thereby indicate a weak ordering force between the molecules. To increase the degrees of freedom for the adsorbed monolayer and optimize the intermolecular interaction, alkane spacer groups are introduced.

7.5.2 Mercaptoalkyl-ferrocenes

As observed for the pure ferrocenethiols, the mercaptoalkyl-ferrocenes form disordered, loose layers, as shown in figure 7.4(a). The STM topography images show the terraces of the underlying substrate, etch-pits and a blurry surface texture. The visibility of substrate features points towards a reasonable layer thickness in the range of one to five monolayers. The etch-pits visible as dark depressions are generated during the chemisorption of sulfur on the gold substrate and thereby indicate the presence of sulfur-gold bonds. The blurry surface does not show any clear features, which can be attributed to geometrically or electronically unstable features or physisorbed surface adsorbates, including ferrocenes forming a multilayer structure. According to the disordered crystal structure of ferrocene and the multilayer formation observed in

literature, ferrocene derivatives do not form ordered monolayers spontaneously, but tend to be disordered and likely incorporate loosely bound ferrocene on the surface.
Monolayers of mercaptoalkyl-ferrocenes, FcC3SH, FcC5SH and FcC11SH display similar disordered surface structures. After annealing of such samples in solution at 60-80 °C, small domains of ordered molecules appear in the surrounding disordered structure, especially for the shorter molecules FcC5SH and FcC3SH (figure 7.4), visible as darker areas of homogenous texture. The apparent height difference between the low, ordered areas and the bright, blurry environment further indicate disorder and beginning multilayer formation in the surrounding layer (figure 7.4).

In annealed monolayers of FcC3SH, large domains with crystalline structure are observed (figure 7.5). The ordered surface areas show two different surface textures. Both exhibit a rectangular superstructure, one with elevated peaks in the corners of a unit cell (figure 7.5a,c), the other one is less pronounced and features a depression on one side of the unit cell, resulting in a striped appearance of the monolayer (figure 7.5b,d). Both structures are observed consecutively on the same area and cannot be changed into each other by bias variation, nor are they observed in parallel. They have very similar dimensions and only slight distortions of the angle are visible. With respect to the absolute accuracy of the STM, the unit cell dimensions of both structures are assumed to be identical. Therefore the structural differences between elevated corners and striped structure are contributed to tip changes by a rearrangement of the tip apex or uptake of a ferrocene molecule to the tip apex during the scan. Thus the superelevation of the corner molecules is believed to be of electronic and not of geometric origin (figure 7.5). Both structures feature a rectangular unit cell with average lattice vectors of 2.54 ± 0.05 nm and 1.52 ± 0.05 nm as shown in figure 7.6. The interior of the unit cell shows little structure and cannot be specified further from the available real space data. In the fourier-transform image figure 7.5(c), the rectangular superstructure is obvious in the overall frequency pattern. In addition, the fourier spectrum shows four prominent peaks marked with black circles, indicating a basic rectangular lattice with halved lattice vectors. In figure 7.6 the inverse lattice of a structure, consisting of a rectangular lattice (green) and a rectangular superstructure (black dots) of doubled periodicity is simulated and shown in (figure 7.6b). The pattern of the larger lattice is drawn as white spots, the points where both lattice structures coincide are marked in color. The first order points

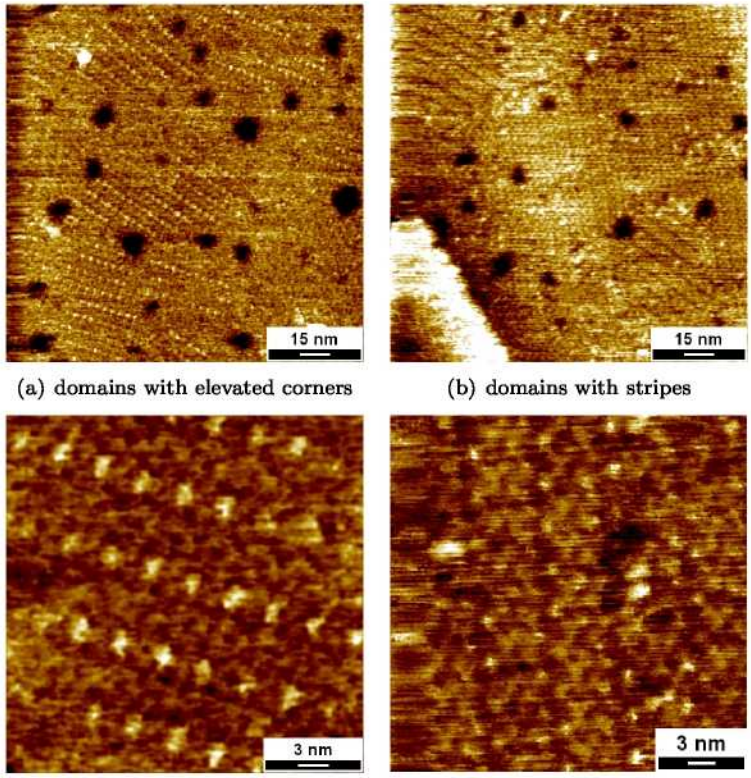

(a) domains with elevated corners (b) domains with stripes

(c) zoom in, elevated corners (d) zoom in, stripes

Figure 7.5: Large domains of the two different rectangular FcC3SH structures observed. The left, dotted structure features elevated corner molecules, whereas the structure on the right features a structure of striped appearance. All scans are measured with bias voltages between 0.9-1 V and currents of 50-60 pA.

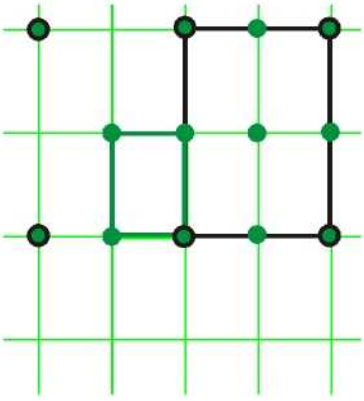

(a) superposition of small (green) and large (black) rectangular structures

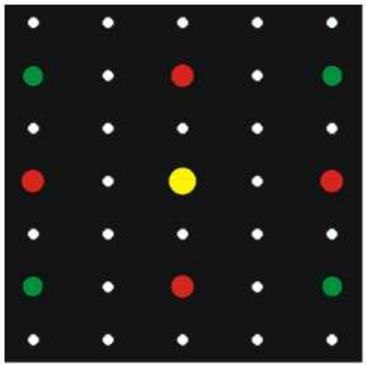

(b) inverse lattice for both lattices, at the colored dots, both structures coincide

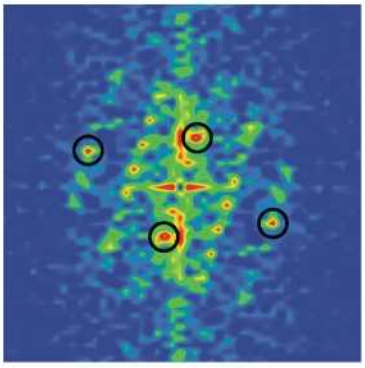

(c) FFT-image of the STM scan, showing increased brightness for the first order coinciding spots (black)

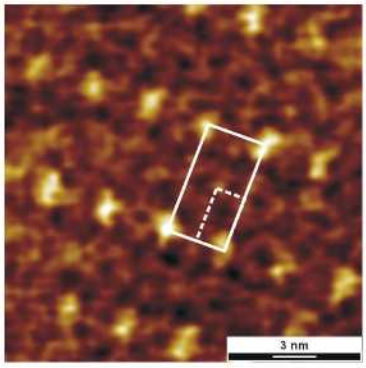

(d) STM topography, showing the large and the small rectangular structure, modeled in (a)

Figure 7.6: FFT spectrum and topography image of the Fc-C3SH superstructure. The simulated inverse lattice and the corresponding pronounced spots in the FFT indicate a smaller rectangular structure as the basic structure.

of the base lattice are marked red and correspond to pronounced spots in the FFT-image (figure 7.6c), marked with black circles. Thus, from FFT data, a division of the large unit cell into four basic cells as basic structure is indicated.

For FcC3SH bulk crystals, x-ray diffraction measurements were successfully performed at the Institute for Anorganic Chemistry, RWTH Aachen, and the structure of the FcC3SH crystals was determined (figure 7.7). The ferrocenes form a monoclinic crystal with four molecules per unit cell. In [100]-direction, the crystal consists of closely packed ferrocene layers, stacked alternatingly upon each other. Each layer is either ferrocene or thiol terminated, i.e. the ferrocenes are oriented with the ferrocene moiety in [100]-direction or with the thiol moiety in [100]-direction. One unit cell is formed by a ferrocene terminated layer and a flipped thiol terminated layer on top, leading to alternating interface planes of either ferrocene-ferrocene or thiol-thiol adjacencies (figure 7.7(b)).

Looking at a thiol-terminated (100)-crystal plane, the in-plane base vectors of the x-ray unit cell a^*=1.29 nm and b^*=0.77 nm describe a rectangular lattice of sulfur atoms in the (100)-plane (figure 7.7). Comparing these distances with the Au(111) surface lattice, a close match is found. The crystalline unit cell can be placed commensurably on the Au(111) surface by 2% stretch in a^*-direction and 0.7% compression in b^*-direction, offering equivalent adsorption sites for the corner molecules and causing only moderate stress in the unit cell (figure 7.8). Therefore adsorption of the ferrocenes in a configuration, similar to a (100)-layer of the bulk crystal is expected. This assumption is further confirmed by the congruence of the surface unit cell, measured for the chemisorbed species on the Au(111) surface (a=2.54±0.05 nm, b=1.52±0.05 nm) and the quadrupled (100)-unit cell of the bulk crystal (a=2.58 nm, b=1.53 nm) as marked in figure 7.7(a).

Thereby a $\begin{pmatrix} 2 & 3 \\ -4 & 1 \end{pmatrix}$ unit cell with respect to the underlying Au(111)-lattice is suggested as interfacial structure, forming a superstructure of quadrupled size on the surface. The observed agreement between measured surface superstructure, crystal lattice vectors and substrate symmetry leads to the conclusion, that the FcC3SH molecules chemisorb in an arrangement very similar to their bulk crystal phase. Due to low contrast inside the quadrupled super-cell, the exact placement and orientation of the internal molecules cannot be defined. The lack of contrast is related to a certain amount of disorder and flexibility of the ferrocene

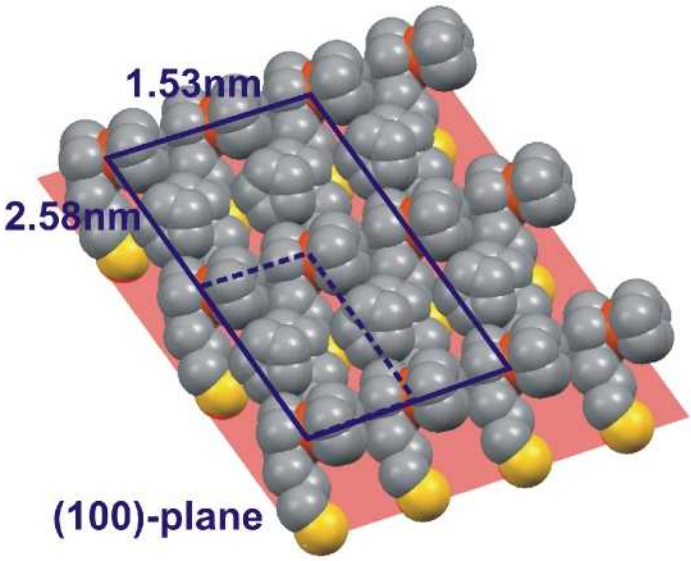

(a) Layer of a single crystal cut along the (100)-plane with a thickness of a half unit cell, exposing a ferrocene terminated surface.

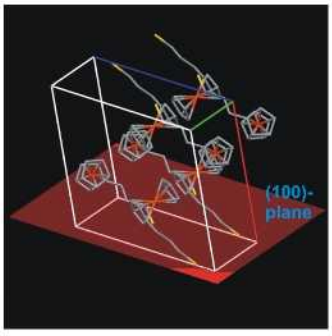

(b) Structure of the complete unit cell, the red (100)-plane is given again for orientation.

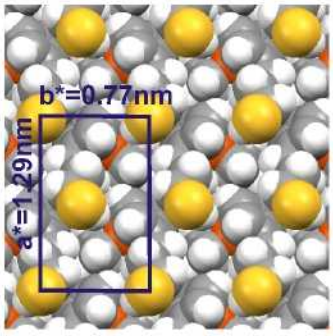

(c) Thiol terminated (100)-crystal plane, with the basic unit cell marked in blue.

Figure 7.7: Schematics of x-ray diffraction data for FcC3SH crystals. On a ferrocene terminated (100)-surface (a), the distances of a four times larger unit cell are marked, agreeing with the size of the superstructure for chemisorbed molecules. The dashed rectangle marks the unit cell of the single crystal, shown in (b) and (c). In (c) a thiol terminated (100)-surface is shown. The marked unit cell can be matched with the Au(111) surface, causing only minor stress in the monolayer.

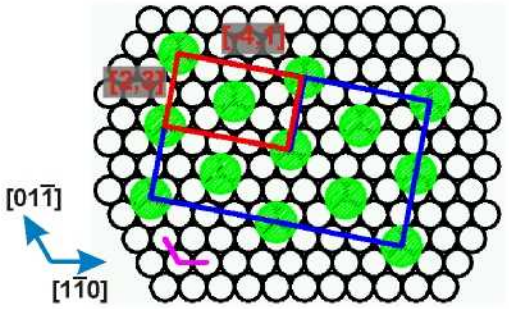

Figure 7.8: Schematic placement of the FcC3SH molecules on Au(111). The suggested unit cell at the interface (blue) causes only minor stress compared to the crystalline unit cell (red). The resulting quadrupled cell of the superstructure is marked in blue. The Au(111) vectors are noted and the relative vectors of the unit cell are given in red. Other slightly different molecular surface arrangements are possible within the accuracy of the STM, but cause a larger distortion of the crystalline unit cell and therefore are less likely.

moieties on the surface. The tendency of ferrocenes to show fuzzyness when imaged, is already observed for the disordered bulk crystal structure of pure ferrocenes. It is probably further aggravated by the slight distortion of the crystal unit cell and the lack of stabilizing neighbors, compared to the bulk, caused by the symmetry break at the surface. The interpretation of the molecular positions inside the unit cell is further complicated, since the exact spatial relation of a heightened spot in the STM to the real position of the molecule is not known. The peak in the shape of the LDOS, imaged by STM, can deviate in space from the molecular center or even combine with a second molecule, especially in the presence of π-electron rich systems like ferrocene. Thus the exact internal structure of the unit cell can only be defined with supporting theoretical and experimental data.

The suggested surface structure of the FcC3SH SAM closely resembles a (100)-plane in the bulk crystal and therefore presents the perfect substrate for the attachment of excess ferrocenes from solution. After the first layer is chemisorbed on the gold substrate the layer growth is stopped by self-termination, but changes its dynamics and physisorbed multilayer-formation is started, consistent with literature observations.

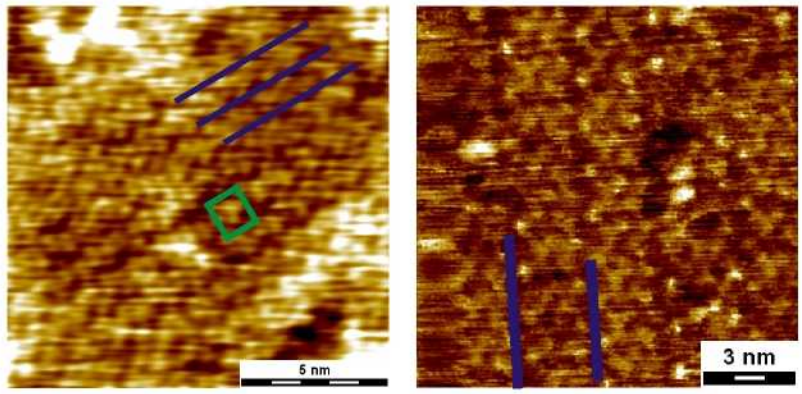

(a) FcC5SH (b) FcC3SH

Figure 7.9: Comparison of monolayer structures for FcC5SH and FcC3SH, showing a characteristic striped pattern marked in blue, caused by a depression on one side of a unit cell and slightly intensified corner molecules. The unit cell of the FcC5SH molecules is marked in green.

Mercaptoalkyl-ferrocenes with longer spacer-chains are significantly less ordered, then the ones with shorter chains. Whereas for FcC3SH relatively large ordered areas with multiple domains are formed, only smaller ordered areas in a surrounding blurry structure are visible for FcC5SH, as shown before in figure 7.4. The surface structure of FcC5SH looks very similar to the structure of FcC3SH, featuring the same surface trenches and bulky texture, as shown in figure 7.9. The unit cell drawn in figure 7.9(a) with unit cell vectors of 1.16 ± 0.05 nm and 1.05 ± 0.05 nm appears to be smaller than those of the shorter chain FcC3SH. Due to lack of resolution the exact molecular structure and thus the number of molecules within the unit cell cannot be determined. Therefore the marked FcC5SH unit cell might consist of less molecules than the FcC3SH structure, indicating a decrease in packing density.

Due to limited resolution of the ordered areas and insufficient supporting material no structure is proposed for FcC5SH SAMs, whereas the related system and the resemblance of the observed surface structures support a similar layer structure and formation mechanism as observed for FcC3SH.

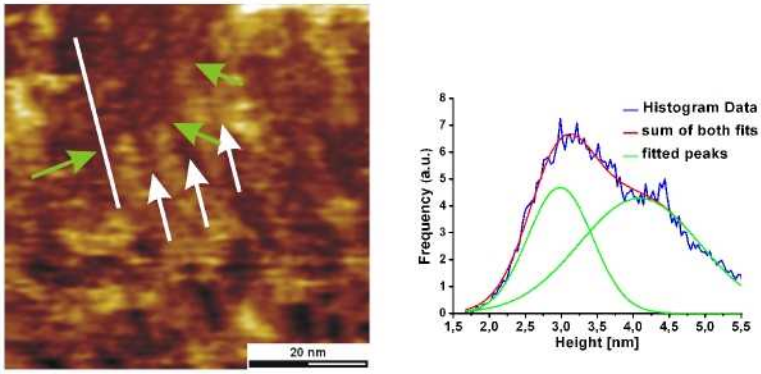

(a) STM topography of an FcC11SH mono/multilayer on Au(111)

(b) Height histogram of the layer, with two fitted gaussian peaks

Figure 7.10: Multilayer formation in SAMs of FcC11SH. Striped monolayer features marked white, change their height at the sites marked by green arrows. A local histogram shows a height difference of 1.09 nm between the first and the second monolayer, by fitting two gaussian peaks in the topography histogram.

For FcC11SH even less structural data is available. Probably due to the increased tunneling resistance and increased mobility due to the longer spacer-chains, no clear monolayer structure is discovered. In analogy to the assumptions for the structure of the FcC5SH monolayer, the described properties of the FcC3SH layer are probably also valid for the FcC11SH layer. Upon closer inspection of small less blurry features on the surface evidence for multilayer formation is found. In figure 7.10 a blurry pattern slightly resembling the striped structures of the shorter chain mercaptoalkyl-ferrocenes is observed. The elevated stripes change their height in a discrete step, marked by the green arrows. This height change is supposed to happen due to local adsorption of a second ferrocene layer, as indicated by the bulk crystal structure. A histogram of the local scan shows a height difference of $\sim 1.0 \pm 0.1$ nm between both layers, as visible in the histogram (figure 7.10(b)).
Ordered monolayer formation of ferrocene-derivatives is very fragile and is observed only for FcC3SH, FcC5SH and weakly for FcC11SH. The spatial hindrance of the bulky ferrocene moiety and the weak interaction between the ferrocenes impede the formation of an ordered self-

assembled monolayer. Monolayer formation is further complicated by the increased interaction between free and chemisorbed ferrocenes leading to incorporation of excess molecules, forming multilayer assemblies. By solution annealing, ordered domains can be achieved for the mentioned derivatives.
For pure ferrocenesulfides, the lack of freedom and interaction energy, caused by the missing alkane spacer moiety seems to prevent ordered layer formation. With longer chain spacers the layers are less ordered, probably due to increased stress and defects in the changeover region from alkane to ferrocene. They incorporate more excess ferrocenes and start multilayer formation. Upon observation of molecules with carbonyl moiety and acetate protection, ordered monolayers are not visible, probably due to further increased steric hindrance and interactions of the carbonyl-group plus possible impurities caused by the acetate-group. The degree of order, found for mercaptoalkyl-ferrocene monolayers, depends on the spacer-chain length. Since ferrocenes are likely to incorporate additional physisorbed molecules into the layer, an annealing step (60-80 °C in solution) is crucible for ordered thin films. The temperature needs to be high enough, to promote ordering in the thin film and desorb remaining excess molecules. If the temperature is too high, ferrocene molecules are desorbed and more disordering is induced. For longer spacer-chains, this process window is getting smaller, so the preparation of ordered layers is getting increasingly difficult.

7.6 Mixed monolayers

The creation of mixed monolayers is a powerful way to adjust the assembly dynamics and the properties of an organic monolayer. By diluting functionalized alkanethiols with their basic counterparts, the interaction of the functional groups in solution and on the surface can be decreased. For diluted monolayers of mercaptoalkane-ferrocenes in alkanethiols, a better defined redox behavior and layer stability has been shown by electrochemical measurements on chemisorbed ferrocene monolayers [152, 153]. Dilution of functional monolayers offers the chance to tune the density of the functional group on the surface and thereby its electrochemical and structural properties. Furthermore, molecules which do not readily form ordered monolayers by themselves can be integrated. Thus functional monolayers for potential applications can be achieved, which are structurally better defined, more reproducible and show less

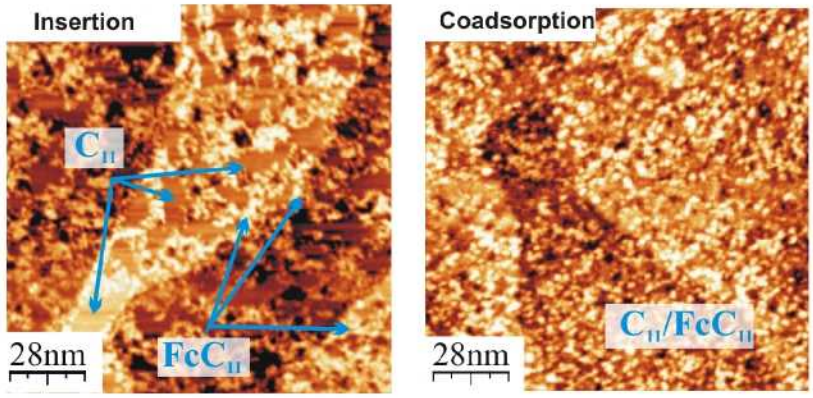

(a) insertion (b) coadsorption

Figure 7.11: Coadsorption of FcC11 and C11 at a ratio of 1:3. The brighter, crumbled surface is attributed to the ferrocene end-groups (a). Two step insertion process of FcC11SH into undecanethiol (b). Both monolayers show substrate steps and etch-pits (dark depressions), indicating a chemisorbed monolayer.

defects. For electrical studies the matrix isolation approach, as described above (section 7.1), offers the possibility for characterization of phase-separated islands or individual isolated molecules. Finally the mixture of two molecules offers a chance for the formation of supra-molecular units and new hybrid structures with new and interesting properties. For mixed layers a determination of the local structural properties is extremely important for characterization.

7.6.1 Insertion vs. coadsorption

Mixed monolayers can be prepared in sequential or parallel manner. Either a layer of one single component is deposited first and the guest component is inserted in a second step or both species are coadsorbed at the same time. In this section the assembly behavior of mixed, full-coverage layers of mercaptoundecyl-ferrocenes (abbreviated as FcC11SH) and alkanethiols by insertion and coadsorption is compared.

For both processes, the sample topographies show mono-atomic substrate steps as well as etch-pits, resulting from the assembly process.

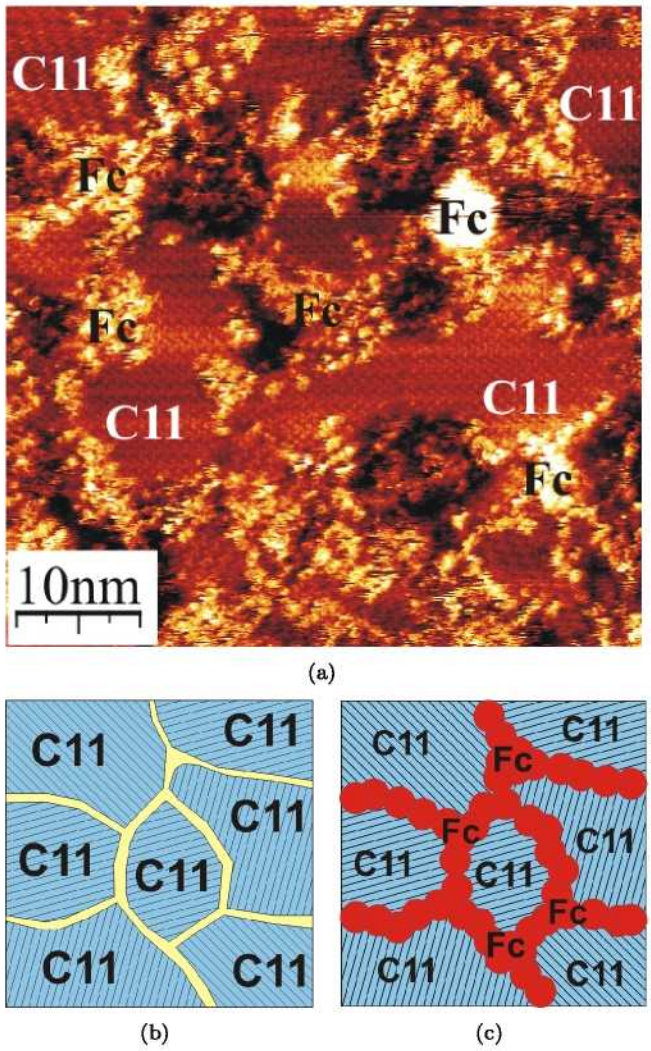

Figure 7.12: Mesh-like insertion of FcC11SH along domain boundaries of a undecanethiol (C11) SAM. A dense alkanethiol monolayer forms a dense monolayer consisting of different domains (b). Along their edges preferential adsorption takes place, leading to accumulated ferrocene ribbons on the surface (c). On the surface of the large intact C11 domains, the characteristic c(4x2) surface reconstruction of an alkanethiol SAM can be observed (a).

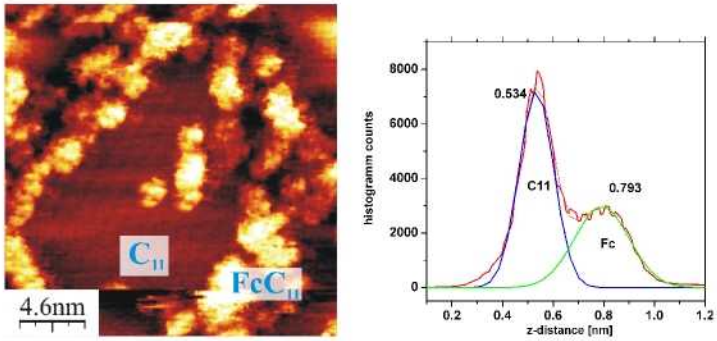

Figure 7.13: Topography of FcC11SH inserted into undecanethiol. In the center, an ordered C11 domain is visible, surrounded by a ferrocene surface ribbon. On the height distribution histogram two distinct peaks are visible. Fitting two Gaussian peaks to the graph results in an average height difference of 0.26 nm.

The visibility of these surface features indicates a chemisorbed monolayer of homogenous thickness (figure 7.11). The coadsorption experiment yields layers with dense, elevated features, attributed to the ferrocene end-groups (figure 7.11(b)). The measured heights of the elevated spots agree with the expected height of embedded ferrocenes. However, even for diluted ratios, no molecular resolution of the matrix monolayer could be achieved and a decreased ordering or impairing of the imaging process due to the entangled ferrocene/alkanethiol structure is assumed. The surface of the insertion-processed sample shows a mesh-like structure of ferrocene ribbons running along the alkanethiol domain boundaries (figure 7.11(a)). During the insertion step, a combination of desorption of chemisorbed molecules and insertion of new molecules from solution occurs, which takes place preferentially at defect sites. Thus, the existing alkanethiol domains remain highly ordered, whereas the inserted ferrocenes accumulate along domain boundaries and edges of steps and etch-pits (figure 7.12). The quality and order of the monolayer with inserted FcC11SH molecules can be increased by careful tempering in solution at around 50 °C. At elevated temperatures, slow desorption of the alkanethiols takes place, which is avoided by using a 3:1 mixture of 1 mmol/l undecanethiol and FcC11SH during the insertion

step. The mixed monolayers, produced by this insertion method, show uniformly ordered alkanethiol domains, which exhibit the characteristic surface reconstruction of a closely packed, standing-up alkanethiol monolayer (figure 7.12, 7.13). The height difference between FcC11SH and undecanethiol is determined from a topography histogram (7.13). The extracted height difference at a tunneling setpoint of 1.65 V/ 35 pA is roughly 0.26 nm, compared to an expected physical length difference of ~0.3 nm between the two molecules, taken from single crystal x-ray measurements. Considering a slightly tilted arrangement and differences in the electronic decay constant, these numbers agree quite well. The height difference indicates the presence of single ferrocene end-groups on the SAM surface. However, due to the structural properties of the ferrocene ribbons, showing local bulky structures, the formation of aggregated clusters of multiple molecules on the surface remains likely for the higher and more disordered parts of the ferrocene ribbons. The observed decoration of the domain boundaries with ferrocenes proves an interesting point for the dynamics of the insertion process. The insertion and exchange mechanism in the insertion step starts at domain boundaries and other defects, leaving the interior of the domains unchanged.
Mixed monolayers of FcC11SH and undecanethiol molecules are prepared by coadsorption and by a two-step insertion process. The coadsorption process results in a dense, mixed monolayer with an entangled structure of ferrocenes and alkanethiols. This process leads to difficulties at high-resolution imaging, probably due to agglomeration and surface instabilities. The two-step insertion process yields a monolayer with crystalline alkanethiol domains, separated by mesh-like ferrocene ribbons formed along the domain walls. The height of the ferrocenes at the boundaries points towards separated ferrocene end-groups and to no or little agglomeration of multiple molecules on the surface of the SAM.

7.6.2 Phase-separated islands

Upon stronger annealing of mixed monolayers, different structures from phase-separated islands to various mixed assemblies are observed. Dithiobis-ferrocene (referred to as FcSSFc), consisting of two ferrocene moieties connected via a disulfide, is inserted into an annealed octanethiol-monolayer at a temperature of 60 °C for 13 minutes. During the annealing step, a part of the alkanethiol layer is desorbed and phase-separated islands of pure ferrocenes are formed. The mixed monolayers show the characteristic features of alkanethiols on Au(111) as described before

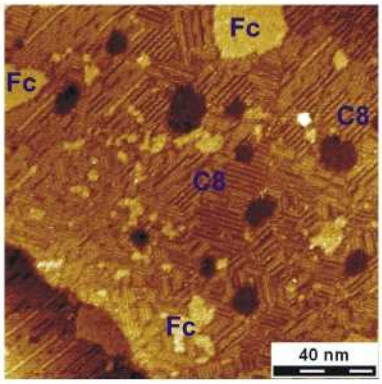

(a) Several phase-separated structures

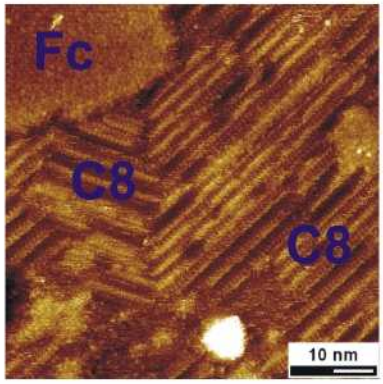

(b) Ferrocene island in octanethiol

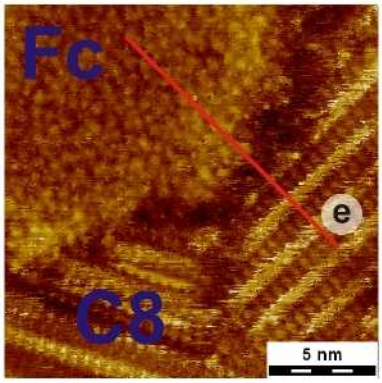

(c) Different surface textures of the island and the surrounding layer

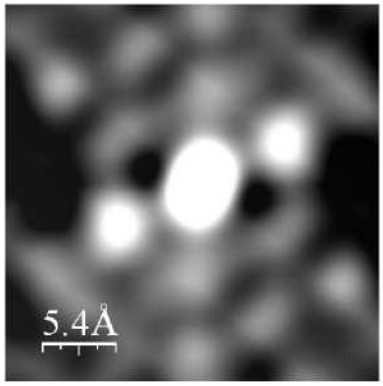

(d) Autocorrelation analysis of the island structure

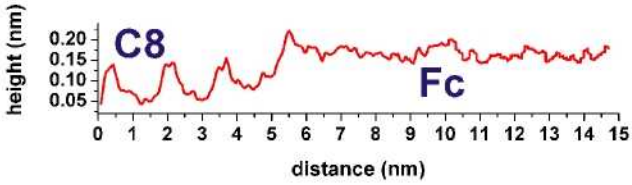

(e) Profile of the island in (c)

Figure 7.14: Islands of dithiobis-ferrocene in octanethiol, showing a knobby surface texture. Upon autocorrelation of the surface features a weak hexagonal order is visible for the island structure.

(chapter 6), a characteristic striped texture for the lying-down alkane phase and islands with a knobby surface structure (figure 7.14). The octanethiol SAM around the island resembles a striped ($p \times v3$)-phase of lying-down molecules. The islands show a knobby surface structure and are assumed to consist completely of ferrocenes. The homogenous texture, the lack of alkanethiol features on the island, as well as the undisturbed order of the surrounding monolayer support the assumption of a clear phase-separation. Autocorrelation of the Fc-island structure (figure 7.14c) shows a weak hexagonal order and an average distance of 0.67 nm between the centers of two nearest neighbors, which corresponds well to the STM apparent size of a ferrocene measured by Waldfried et al. [174], the estimations by Chidsey et al. [150] and the observations made for a pure monolayer before (section 7.5.1).

As a first approximation, the ferrocene moiety can be considered as a small sphere of ~0.67 nm diameter, so the measured slightly hexagonal structure would be the expected order for a close-packed layer. Assuming hexagonal structure and a nearest neighbor distance of ~0.67 nm, an average surface area of ~0.39 nm^2 per molecule can be calculated, corresponding to roughly one half of the surface density of a full-coverage alkanethiol monolayer with an average area of ~0.216 nm^2 per molecule. From the homogenous height of the island, a layer thickness of exactly one monolayer can be derived and multilayer-stacking as observed for full-coverage mercaptoalkyl-ferrocenes [158] can be excluded (figure 7.14e). The structure and intermolecular spacings are in close agreement with the intermolecular spacing of ~0.7 nm observed for a disordered monolayer of dithiobis-ferrocene in section 7.5.1 (figure 7.3).

Upon variation of the insertion time and temperature, the distribution and the amount of embedded ferrocenes can be controlled. For lower temperatures the ferrocenes are more isolated. For the chosen higher temperature, domain separation and coalescence take place and islands of different surface texture appear. Dithiobis-ferrocenes are inserted into an alkanethiol monolayer and small islands of a homogenous monolayer are formed in the surrounding SAM. The islands show a close-packed random structure with an average intermolecular distance of ~0.67 nm or an area of ~0.39 nm^2 per molecule, in close agreement to the pure monolayer described in 7.5.1, indicating a complete phase-separation inside the island. This phase-separation, already taking place for moderate annealing conditions indicates a high mobility of the embedded molecules inside the monolayer and a lower ferrocene-alkanethiol interaction energy.

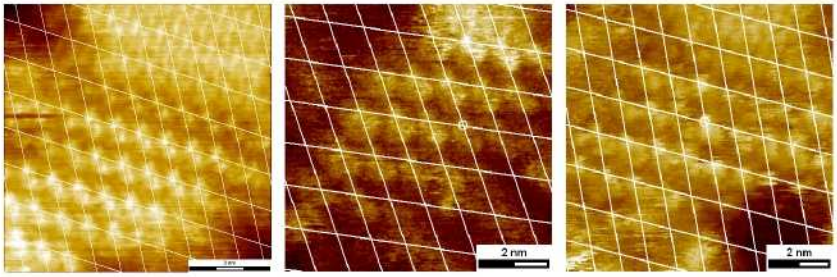

(a) Fc(OC11SAc)2 (b) FcOC11SAc (c) FcC11SH

Figure 7.15: Crystalline domains of different ferrocene-derivatives, embedded into alkanethiol SAMs. The islands show a very similar surface with lattice constants of a=1.4±0.06 nm, b=1±0.05 nm and an angle of 60±2°.

7.6.3 Ordered islands

Analogous to the insertion of the FcSSFc-molecules, described in the previous section, FcC11SH, FcOC11SAc and Fc(OC11SAc)2-derivatives are inserted into undecanethiol and dodecanethiol monolayers. After moderate annealing at 60-70 °C, the mixed layers show typical features. The highly ordered SAM structure of alkanethiols, ferrocene surface ribbons, disordered areas, isolated small groups of molecules and sporadic, small islands of the ferrocene-derivatives with a crystalline order are visible. These ordered islands are rather small and rare, but are observed for different samples and for all three mentioned ferrocene derivatives. In close accordance, all three types of ferrocenes show the same surface structure of elongated shapes, assumed as single ferrocene moieties on the surface. The visible unit cell is a parallelogram with lattice constants of a=1.4±0.06 nm, b=1±0.05 nm and an angle of 60±2°. The resulting area of ~0.7 nm^2 per molecule seems reasonable, compared to ~0.5 nm^2 per molecule for the ordered FcC3SH (section 7.5.1) and 0.39 nm^2 for FcS, taken into account the observation of relatively large, lowered spaces between the ferrocene moieties in figure 7.15. The lower density of the surface ferrocenes suggests the packing-density is rather determined by the alkanethiol spacer-chains then by the ferrocene end-groups or a closely entangled structure, as for the FcC3SH crystal.

An obvious feature of the ordered islands is the pairing of the ferro-

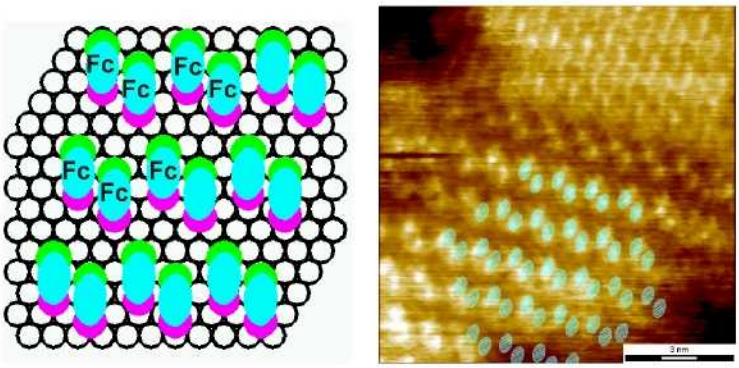

(a) schematic of placement (b) overlay of schematic and STM

Figure 7.16: (a) Schematic of the suggested placement for the Fc(OC11SAc)2 molecules with respect to the gold lattice. The green and pink dots represent the chemisorbed spacer groups, the bright blue ovals the associated ferrocene moiety. (b) Overlay of the bright blue ferrocene structure, matching the STM scan.

cene end-groups on the surface. After comparing distances and known structures, a molecular arrangement for the observed ordered domains is proposed. Since each ferrocene moiety of the Fc(OC11SAc)2 is associated with two alkane spacer-chains, the two ferrocene moieties are assumed on top of four alkanethiol chains in the same arrangement as in a c(4×2) unit cell. This assumption closely reassembles the distance of a ferrocene pair on the surface (figure 7.16). The c(4×2)-cells with the ferrocenes on top are spaced to meet the distances from the STM scans. To match the distances in the short direction, every second cell is placed on a intermediate adsorption position and thereby doubling the unit cell. The resulting structure proposed for ordered islands of Fc(OC11SAc)2 is shown in figure 7.16. Interestingly the structures for the single spacer-chain ferrocenes are very similar to the Fc(OC11SAc)2 structure with double spacer chains (figure 7.15). Therefore a mixture of the single spacer-chain ferrocenes and the surrounding alkanethiols is assumed to form the observed island structure for the ferrocenes with a single spacer-chain.

Besides the phase-separated islands a number of spots is observed in the mixed layers, indicating the existence of small groups and individual

ferrocene molecules in the alkanethiol monolayer. The number and size of the islands is much smaller than for the ferrocenes without spacer-chain, discussed in section 7.6.2. The hindered phase-separation resulting in monolayers with only a few and small islands, observed for the ferrocenes with long alkane spacers, emphasizes a decreased interdiffusion of ferrocenes and alkanethiols. The described effect is attributed to a higher interaction energy between the ferrocenes with spacer-chain and their surrounding monolayer than for the ferrocenes without spacer-chains described before.

7.6.4 Voltage dependent features

For the ordered islands of Fc(OC11SAc)2 in undecanethiol, bias-dependant imaging of the phase-separated islands is performed. Upon a change of the bias voltage in constant-current mode the topography of the crystalline domain is changed. In high-resolution images showing only a few molecules, the emergence and disappearance of additional peaks in the topography scan is observed (figure 7.17). The always visible, paired, bright peaks are attributed to the ferrocene moieties on the surface. The peaks are slightly elongated to the upper left direction and for increased bias their orientation is changed to an elongation towards the upper right (compare 1 V and 1.6 V, marked by ellipses). This change reflects either a reorientation of the molecule, or the incidence of higher molecular energy states into the tunneling energy range. Next to the primary spots, darker spots of similar size and periodicity (marked blue) are observed for low bias and vanish completely for higher bias, which is probably due to an increased conduction of the more prominent features, compared to the lower ones. In addition, a small, bright (marked red) feature is only visible for a bias of 1.2 Volt, which is of unclear origin, but might be contributed to the oxygen of the carbonyl-groups. The observed changes in the molecular features show, that the molecule responds to the applied electrical field and the electronic structure of the molecule shows localized features in space and in energy. An exact interpretation and explanation of these measurements is not possible by STM alone and can be achieved only in combination with theoretical calculations and supporting analytical measurements. Still the observed evolution of features in the STM measurements demonstrate the sensibility of the method and the setup to resolve sub-molecular features and indicates the presence of localized energy states of the molecule in the energy range, accessible by the STM measurements.

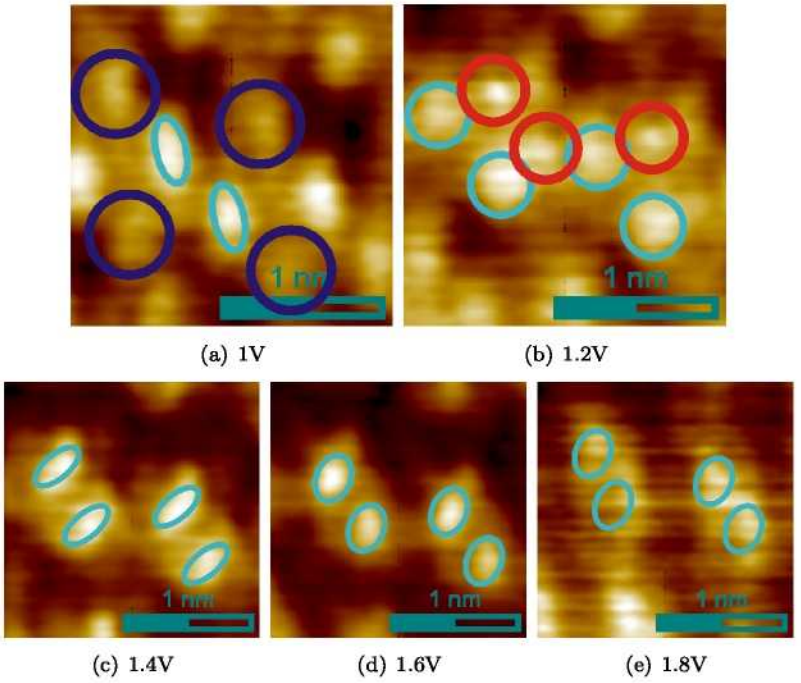

(a) 1V (b) 1.2V

(c) 1.4V (d) 1.6V (e) 1.8V

Figure 7.17: High-resolution, bias dependent images of a phase-separated Fc(OC11SAc)2-island, showing the appearance of a voltage dependent feature, marked by the red circles. In addition the contrast of the prominent peaks increases and the side peaks (marked blue) vanish. The bias dependence of features indicates a spatially different electronic structure of the molecule.

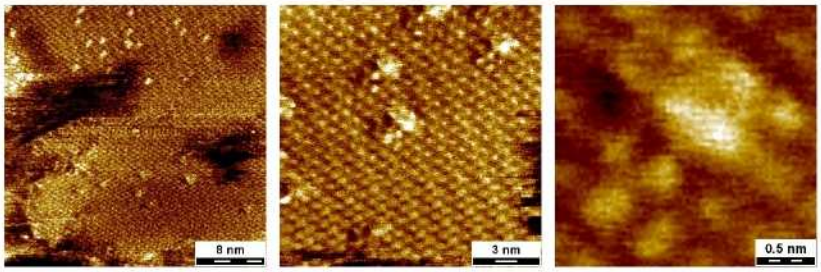

(a) Typical surface structure of alkanethiols, showing additional bright spots

(b) The brighter spots correspond to single, embedded ferrocene molecules

(c) Correlation averaged zoom of an embedded single molecule

Figure 7.18: STM topography scan of a mixed monolayer of FcC11SH and undecanethiol. The surface shows the alkanethiol monolayer structure with single ferrocene molecules embedded by coadsorption.

7.6.5 Embedded single molecules

To observe a single molecule by the matrix isolation method (section 7.1) a high-quality matrix monolayer with well separated functional molecules is needed. Whereas the insertion process yields ribbons of ferrocenes along the domain boundaries, the coadsorption process yields layers of poor order and tends towards phase-separation. For matching lengths of spacer-chain and surrounding monolayer, the interdiffusion of the mixed layer, leading to phase-separation, is minimized. For FcC11SH in undecanethiol, very diluted monolayers with ordered structure are successfully prepared by solution annealing in undecanethiol solution for $\sim$1 h at 60 °C in a closed container, after monolayer deposition from a mixed solution (1:10 Fc:Alkanethiol). In STM images of such layers (figure 7.18), undistorted c(4×2)-alkanethiol structures with embedded single molecules are observed. Around the bright spots, associated to the ferrocenes, the surface atoms of the alkanethiols are resolved and slightly brightened in the proximity of the ferrocene moiety. The size of the prominent spots is slightly larger than those of the alkanethiols and is attributed to single, embedded FcC11SH molecules. The density of the embedded ferrocenes depends strongly on the initial concentration, the deposition and annealing times and temperatures.

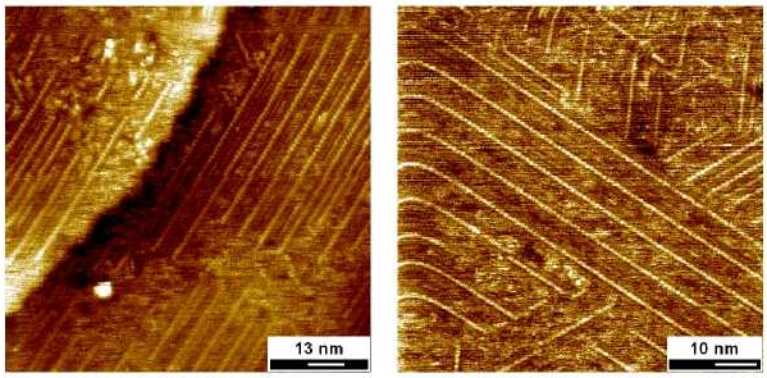

(a) FcOC3SAc and octanethiol (b) FcC5SH and octanethiol

Figure 7.19: Hybrid phases of octanethiol and ferrocene derivatives. The surface shows a striped pattern corresponding to the lying-down octanethiol phase with additional features in between the bright rows.

7.6.6 New hybrid structures

For samples deposited from mixed solutions with a long insertion step at elevated temperatures (~1:30 h at 60 °C solution temperature), partially desorbed structures are observed, which are formed due to the lack of alkanethiols in the annealing solution. In difference to the ferrocene layers compared so far, the alkanethiols as well as the ferrocene derivatives lie flat on the surface. In these relaxed layers, the packing density is not high enough to maintain a standing-up configuration of the molecules. Compared to full coverage phases, the ordering energies are in a different regime with additional interactions of the molecular backbone to the substrate. Low coverage alkanethiols are known to form ordered, striped structures [94–96] of $(p \times \sqrt{3})$-symmetry, with p depending on the length of the molecule and on the exact configuration of the lying-down layer [185, 186]. The striped pattern, observed by STM is caused by the exposure of the gold-sulfur bonding states forming bright features, that merge into elevated stripes on the surface. For octanethiols a periodicity of 2.71±0.06 nm, corresponding to a p value of 9.4±0.2 would be expected [185]. For a mixed monolayer of octanethiol and FcOC3SH a lying-down hybrid phase with a similar periodicity of 2.9±0.2 nm is found (figure 7.19), indicating a slightly stretched geometry. This phase

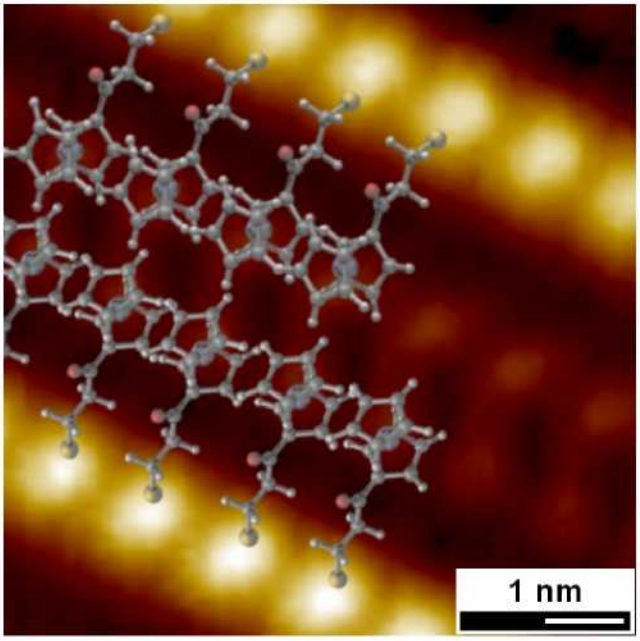

(a) High resolution STM image and schematic overlay of the ferrocenes forming the striped double row phase

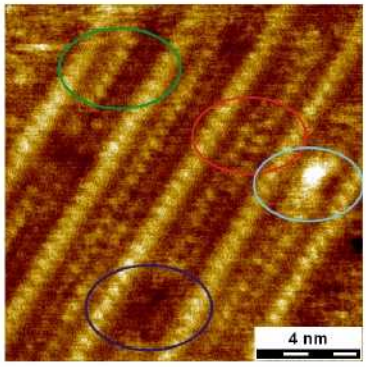

(b) Striped double row structure and typical hybrid structures marked in color.

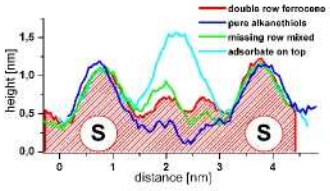

(c) Profiles of the hybrid structures observed in (b).

Figure 7.20: STM topography scans of a hybrid structure of FcOC3SAc and octanethiol. The surface shows a striped pattern corresponding to the chemisorbed sulfur atoms of a lying-down alkanethiol phase. Between the higher stripes, double rows of the ferrocene headgroups appear.

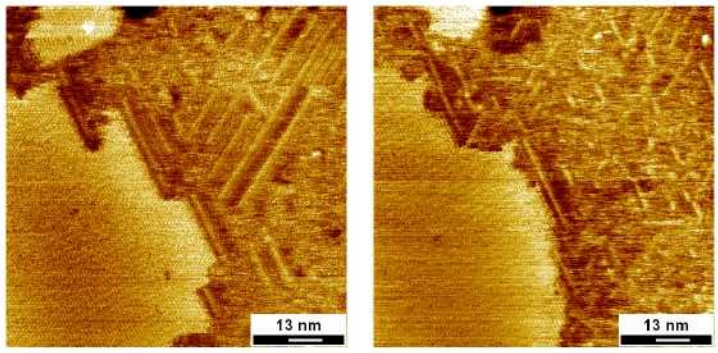

(a) before CITS-measurement (b) after CITS-measurement

Figure 7.21: Hybrid structure of octanethiol and FcOC3SAc, before and after a CITS-measurement from -2 V to 2 V. The image in (a) shows a standing-up alkanethiol domain with straight boundaries and neighboring domains of the hybrid structure. After the CITS-measurements (b) the order of the hybrid-phase is almost destroyed, whereas the alkanethiol-phase is only affected at the boundary.

closely resembles the lying-down alkanethiol phase, but shows additional features between the alkanethiol stripes (figure 7.20(a)), which appear as a dotted double row. For the fully featured double row, a pure ferrocene phase with a molecular placement of the ferrocene molecules, as shown in (figure 7.20(a)) can be assumed. Since a lying down structure is not observed for pure ferroceneylalkanethiols, a template moderation by the surrounding alkanethiols is involved into the formation of such monolayers. Besides the fully featured double row, different hybrid structures formed by partial replacement of the ferrocene derivatives by alkanethiols as shown in figure 7.20(b) and (c) can be observed. The central double row is replaced by a single row or vanishes completely. Furthermore, additional adsorbates can be found in between the alkanethiol stripes, indicating a preferential adsorption of additional molecules in the area between the stripes. These different hybrid structures can be explained by certain defect mechanisms. The double row, as marked in red (figure 7.20(b) and (c)) shows two intact ferrocene peaks in the profile. The single row shows a ferrocene ferrocene peak on one side and a missing peak, corresponding to a substitution of the ferrocenethiol

by an alkanethiol on the other side, resulting in a single row profile (marked green). Occasional pure alkanethiol structures show no peaks (dark blue), whereas a preferred adsorption of large features between the rows leads to a lagre peak in the profile (light blue).
The observed structure is stable during scanning under normal imaging or storage conditions, but is sensible to increased stress. In figure 7.21, an area showing the hybrid structure is imaged under normal conditions, then a CITS scan, alternating the voltage from 2 to -2 Volt is done and the area is imaged again under normal conditions. As can be seen easily, the formerly ordered hybrid phase is disordered after the voltage treatment, whereas the ordered standing-up alkanethiol domain, visible on the left, remains intact and is only affected in the boundary region.
For a mixture of alkanethiols and ferrocene derivatives a new hybrid structure is observed for the lying-down phase. The hybrid phase is similar to the well known striped phases and features ordered lines of ferrocenes with a relatively large spacing. Such lines of functionalized molecules might be useful for surface patterning and may show interesting conduction behavior as the semiconducting benzene rows of Wolkow et al. [187].

7.6.7 Layer stability

In early experiments, the controlled modification of a ferrocene layer by the STM tip is examined and mixed, disordered monolayers of Dithiobisferrocenes and octanethiols are prepared by long time insertion (2:30-6:00 h). These monolayers are disordered, but exhibit a well-defined surface in contrast to single component monolayers, by avoiding multilayer formation. While scanning the surface at higher bias voltages, a modification of the surface is observed. After scanning a smaller part of the sample with a setpoint voltage of 3.5 V and 0.5 nA, a well-defined, elevated square is visible on the surface (figure 7.22). Such features already evolve for lower setpoints, but are nicely pronounced over 3 V/0.5 nA. The observed brighter features cannot be removed by scanning with a lower or reversed bias. Thus the bright features are attributed to an irreversible change of the monolayer at the elevated area and a probable complete destruction. Due to the structural properties and the large elevation, the risen features are likely to be caused by gold aggregates, pulled out of the substrate. These observations of structural instability at higher voltages, need to be taken into account for further structural or spectroscopic studies.

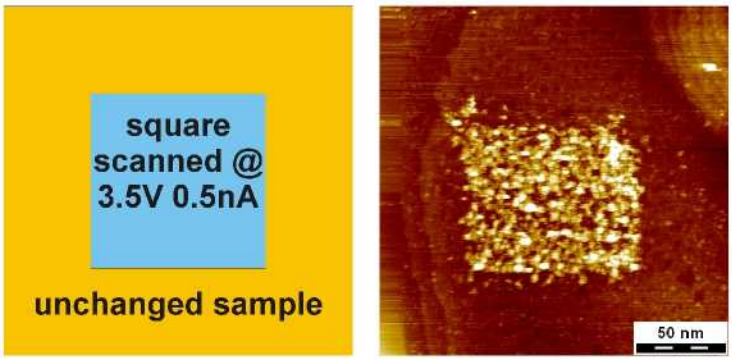

(a) writing scheme (b) 1.2 V, 85 pA

Figure 7.22: Topography scan of a disordered, mixed monolayer of octanethiol and ferrocenethiols, showing a central elevated structure due to high voltage/current scanning.

7.7 Spectroscopy

Scanning tunneling microscopy is not only sensitive to the topographical properties of a monolayer or molecule, but also to the electronic properties of the sample. Depending on the sample, a change in bias voltage causes the emergence of electronic features in the topography scan as observed in section 7.6.4. By using a controlled modulation of the bias voltage or the tip sample distance, a characterization of the electronic structure can be performed (See chapter 3.1).

7.7.1 Current-decay parameters

The electrical properties of ferrocene monolayers are studied by current/-distance spectroscopy (described in section 3.2). Both measurements are performed on extended patches of molecules inserted into undecanethiol. The spectra (figure 7.23) show the material dependent tunneling decay parameter of the monolayers. Both curves start with a low current branch on the left, for large tip sample distances, when the current is determined by the noise level of the preamplifier. Next, a sharp jump in the current occurs, when the tip is getting close to the monolayer surface. The slope in this branch is governed by the vacuum decay constant of

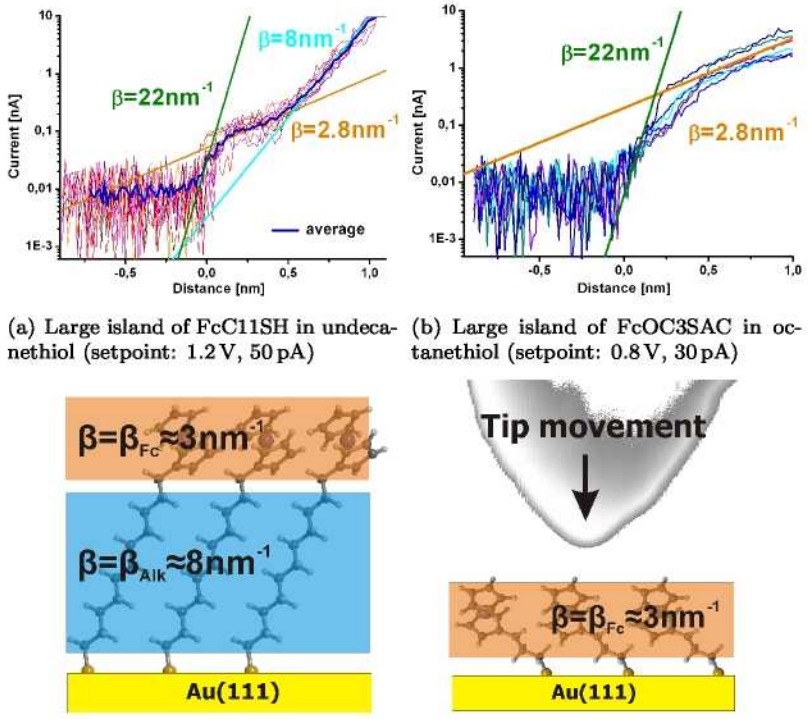

(a) Large island of FcC11SH in undecanethiol (setpoint: 1.2 V, 50 pA)

(b) Large island of FcOC3SAC in octanethiol (setpoint: 0.8 V, 30 pA)

(c) Schematic showing the electronic structure of a FcC11SH layer

(d) Schematic of a FcC3SH layer, showing only one decay regime

Figure 7.23: Current-distance spectroscopy of FcC11SH and FcOC3SAc layers at the given setpoints (a,b). The tip approaches to the sample from left to right and the current is recorded. The slopes of the current in the logarithmic plot reflect the current-decay parameter and are material dependent. In (c) and (d) the electronic structure of both monolayers is sketched schematically.

$\beta > 20\,\mathrm{nm}^{-1}$. Upon contact to the monolayer, the slope of the current changes, when the tip penetrates the thin film. Both layers show a β of $\sim 2.8\,\mathrm{nm}^{-1}$, attributed to the ferrocene moieties. The FcOC3SAc shows a small transition range around the contact point and only one decay constant for the complete layer. The FcC11SH shows sharp transition and after a distance of $\sim 0.4\,\mathrm{nm}$ the current slope rises again to a β of $\sim 8\,\mathrm{nm}^{-1}$, which resembles the current-decay parameter of alkanethiols. The characteristic of the FcC11SH monolayer is interpreted as a monolayer with two different regimes. Far away from the surface, the charge transfer is dominated by the ferrocene moiety ($\beta \sim 2.8\,\mathrm{nm}^{-1}$). After getting closer to the surface, the charge transfer is dominated by the alkane chain. The short chain ferrocenes FcC3SH form a layer with closely entangled ferrocene moieties and spacer chains as observed for FcC3SH in section 7.5.1. If a pure alkane dominated transport regime exists for FcOC3SH, it would be too close to the gold surface to be visible. The small transition region around the point of contact is probably caused by a small surface disorder or instability.

The current-decay constant is directly related to the apparent height of a tunneling barrier. The value for ferrocene of $\sim 2.8\,\mathrm{nm}^{-1}$ is very low, compared to the constants of $\sim 5\,\mathrm{nm}^{-1}$ observed for phenyl-moieties [50,188] or $\sim 8\,\mathrm{nm}^{-1}$ for alkanethiols [143]. Thus the measurements indicate the existence of available energy states close to the observed energy range, mediating the charge transfer by lowering the apparent tunneling barrier. Still, the dominant charge transfer mechanism is tunneling and no band conduction is observed for the ferrocenes in the given voltage range.

The measurement of a low apparent tunneling barrier height for ferrocenes can be interpreted and allows interesting conclusions for the electronic structure. No clear data for the HOMO-LUMO gap of chemisorbed ferrocenes on gold exists in literature, but a gap in the range of around 5 eV is found for plain ferrocenes from theoretical calculations [189] and spectroscopical measurements [190]. This value can be used as an approximation for the observed structure, although the energy states of a chemisorbed molecule may be significantly altered by the influence of the electrodes. From the assumption of reasonably spaced energy levels on the molecule and a low tunneling barrier height, the distribution of the energy levels can be deduced as follows: one energy level is significantly closer to the molecular fermi level, causing a low apparent tunneling barrier, resulting in a larger energy distance for the other one, being negligible for charge transport in a first approximation. Looking at the electrochemical characteristics of ferrocenes in solution, a

preferential oxidation of Fe^{2+} to Fe^{3+} at moderate potentials is found in solution, representing a donor behavior of the ferrocene moiety. Thus, the HOMO of the molecule is expected to be energetically closer to the Fermi energy than the LUMO and influences the current transport. These assumptions result in a first picture of the charge transfer properties of a ferrocene monolayer, observed by STM. On the tip side, the junction is weakly coupled to the electrode. The charge transfer is dominated by the HOMO of the molecule, being probably located within 1-3 eV to the Fermi level. On the substrate side, the coupling changes with the length of the alkane spacer which probably also moves the energy levels of the molecule itself. This assumptions for the electronic properties represent first approximations, based on the available data. A more elucidated model of the junction requires the statistical treatment of a large number of measurements in a more stable setup, supporting measurements with other methods and theoretical calculations.
The embedded FcC11SH molecules form a layered structure with a dedicated spacer layer and a surface layer of the ferrocene moieties. The observed thickness for the β=2.8 nm^{-1} range, ~0.4 nm is in close agreement with the size, expected for a single ferrocene moiety, indicating a layer structure with the ferrocenes exposed on the surface. The low current-decay constant attributed to the ferrocene end-group indicates a low apparent tunneling barrier. Based on which a rough model of the electronic properties of the junction can be drawn.

7.7.2 Voltage dependent behavior of the ferrocene moiety

The electronic behavior of embedded ferrocene molecules is also studied by direct current-voltage measurements and bias dependent imaging. For chemisorbed ferrocenes, as in the phase-separated islands of FcSSFc, described in section 7.6.2, CITS measurements allow a direct comparison of the electronic properties of ferrocenes and alkanethiols. In figure 7.24 the topography scan (a) shows an elevated island of ferrocenes surrounded by an alkanethiol matrix. The parallel current image for -1.5 V (b) shows a dark area, corresponding to a higher negative current, whereas the surrounding monolayer shows a clear contrast. Two characteristic areas for both materials are selected and their averaged curves are displayed (c). Ferrocenes and alkanethiols show typical tunneling characteristics with an increased current for the ferrocene molecules. Since

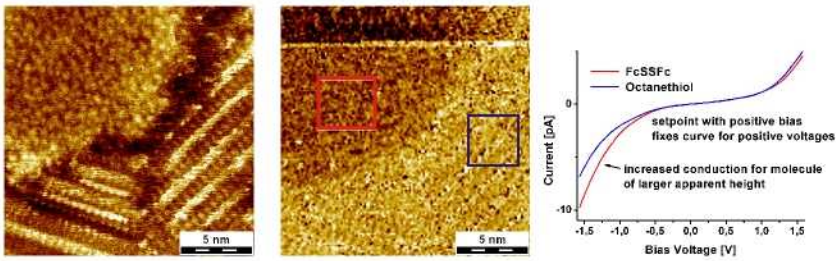

(a) Topography data of a CITS scan, showing a FcSSFc island surrounded by alkanethiols.

(b) CITS current image, showing an increased conductance in the area of the ferrocene island.

(c) I/V curves taken from the areas marked in (b), showing an increased conductance for the ferrocenes.

Figure 7.24: CITS measurements on FcSSFC phase-separated islands in octanethiol, showing plain tunneling characteristics for the given voltage range. The setpoint is 0.3 V/200 pA.

the ferrocenes appear already higher in the topography scan, this effect is already softened by the feedback loop during the CITS scan, responsible for a larger vacuum gap over the ferrocenes, than over the alkanethiols, indicating an enhanced conductivity of the ferrocenes. From the similar curve shape, tunneling can be assumed as the dominant charge transfer mechanism. This observation is in accordance to the almost three times better conduction of the ferrocene moiety, compared to the alkanethiols and tunneling as the dominant charge transfer mechanism, as observed by current-distance spectroscopy (See section 7.7.1).

To further examine the electronic characteristics of the ferrocene moiety, voltage dependent images of mixed ferrocene layers are scanned (figure 7.17). The height difference between ferrocene surface ribbons of FcC3SH and the surrounding octanethiol monolayer is measured in constant-current mode with variable bias voltages. As obvious from the selected images, the extension of the ferrocene moieties on the surface changes with the bias voltage. For lower bias voltages only slightly elevated features of blurry texture are visible, for higher negative biases bright, well-defined features appear. The resulting voltage dependent height difference, plotted into a diagram is shown in figure 7.25(e). The plot shows a strong exponential dependence of the height vs. bias, but without different regimes or jumps, which could be attributed to large changes in the structure or electronic properties. The bias dependence

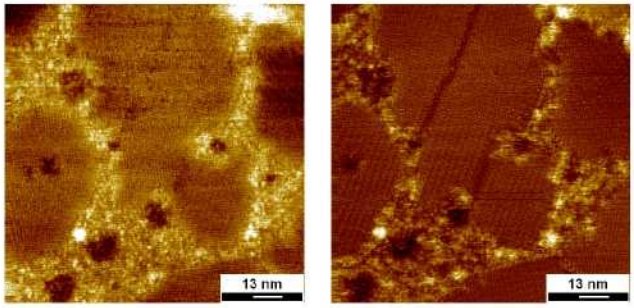

(a) -0.8 V (b) -1.1 V

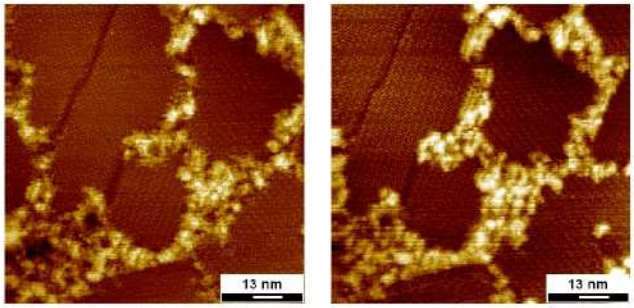

(c) -1.5 V (d) -1.8 V

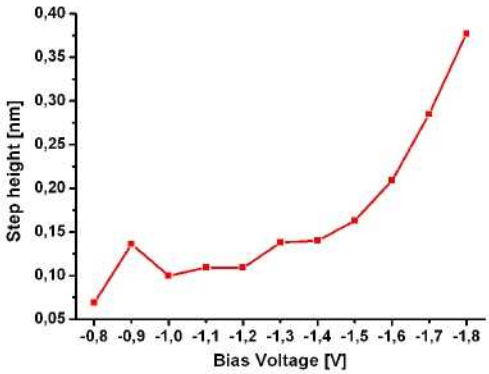

(e) Strong bias dependence of the height difference between ferrocene moiety and the surrounding alkanethiol monolayer.

Figure 7.25: STM scans of FcC3SH embedded in octanethiol, with a constant current of 0.05 nA. The ferrocene features on the surface change their appearance upon change of the bias voltage (a-d).

of the apparent height is predominantly caused by a voltage dependance of the molecular conduction. Thereby a voltage dependance in the exponential term of the tunneling current is indicated, as visible in the high bias approximation (voltage larger than barrier height) of the Simmons tunneling equations (table 2.2), also known as Fowler-Nordheim regime. Thus a low apparent tunneling barrier height is evident from the measurements and probable contributions of the molecular HOMO can be assumed as discussed in section 7.7.1. The effect is probably further enhanced by image charging [48], coulomb effects or small conformation changes of the ferrocenes, which prevents a quantitative fitting of the β-factor or barrier height.

Direct current-voltage measurements are also performed on ferrocene monolayers with alkane spacers (FcC11SH, FcC5SH and FcC3SH). However, they are not completely clear and suffer from large deviations and poor reproducibility. Still they share a few basic features as shown in figure 7.26. The measurements shown in reddish colors are taken on top of small islands or ribbons of the respective ferrocene derivatives and are compared to the current-voltage characteristic of the surrounding alkanethiol SAM, drawn in blueish colors. All ferrocene curves show a central plateau for lower bias voltages with a current comparable to the alkanethiols. In this central voltage range, no remarkable features can be observed and plain tunneling is assumed as the dominant charge transfer mechanism. For higher voltages the ferrocene curves differ from the alkanethiol curves and sometimes a sharp rise of the current occurs for negative biases as well as for positive biases. As shown for FcC11SH, in different measurements, the current can be more dominant for positive (a) or for negative (b) biases. The type of rise differs between the measurements and ranges from a linear type of increase (c), indicating an ohmic behavior, to a more frequently observed exponential rise (a, b, c). The onset voltage for the current rise is ill defined, ranging from no visible current jump, as observed in figure 7.24 down to a strong rise at around 0.7 V, as visible in figure 7.26(d). For higher voltages, above 2-2.5 V, unstable current-voltage curves are observed. These can be attributed to a structural rearrangement of the monolayer, caused by a reorientation of the ferrocene moieties, by movement or chemical changes of the monolayer or by effects of remaining physisorbed ferrocenes on the surface. In the worst case, even a decomposition of the ferrocenes might occur, as observed by Wolkow et al. [175] and Hla et al. [177].

The current increase, observed for higher voltages below the onset of instability is probably due to contributions of the HOMO, in accordance

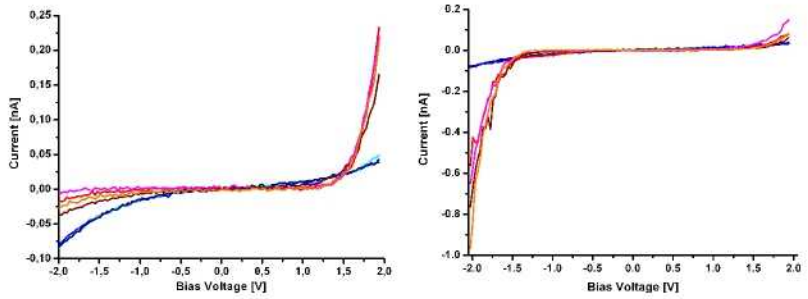

(a) FcC11SH 1.619 V, 25 pA, plateau and positive increase

(b) FcC11SH 1.907 V, 25 pA, plateau and negative increase

(c) FcC5SH -1.2 V, 50 pA, plateau, linear negative, positive increase

(d) FcC3SH 1.4 V, 100 pA, plateau, negative and positive increase

Figure 7.26: Current-voltage measurements for different ferrocenes embedded into alkanethiols as large surface patches. The diagrams compare the currents of the ferrocene (reddish) and the surrounding alkanethiol monolayer (blueish). The curves show different characteristics, depending on the molecule and the exact measurement conditions. For all combinations a pronounced change in the current is observed for higher biases.

to the assumptions made on the low current-decay constant (See section 7.7.1). Depending on the coupling to the electrode, the shape of the HOMO may vary dramatically, from localized states in the junction to an extended orbital, leading to different charge transfer-properties. The measurements in figure 7.26 show that electronic states of the ferrocene can be accessed by tunneling spectroscopy in a reasonable energy range. The detailed electronic structure of the junction is not known and can only be clarified by further measurements and theoretical calculations.
By spectroscopic measurements, the current-decay constant $\beta \approx 2.8$ of the ferrocene moiety is determined and a layered structure of the alkanethiol spacer with the ferrocene on top of the monolayer is verified for FcC11SH in undecanethiol. For short chain monolayers, a mixed layer with a homogenous decay constant, corresponding to ferrocene is observed. By direct current-voltage measurements and bias dependent height measurements, a well behaved charge transfer, indicating tunneling in the high voltage regime (See chapter 2), orbital mediated tunneling or hopping conduction, is observed. For current-voltage measurements on embedded ferrocene islands, an increase in current is observed for larger bias voltages. From the low current-decay constant of the junction and the molecular properties, an energetical position of the HOMO close to the Fermi level is assumed and the current increase observed for higher biases are attributed to charge transfer contributions of the HOMO.

7.8 Conclusion

For the first time, real space structural information of chemisorbed ferrocene monolayers is gathered. The wide range of molecules, deposition methods and combinations with alkanethiols are studied, resulting in a large number of new structures and discoveries, which need to be further investigated.
For ferrocenes without spacer-chain, only loosely ordered structures are found for single component and mixed monolayers. As for all ferrocenes, a strong tendency to physisorb additional ferrocenes on the first layer and to form bulky multilayer structures is observed. By extensive solution annealing or mixed monolayer preparation, stable monolayers with crystalline areas could be achieved. For single component monolayers of the homologous ferrocenes with mercaptoalkane spacers, the structural properties of the shorter chain FcC3SH could by determined by STM and

compared to x-ray studies. Based on these conclusions and additional measurements the structures of ferrocenes with longer spacer-chains are discussed as well.

The preparation of mixed monolayers is compared for different assembly routes, via a two step insertion process or a direct coadsorption process. For higher concentrations of the ferrocene species a clear difference is visible, showing crystalline alkanethiol domains with a ribbon-like decoration of the domain boundaries by the ferrocene end-group and a disordered mixed structure for the coadsorbed layer. The comparison proves, that the molecular exchange in solution takes place at the domain boundaries. For mixed layers, incorporating ferrocenes with a short or without a spacer-chain, a large interdiffusion and increased tendency for phase-separation is found. This effect can be attributed to the different interactions between the ferrocene moieties or between the alkane chains. For longer spacer-chains, the phase-separation is less pronounced. The structural properties of phase-separated islands for FcC11SH, FcOC11SAc and Fc(OC11SAc)2 are examined and a similar crystalline structure is found. In diluted mixed films, single, embedded ferrocene molecules could be identified. For lower coverage, mixed layers, an interesting hybrid structure of lying-down ferrocenes and alkanethiols is observed, resulting in long rows of ferrocene moieties separated by alkanethiols.

The resulting layers and structures are studied by spectroscopic methods. For embedded islands of FcC11SH in undecanethiol, i.e. a full-coverage alkanethiol monolayer with ferrocene moieties on top, a current-decay constant of β=2.8 nm^{-1} is observed for the ferrocene moiety and β=8 nm^{-1} for the intact alkanethiol monolayer below. For short spacer and no spacer ferrocenes, a similar β of around 3 nm^{-1} without alkanethiol contributions is found. Thereby a mixed layer with complete incorporation of the ferrocene moieties is indicated, dominating the charge transfer down to the surface. This assumption is further backed by the observation of such layers for pure FcC3SH. By measuring the bias dependent height difference of embedded ferrocenes in alkanethiols and by direct current-voltage spectroscopy, a well behaved tunneling conduction is observed for low biases. The strong bias dependence of the height difference and the low current-decay constant indicate a low apparent tunneling barrier height for the ferrocene moiety. For higher biases a change in the charge transfer properties is observed and attributed to contributions of the HOMO. For the first time the structural properties of ordered, chemisorbed ferrocene monolayers and mixed variations are

successfully studied by STM, down to the identification of single embedded molecules. Finally the electronic properties of the prepared structures, like the electronic decay constant β, are measured and a model for the electronic structure is suggested.

8 Carboxylic Acids on Cu(110)

Self-assembled monolayers of carboxylic acids on copper represent an alternative to the well known alkanethiol on gold system and enhance the understanding of self-assembly in general. One interesting aspect of the system is the substrate structure of the Cu(110) surface, as described in section 5.2. Its rectangular surface symmetry causes a strongly directed layer structure. This technique of modifying the layer structure by imposing structural or surface energy modulations offers a powerful options for the generation of bottom-up structures.

The assembly behavior, the electronic behavior and the structural properties of a self-assembled monolayer do not only depend on the molecules itself, but also on the substrate and the molecule-substrate interaction as well. The acidic carboxyl-group is capable of forming a strong bond to different metals like copper, nickel, palladium or platinum [191, 192]. Unlike the thiol-sulfur bond, the chemisorbed carboxyl moiety attaches the molecule with two points on the Cu(110) substrate, since the two oxygens of the carboxylate are bound to two substrate sites. Therefore free tilting and turning of the molecule to form a energetically optimal monolayer is restricted. Only one degree of freedom for tilting and one for rotation around the phenyl-carboxylate bond exists for benzoic acid, for terephthalic acid the top group is also rotatable. The adsorption sites on the Cu(110) surface closely match the distance between the two oxygen atoms of the carboxyl moiety and therefore represents an ideal surface for self-assembly [193]. As described in chapter 5.2, copper surfaces are very sensible to surface oxides and adsorbates and thus require ultra-high vacuum processing. In contrast to Au(111) surfaces, Cu(110) does not exhibit any surface reconstruction and therefore no vacancy island defects are formed. With respect to possible applications copper is preferred to gold, because the use of copper for interconnects is a standard process in semiconductor technology today. For theoretical calculations copper is preferred to gold, since the number of electrons in a

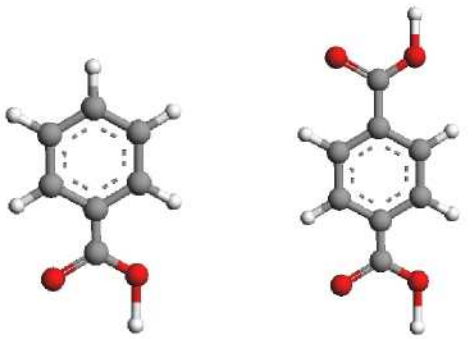

(a) Benzoic acid (b) Terephthalic acid

Figure 8.1: Ball and stick models of both carboxylic acids used for vapor deposition on Cu(110). The only difference between both molecules is the second carboxylic acid group of the terephthalic acid, offering the possibility for a free functional group on the monolayer surface.

copper atom is far lower than in a gold atom and thus the computational complexity is lower for any simulation of the chemisorbed molecule.

Benzoic acid and terephthalic acid (See figure 8.1) are chosen for the initial experiments. Benzoic acid consists of a benzene ring with an attached carboxyl moiety (See figure 8.1). The benzene ring as central moiety interacts with the neighboring molecules via $\pi - \pi$ interactions and is interesting for electrical studies, due to its delocalized π systems. Terephthalic acid contains an additional carboxyl-group at the para position and thereby provides a functional surface, which can chemisorb metal clusters or link to other molecules via the reactive top group. The Carboxyl moiety is attached to the benzene ring via σ-bonding and can be twisted. Twisting around the σ-bond and tilting in (001)-direction of the substrate represents the two angular degrees of freedom for monolayer assembly. Compared to the multiple degrees of freedom for an alkanethiol monolayer the formation of a benzoic acid monolayer is supposed to be less perfect, due to a limited adaptability and a stricter bonding, but the geometrical arrangement of a single molecule is better defined. Benzoic acid on Cu(110) is a thoroughly studied system and is used as a proof of concept for the in-vacuo processing of the monolayer inside the new experimental system described in chapter 4 and for

the establishment of the carboxylate copper system. Upon adsorption of benzoic acid from gas phase the carboxyl moiety is deprotonated and finally chemisorbed on the copper surface as studied and simulated in literature [194–197].

8.1 Experimental

To study the properties of chemisorbed monolayers on the sensible copper surface, a closed experimental system is needed. Therefore all experiments are done in the system, described in chapter 4, to ensure a vacuum environment during the whole preparation and measuring process. As substrate, copper single crystals prepared by sputtering and annealing, as specified in chapter 5.2 are used. Benzoic acid and terephthalic acid are bought from Sigma-Aldrich in 99% sublimation cleaned quality and used for vapor deposition as purchased. Before deposition, the molecule reservoir is exposed to freezing thawing cycles in vacuum, to ensure a pure vapor phase during the process. The molecules are deposited by vapor phase deposition in the designated chamber described in chapter 4. The substrate temperature during deposition is varied between room temperature and 500 K. The deposition pressure is adjusted between 1×10^{-6} mbar and 5×10^{-4} mbar, with the vapor pressure of the terephthalic acid being notably smaller than the pressure of the benzoic acid. The deposition times are varied between 1 min and 10 min for different experiments. The resulting thin films are imaged in constant current mode with the JSPM-4500S STM head. Special care is necessary for selection of the setpoint, since benzoate monolayers are easily disordered by scanning with high voltages or currents [198].

8.2 Benzoic acid

The structural properties of chemisorbed benzoates on Cu(110), depending on coverage and temperature were examined by Barlow and Raval with LEED, RAIRS and STM in great detail [191]. For increasing coverages, ordered domains of different structure, including lying down and standing-up molecules, evolve from disordered regions [191]. The formation of ordered monolayers is strongly dependent on the deposition temperature, since the deprotonation of the carboxylic acid moiety to the carboxylate ion is unlikely below 119 K and only short range domains of

benzoic acid are formed below this temperature. Below 200 K, multilayer formation occurs for higher coverages, since additional benzoic acid will not be desorbed. Above 580 K, the chemisorbed monolayer of benzoates becomes unstable [191]. For low coverages the benzoates lie flat on the surface and with increasing coverage ordered α-phase domains of lying benzoates are formed. The α-phase consists of four lying-down molecules per unit cell with an optional standing benzoate in the center. This structure is stabilized by the formation of benzoate-dimers by inclusion two surface adatoms per two benzoates [78]. Upon further deposition, a β-phase is formed [153,191], consisting of dimer rows and including more standing-up benzoates [78]. For saturation a c(8×2)surface order is observed as the dominant phase by LEED and STM [191,196]. For those layers both oxygen atoms of the carboxylate are chemisorbed on short bridge sites of the outermost copper layer, forming rows in [001] direction of the substrate with a packing density of one benzoate molecule per four outermost copper surface atoms (As shown in figure 8.5). The phenyl-rings of the molecules are arranged in the same plane as the carboxylate moiety, perpendicular to the substrate.

8.2.1 Thermal annealing

The deposition of benzoic acid on copper is optimized to achieve full-coverage, crystalline monolayers. For saturated layers, the influence of thermal annealing is studied. In figure 8.2(a) the structural evolution of a vapor-deposited thin film of benzoic acid on Cu(110) is shown. The surface is homogenously covered by a disordered molecular film with a few remaining spots indicating adlayers of physisorbed molecules or small copper islands covered by molecules, marked in blue. The surface already features a directed texture, caused by the symmetry of the Cu(110) surface, indicating a preferential orientation of the chemisorbed molecules. In the high resolution inset, the molecular structure is visible in detail, showing no visible short range order. Heating the surface to 500 K does not change the surface considerably, whereas heating to around 590 K results in an altered surface structure with obvious annealing effects. In the disordered phase, observed after deposition, domains of the ordered c(8×2)-phase are formed, with typical molecular rows as shown in figure 8.2(b). Upon further heating up to ~620 K, the surface continues to change. For strongly annealed surfaces, areas of lower molecular coverage are observed together with increased size of the ordered c(8×2) domains. Besides, a new, ordered, high-coverage phase is

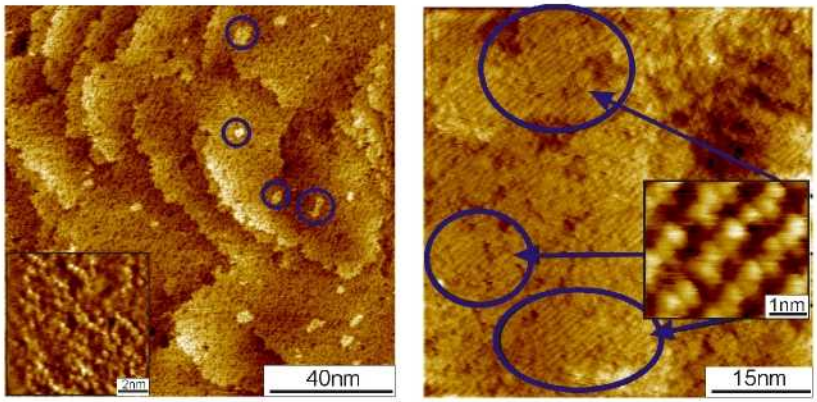

(a) disordered layer after deposition (b) annealed layer with c(8×2)structure

Figure 8.2: STM topography scans of benzoic acid on Cu(110), showing the effect of thermal annealing (90 min at 590 K) from a disordered surface to the c(8×2) ordered monolayer.

discovered, as described in section 8.2.2. Up to an annealing temperature of around 500 K, the surface is not changed. By annealing up to 590 K, the surface ordering is increased, forming the close packed c(8×2)-phase. Upon further annealing, thermal desorption takes place, together with further annealing effects.

8.2.2 New close-packed structure

For monolayers annealed at elevated temperatures above 620 K, as discussed in section 8.2, a new phase is observed. Large regions of the sample show the c(8×2)surface structure, shown in detail in figure 8.3(a). Within the c(8×2)domains a new structure evolved, with smaller feature size of the molecular rows and a different row direction with an angular change of about 35° (figure 8.3(b)). The unit cell of the new structure is determined as $\begin{pmatrix} 1 & 1 \\ -4 & 2 \end{pmatrix}$, with lattice vectors of $a_0 = 0.51$ nm and $b_0 = 1.23$ nm, as shown in figure 8.4. From the peak height of approximately 0.25 nm, a standing-up configuration of the molecules is assumed. With two molecules per unit cell, the new structure has a packing density of one molecule per three outermost surface copper atoms, resulting in

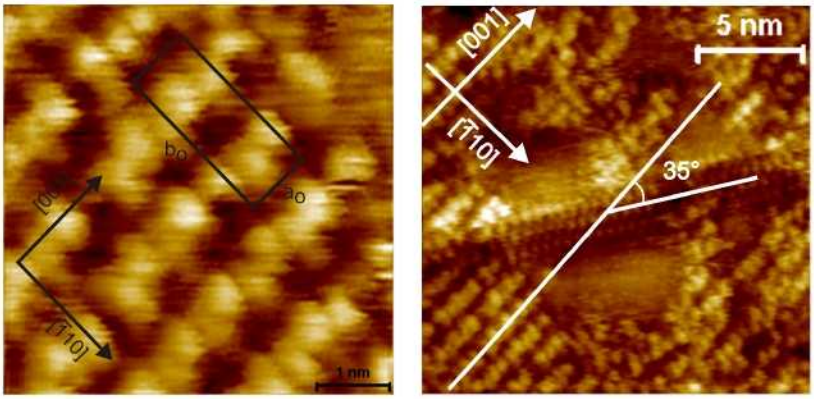

(a) c(8×2) structure (b) new structure

Figure 8.3: High-resolution scan of the c(8×2)-phase, showing the unit cell and surface vectors (a). The new structure with a different texture and changed row direction, surrounded by c(8×2)-domains.

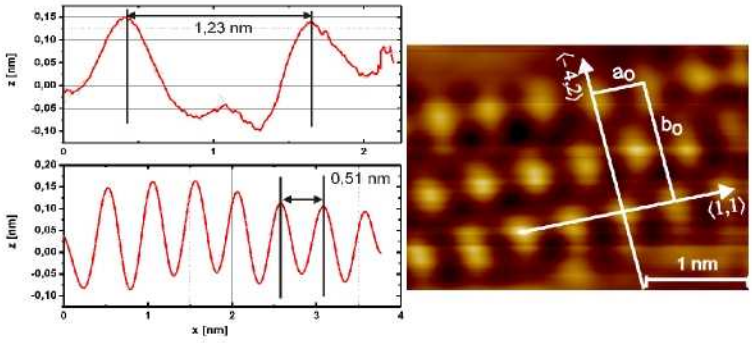

Figure 8.4: The new close packed structure of benzoates on Cu(110). The unit cell and substrate vectors are marked white. The profiles in the direction of the unit cell vectors show the dimensions of $a_0 = 0.51\,\text{nm}, b_0 = 1.23\,\text{nm}$.

a higher density as the c(8×2)-phase with one molecule per four surface atoms. The existence of higher coverage phases was already assumed by Frederick et al. in 1996 [78], but not observed before.

To assign an arrangement of the molecules on the copper lattice, the observed molecular structure is matched with the Cu(110) surface lattice. The intermolecular distances and the angular change, with respect to the c(8×2)-structure result in an unfavorable adsorption site for every second molecule of the unit cell. Half of the molecules are chemisorbed on the preferred copper atom rows of the outermost substrate layer, whereas the other half is placed exactly in between. To provide a stable adsorption site, a double row of adatoms is assumed, to stabilize the structure. By inclusion of the adatoms, the central molecules are bound atop the adatoms and form a stable complex. In figure 8.5, the molecular arrangement of the c(8×2)-phase and the new, adatom-stabilized structure is drawn. By looking at the height-profiles of the close-packed phase, a slight elevation is found for every second molecular row, supporting the adatom suggestion. A possible modification of benzoate monolayers by the incorporation of adatoms was already suggested by Frederick et al. [198] as an interpretation of observed structures. The existence of different benzoate-adatom complexes was already observed for low coverage phases by [78, 196, 199], further supporting the adatom idea.

To gain a deeper understanding and to cross-check the STM measurements, first-principles, DFT calculations of the suggested structure were started by N. Atodiresei at the IFF, Research Center Juelich. The suggested adatom stabilized structure and the equivalent structure without adatoms are modeled and allowed to relax. The suggested structure remains stable, whereas the structure without adatoms relaxes into a stable structure, to restore the optimal position above the copper atom rows, as shown in figure 8.6. The overall energies of the structures are calculated and show clear differences, resulting in the adatom stabilized structure being energetically favorable, compared to the other structures. For the adatom stabilized arrangement, STM images are simulated by the calculation of the LDOS of the sample and the generation of partial charge density plots. The isosurfaces of constant charge density, corresponding to a given energetic interval, represent the surface as imaged by the STM in constant-current mode. Figure 8.7(a) shows the surface arrangement of the molecules, stabilized with adatoms, (b-d) show different partial charge density images corresponding to the surface structure imaged for the given energies. For a sample bias voltage of -0.5 V (b), the orbitals

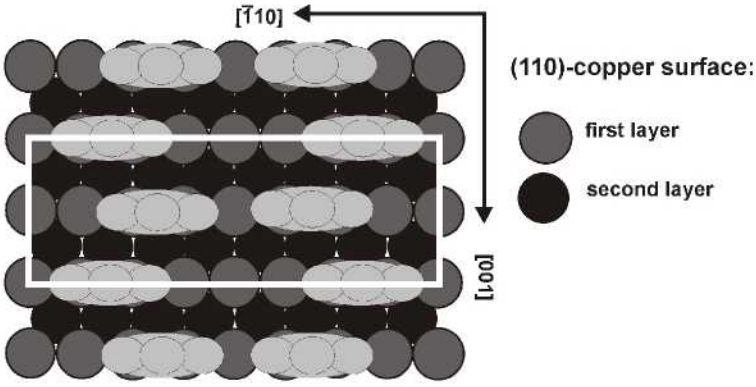

(a) c(8×2)-phase, with all molecules bound on top of two copper atoms in the outermost surface layer rows.

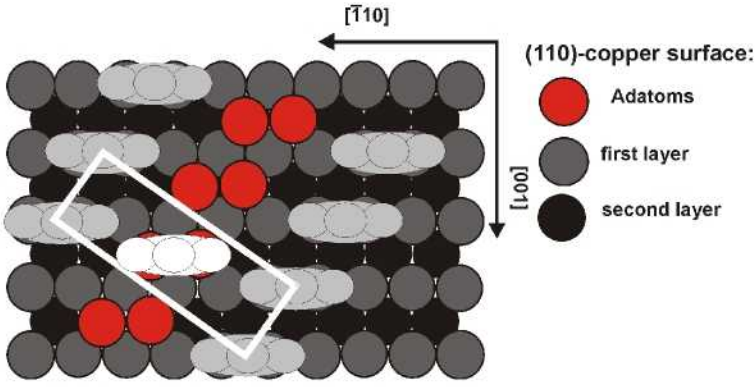

(b) New adatom stabilized phase. The central molecule cannot be placed atop a copper surface atom row. Thus a double row of copper adatoms is suggested to stabilize the structure.

Figure 8.5: Schematics of the adsorption structure of benzoates on Cu(110). Comparing the size of the unit cell, a clear difference in packing density is visible.

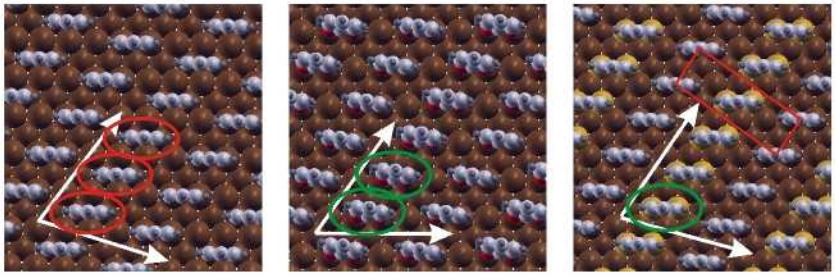

(a) initial phase (b) relaxed structure (c) adatom stabilized

Figure 8.6: Models of the close-packed structure without adatoms (a), relaxing into a stable structure (b), to optimize the bonding position of the central molecule. The molecule is marked red in the unfavored, respectively green at the preferred bonding site. (c) shows the stable, adatom stabilized structure, with the unit cell marked in red.

close to the molecule are plotted, showing the hybridized adatom states on the surface and π-type contributions on the sides of the phenyl rings. For a lower bias voltage of -0.78 V, corresponding to the setpoint of the STM images shown in figure 8.5, σ-type states are visible, elongating the molecular shape. Plotting the surface at a larger distance to the surface results in a bulky structure with a distinct difference between the higher adatom rows and the lower rows without adatoms. The adsorption behavior of benzoic acid on copper is studied by STM. The structural properties, described in literature are reproduced and the new system of carboxylates on Cu(110) including the substrate treatment and vapor deposition are established. Upon closer inspection, an new high-coverage phase is discovered and a surface molecular arrangement, stabilized by adatoms, is suggested. By DFT, the new structure is further supported and STM pictures can be simulated.

8.3 Terephthalic acid

The adsorption of terephthalic acid on copper is studied by spectroscopic methods [192,200] and lying-down phases on Cu(100) are investigated by STM [201]. The molecular structure of the terephthalic acid is shown in figure 8.1. The molecule is identical to benzoic acid with an additional

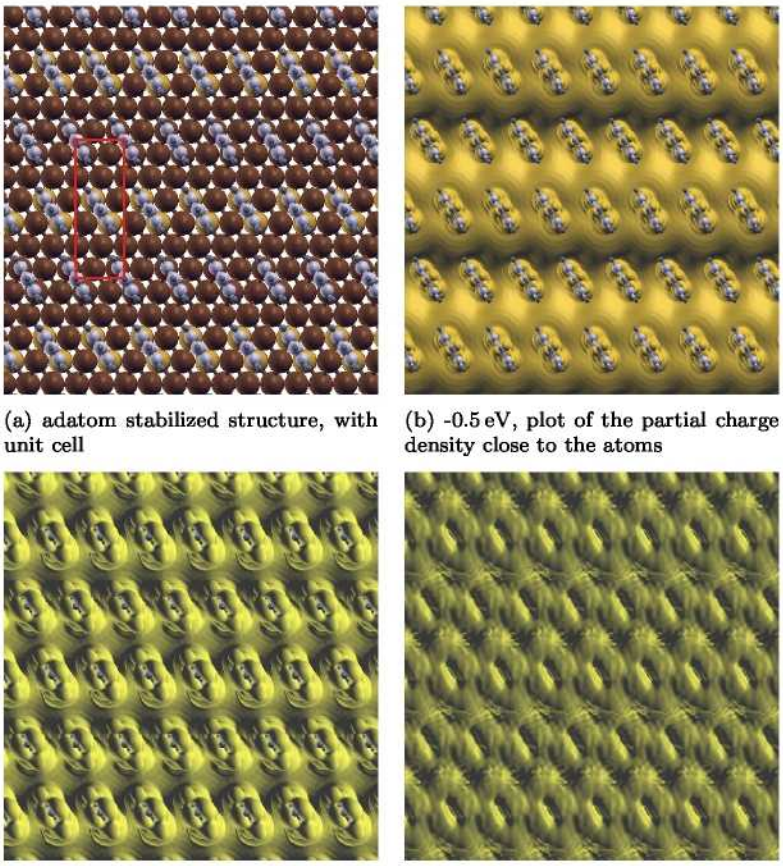

(a) adatom stabilized structure, with unit cell

(b) -0.5 eV, plot of the partial charge density close to the atoms

(c) -0.78 eV, plot of the partial charge density close to the atoms

(d) -0.78 eV, plot of the partial charge density far away in the vacuum

Figure 8.7: Simulated constant-current STM images of the adatom stabilized structure of benzoates on Cu(110). The partial charge density isosurfaces are drawn for different tunneling energies.

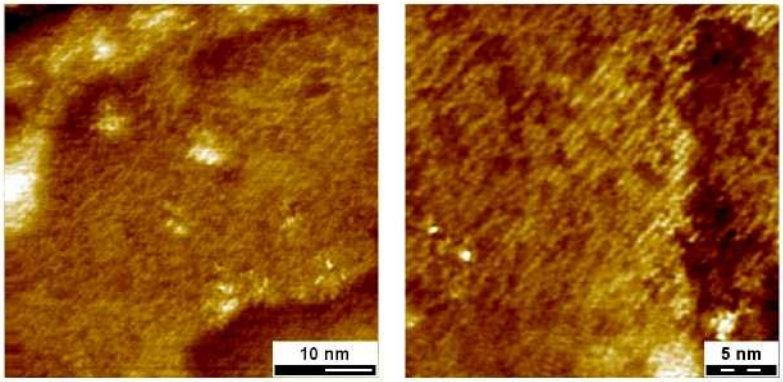

(a) as deposited, the brighter areas indicate excess molecules.

(b) annealed structure showing a strong orientation of the molecular backbones.

Figure 8.8: STM scans of terephthalic acid on Cu(110). After deposition the layer is disordered with a directed surface texture, after annealing for 90 min at 775 K, ordered molecular structures appear.

carboxylic acid moiety in the para position of the phenyl ring. For surface deposition, different molecular arrangements are possible. The terephthalic acid can be deprotonated and bind on one side, exposing free carboxylic acid groups on the surface or it can react with both carboxylic acid moieties, binding the molecules flat on the surface. By RAIRS and LEED measurements for high coverage phases, Martin et al. have observed the chemisorption in upright position, exposing the second carboxylic acid moiety as functional unit on the surface. By LEED a p(10×2)-structure was found for the molecular arrangement on the surface [200].

8.3.1 First topography scans

Upon deposition of terephthalic acid on the copper substrate, disordered layers with a directed texture, caused by the substrate symmetry are formed as shown in figure 8.8. On the surface, the copper substrate steps are clearly visible and the surface exhibits a few brighter spots, probably indicating excess molecules, physisorbed on the substrate. Thereby, full monolayer coverage can be deduced. After annealing for 90 min at

775 K, ordered structures appear on the sample. Compared to the annealing behavior of the benzoate layers, described before, the terephthalate monolayers require slightly elevated annealing temperatures. The STM scans shown in figure 8.8 represent the first successful STM scans of terephthalic acid on Cu(110). The surface properties and deposition conditions are very similar to those of the benzoate monolayers and seem to confirm the measurements of Martin et al. [200], resulting in standing up monocarboxylates on the surface.

8.4 Conclusion

The new carboxylate on copper system is established, including processing of the sensible copper substrates and vapor deposition procedures. Monolayers of benzoic acid and terephthalic acid are successfully deposited on Cu(110) surfaces and molecular resolution by STM is achieved. The samples can be annealed at elevated temperatures, to increase the order of the molecules. For benzoates on copper, the literature results for a close packed structure are reproduced and a new, adatom stabilized molecular arrangement is suggested. The new molecular structure is further tested and verified by DFT calculations, supporting the initial assumptions. Thereby, theoretical support for the interpretation of structural and electronic properties is achieved, being one of the major reasons for the choice of copper substrates. For the chemisorption of terephthalic acid on copper, the first STM scans are measured, showing a close-packed, ordered surface with exposed functional groups.

9 Conclusion

This thesis explored the structural and electronic properties of building blocks for molecular electronics. In particular, the structural properties of different self-assembled systems and the charge transfer properties of the ferrocene moiety were studied. First, the preparation of Au(111) thin films and Cu(110) single crystal substrates was described. To establish vapor deposition of molecules and to enable single crystal handling, a new experimental UHV system was constructed and described in the second chapter. In the following the alkanethiol on gold system was further studied, serving as an archetypical system and as a matrix for the investigation of different ferrocene derivatives, chemisorbed on gold. For the ferrocenes, a large number of structures were discovered and a basic understanding of the formation of monolayers and small assemblies was achieved. For the first time, a current-decay constant was assigned and electronic measurements on well-defined structures performed. Finally the carboxylate/copper system was established, literature results reproduced, and a new phase discovered and interpreted with the support of DFT calculations.

9.1 Substrates

High-quality thin films of Au(111) on mica have been manufactured by a two step electron beam deposition procedure in vacuum. The substrates exhibit a low surface roughness and show large crystalline terraces suitable for monolayer deposition. The substrates have been fully characterized and yield high-quality surfaces for STM studies.

To provide clean and flat Cu(110) surfaces for the deposition of carboxylate monolayers, a crystal preparation procedure was established. Before monolayer deposition, the sample is cleaned by successive cycles of argon sputtering and thermal annealing. The oxygen adsorption behavior on the crystal surface was studied by STM and XPS and a reasonable process window in UHV identified. After the pretreatment procedure, the surface shows clean terraces of reasonable size.

9.2 Construction of a new experimental UHV system

A new UHV system has been constructed and features sputtering, heating, deposition and measurement facilities. The recipient consists of a detached chamber for vapor phase deposition of organic molecules, a load lock chamber, a storage chamber and a measurement chamber. In addition, facilities for tip heating and tip sputtering are provided. The system incorporates a JEOL measurement head with cryostat and reaches a base pressure of 5×10^{-11} mbar in the measurement chamber. In the new system, copper single crystals were successfully prepared and measured and high-resolution images of ferrocene monolayers obtained.

9.3 Self-assembled monolayers of alkanethiols

Monolayers of alkanethiols were deposited from solution onto (111)-oriented gold thin film substrates. The resulting layers were studied by UHV-STM and characterized with molecular resolution. From topographical measurements a new c(4×2) unit cell with four distinguable molecules was identified and named ζ-phase (B.L̃üssem et al. [116]). Looking at the assembly and annealing process, a second new phase close to desorption was identified, pointing the high mobility of the alkanethiols on the gold surface and a possible variation in the bonding positions. By studying the domain boundaries of alkanethiol monolayers, coexisting domains of hcp and fcc bound molecules were found indicating a negligible difference in binding energy between the two bonding sites. Spectroscopic methods were used to probe the electronic structure of the distinguable molecules inside a unit cell, which shows only slight differences for each adsorption site, and the electronic decay constant of the monolayer was determined to serve as a spectroscopic reference for measurements on ferrocenes. Thus a better understanding of the monolayer properties, especially at the interface, has been achieved.

9.4 Structural and electrical properties of ferrocenes

For the first time, real space structural and spectroscopical information has been gathered on chemisorbed monolayers incorporating ferrocene moieties. Since hardly any information is available in the literature, a large number of new structures and properties were discovered in this thesis.

Self-assembled monolayers of mercaptoalkyl ferrocenes were successfully prepared and studied for the first time by STM. For mercaptopropylferrocene, a detailed molecular structure was found and compared to x-ray measurements. Based on these observations and additional measurements, the structures of ferrocenes with longer spacer chains were also discussed. For ferrocenes without spacer chains, only loosely ordered, bulky structures were observed for single component and mixed monolayers. All the ferrocenes studied showed a strong tendency to physisorb additional ferrocenes on the first layer and form bulky multilayer structures, which were reduced by strong solution annealing.

The assembly routes via a two-step insertion process or a direct coadsorption process were compared for the preparation of mixed monolayers. Clear differences were visible for higher concentrations of the ferrocene species. The surface of the insertion-processed monolayers showed ordered alkanethiol domains with a ribbon-like decoration of the domain boundaries by the ferrocene end-groups. The surface of the coadsorbed layer showed a disordered mixed structure. For mixed layers incorporating ferrocenes, an increased tendency towards phase separation was observed for ferrocenes with shorter spacer-chains. In mixed monolayers of different ferrocene derivatives and alkanethiols, a large variety of new, mixed structures was observed and described, ranging from single embedded molecules through various island structures up to a hybrid phase with interesting structural properties.

The electronic properties of the ferrocene moiety were studied by current-distance spectroscopy on embedded islands of FcC11SH in undecanethiol, i.e. a full-coverage alkanethiol layer with ferrocene end-groups. A current-decay constant of β=2.8 nm^{-1} was determined for the ferrocene group and a β=8 nm^{-1} for the intact alkanethiol spacer layer below. A similar β around 2.8 nm^{-1} without alkanethiol contributions is found for ferrocenes with short spacers and no spacer. By measuring the bias-dependent height difference of embedded ferrocenes in alkanethiols and

by direct current-voltage spectroscopy, a well-behaved tunneling conduction was observed for low biases. A strong bias dependence of the height difference and the low current-decay constant indicates a very low apparent tunneling barrier height for the ferrocene moiety. For higher biases a change in the charge transfer behavior was observed and attributed to a beginning contribution by the ferrocene HOMO.

9.5 Self-assembled monolayers of carboxylates on copper

Monolayers of benzoic acid and terephthalic acid were successfully deposited on Cu(110) surfaces, and molecular resolution by STM was achieved. After deposition, the samples were annealed at elevated temperatures, to successfully increase the order of the molecules. An extra molecule-substrate system was thus established for studies, including processing of the delicate copper substrates and vapor deposition procedures. The literature results for a close packed structure [196] were reproduced for benzoates on copper and a new, adatom-stabilized molecular arrangement discovered. The new molecular structure was further tested and verified by DFT calculations, which support the assumption of copper adatoms incorporated into the structural arrangement. Theoretical support for the interpretation of structural and electronic properties was thus achieved, which was one of the reasons for the choice of copper substrates. The first STM scans were performed, for the chemisorption of terephthalic acid on copper, showing a close-packed, ordered surface with exposed functional groups.

9.6 Perspectives

The different systems studied in this work represent potential building blocks for future molecular devices and a wide range of possible applications. Aromatic systems such as the phenyl-rings of benzoic and terephthalic acid have a great potential, for conducting or semiconducting structures in the form of monolayers or larger molecular assemblies. Alkanethiols represent an ideal spacer and insulator material. In the form of monolayers consisting of alkanethiols with a functional endgroup, the functional group is well separated from the substrate and interesting properties may arise, such as a switchable surface that can

change between wetting and de-wetting behavior [202]. For larger molecular systems and assemblies, alkanes can be used as adjustable spacers, separating different functional parts of a molecule electronic and physically.

Mixed layers and hybrid structures offer the chance to combine different molecular properties in a single layer. Layers of shorter and longer molecules or different functional groups inside the layer and on the surface can be used to create larger-scale assemblies with unique properties. Even selected molecular ratios may be achieved by electrochemical methods or smart combinations. Functional surface groups such as ferrocenes or carboxylic acids offer opportunities for use in surface chemistry, as catalysts or for the selective adsorption of various molecules, clusters or other building blocks.

Molecules with a potential for storing and manipulating charge, such as ferrocenes, may form the functional backbone of molecular information processing and their comprehension represents the first steps towards possible applications. The redox properties of plain ferrocenes may be used, for instance, as simple molecular memories [164]. The true potential of electro-active molecules lies in the combination of donor moieties like ferrocene and acceptor moieties to form larger charge transfer complexes. The exact properties of such a network can be fine-tuned by using different bridging molecules or adjusting the molecular energy levels by controlled substitutions and additions to achieve the desired electrical behavior.

The creation of advanced functional units for information processing by a combination of charge transfer complexes, relying on the power of chemical methods for the fabrication of the smallest structures, represents the long-term aim of true molecular electronics.

Nomenclature

A/D	*a*nalog/ *d*igital
AFM	*a*tomic *f*orce *m*icroscope
cAFM	*c*onductive*a*tomic *f*orce *m*icroscope
CITS	*c*urrent *i*maging *t*unneling *s*pectroscopy
CMOS	*c*omplementary *m*etal *o*xide *s*emiconductor
FFT	*f*ast *f*ourier *t*ransformation
GIXD	*g*razing-*i*ncidence *x*-ray *d*iffraction
HOMO	*h*ighest*o*ccupied *m*olecular *o*rbital
HOPG	*h*ighly*o*riented *p*yrolytic *g*raphite
I/S	current-distance spectroscopy
I/V	current-voltage spectroscopy
IC	*i*ntegrated *c*ircuit
IETS	*i*nelastic *e*lectron *t*unneling *s*pectroscopy
LB	*l*angmuir *b*lodgett
LDOS	*l*ocal *d*ensity *o*f *s*tates
LUMO	*l*owest*u*noccupied *m*olecular *o*rbital
NDR	*n*egative *d*ifferential *r*esistance
OP	*op*erational amplifier
QCM	*q*uartz *c*rystal *m*icrobalance
RMS	*r*oot *m*ean *s*quare
SAM	*s*elf *a*ssembled *m*onolayer
SEM	*s*canning *e*lectron *m*icroscopy
SPM	*s*canning *p*robe *m*icroscope
STM	*s*canning *t*unneling *m*icroscope
STS	*s*canning *t*unneling *s*pectroscopy
THF	*t*etra-*h*ydro *f*uran
TMP	*t*urbo *m*olecular *p*ump
UHV	*u*ltra-*h*igh *v*accum
XPS	*x*ray-*p*hoto-emission *s*pectroscopy
XSW	*x*ray-*s*tanding *w*ave

Bibliography

[1] J. von Neumann, . First Draft of a Report on EDVAC. Technical report University of Pennsylvania june 1945.

[2] J. Bardeen, W.H. Brattain, The Transistor, A Semi-Conductor Triode. *Physical Review* **74**, 230–231 (1948).

[3] C.K. Chiang, C.R. Finche Jr., Y.W. Park, A.J. Heeger, H. Shirakawa, E.J. Louis, S.C. Gau, A.G. MacDiarmid, Electrical Conductivity in Doped Polyacetylene. *Physical Review Letters* **39**, 1098–1101 (1977).

[4] ed. by R. Waser *Nanoelectronics and Information Technology – Advanced Electronic Materials and Novel Devices.* Wiley-VCH Verlag GmbH, Weinheim, 2003.

[5] M. Ruben, J Rojo, F.J. Romero-Salguero, L.H. Uppadine, J.-M. Lehn, Grid-Type Metal Ion Architectures: Functional Metallosupramolecular Arrays. *Angewandte Chemie* **43**, 3644–3662 (2004).

[6] M.D. Watson, A. Fechtenkoetter, K. Muellen, Big is beautiful-"Aromaticity" Revisited from the Viewpoint of Macromolecular and Supramolecular Benzene Chemistry. *Chemical Review* **101**, 1267–1300 (2001).

[7] J.V. Barth, G. Constantini, K. Kern, Engineering Atomic and Molecular Nanostructures at Surfaces. *Nature* **437**, 671–679 (2005).

[8] A. Aviram, M.A. Ratner, Molecular Rectifiers. *Chemical Physics Letters* **29**, 277–283 (1974).

[9] M.A. Reed, C. Zhou, C.J. Muller, T.P. Burgin, J.M. Tour, Conductance of a Molecular Junction. *Science* **278**, 252–254 (1997).

[10] A. Szuchmacher Blum, J.G. Kushmerick, D.P. Long, C.H. Patterson, J.C. Yang, J.C. Henderson, Y. Yao, J.M. Tour, S. Sashidhar, B.R. Ratna, Molecularly Inherent

Voltage-Controlled Conductance Switching. *Nature Materials* **4**, 167–172 (2005).

[11] C.P. Collier, E.W. Wong, M. Belohradsky, F.M. Raymo, J.F. Stoddart, P.J. Kuekes, R.S. Williams, J.R. Heath, Electronically Configurable Molecular-Based Logic Gates. *Science* **285**, 391–394 (1999).

[12] R.F. Service, Next-Generation Technology Hits an Early Midlife Crisis. *Science* **302**, 556–559 (2003).

[13] C.A. Richter, D.R. Steward, D.A.A. Ohlberg, R.S. Williams, Electrical Characterization of Al/AlO_x/Molecule/Ti/Al Devices. *Applied Physics A* **80**, 1355–1362 (2005).

[14] B. Lüssem, M. Alba, S. Karthäuser, S. Kronholz, M. Weides, R. Waser, Resistive Switching of Devices Based on Thin Films of Rose Bengal: a Molecular Effect? *Journal of Applied Physics* **100**, 094504 (2006).

[15] I. Langmuir, The Constitution and Fundamental Properties of Solids and Liquids. 11. Liquids. *Journal of the American Chemical Society* **39**, 1848–1906. (1917).

[16] K.B. Blodgett, Films Built by Depositing Successive Monomolecular Layers on a Solid Surface. *Journal of the American Chemical Society* **57**, 1007 (1935).

[17] K.B. Blodgett, I. Langmuir, Built-Up Films of Barium Stearate and Their Optical Properties. *Physical Review* **51**, 964 (1937).

[18] H. Emmons, The Mechanism of Drop Condensation. *Transactions of the American Institute of Chemical Engineers* **35**, 0109–0125 (1939).

[19] W.C. Bigelow, D.L. Pickett, W.A. Zisman, Oleophobic Monolayers .1. Films Adsorbed from Solution in Non-Polar Liquids. *Journal of Colloid Science* **1**, 513–538 (1946).

[20] E.E. Polymeropoulos, J. Sagiv, Electrical Conduction through Adsorbed Monolayers. *Journal of Chemical Physics* **69**, 1836–1847 (1978).

[21] Unknown, Monolayer Films that Assemble Themselves. *New Scientist* **98**, 20 (1983).

[22] A. Ulman, Formation and Structure of Self-Assembled Monolayers. *Chemical Review* **96**, 1533 (1996).

[23] F. Schreiber, Structure and Growth of Self-Assembling Monolayers. *Progress in Surface Science* **65**, 151–256 (2000).

[24] F. Schreiber, Self-Assembled Monolayers: from 'Simple' Model Systems to Biofunctionalized Interfaces. *Journal of Physics.: Condensed Matter* **16**, R881–R900 (2004).

[25] J.C. Love und D.B. Wolfe und R. Haasch u.a., Formation and Structure of Self-Assembled Monolayers of Alkanethioles on Palladium. *Journal of the American Chemical Society* **125**, 2597 (2003).

[26] A.F. Carley, P.R. Davies, R.V. Jones, K.R. Harikumar, M.W. Roberts, An STM and XPS Study of the Chemisorbtion of Methyl Mercaptan at a Cu(110) Surface. *Surface Science* **490**, 585–591 (2001).

[27] K. Heister, M. Zharnikov, M. Grunze, L.S.O. Johansson, Adsorption of Alkanethiols and Biphenylthiols on Au and Ag Substrates: A High-Resolution X-ray Photoelectron Spectroscopy Study. *Journal of Physical Chemistry B* **105**, 4058–4061 (2001).

[28] M.H. Schoenfisch, A.M. Ross, J.E. Pemberton, Electrochemical Cleaning of Surface-Confined Carbon Contamination in Self-Assembled Monolayers on Polycrystalline Ag and Au. *Langmuir* **16**, 2907–2914 (2000).

[29] K. Adlkofer, A. Shaporenko, M. Zharnikov, M. Grunze, A. Ulman, M. Tanaka, Chemical Engineering of Gallium Arsenide Surfaces with 4-Methyl-4-mercaptobiphenyl and 4-Hydroxy-4-mercaptobiphenyl Monolayers. *J. Phys. Chem. B* **107**, 11737–11741 (2003).

[30] K. Slowinski, H.K.Y. Fong, M. Majda, Mercury-Mercury Tunneling Junctions. 1. Electron Tunneling Across Symmetric and Asymmetric Alkanethiolate Bilayers. *Journal of the American Chemical Society* **121**, 7257–7261 (1999).

[31] W. Geyer, V. Stadler, W. Eck, M. Zharnikov, A. Gölzhäuser, M. Grunze, Electron-Induced Crosslinking of Aromatic Self-Assembled Monolayers: Negative Resists for Nanolithography. *Applied Physics Letters* **75**, 2401–2403 (1999).

[32] A.M. Rawlett, T.J. Hopson, I. Amlani, R. Zhang, J. Tresek, L.A. Nagahara, R.K. Tsui, A Molecular Electronics Toolbox. *Nanotechnology* **14**, 377–384 (2003).

[33] R. Liu, S.-H. Ke, H.U. Barangerand W. Yang, Organometallic Spintronics Dicobaltocene Switch. *Nano Letters* **5**, 1959 –1962 (2005).

[34] D.M. Adams, L. Brus, C.E.D. Chidsey, S. Creager, C. Creutz, C.R. Kagan, P.V. Kamat, X.M. Lieberman, O.S. Lindsay, R.A. Marcus, R.M. Metzger, M.E. Michel-Beyerle, J.R. Miller, M.D. Newton, D.R. Rolison, O. Sankey, K.S. Schanze, J. Yardley, X. Zhu, Charge Transfer on the Nanoscale: Current Status. *Journal of Physical Chemistry B* **107**, 6668–6697 (2003).

[35] A. Salomon, C. Cahen, S. Lindsay, J. Tomfohr, V.B. Engelkes, C.D. Frisbee, Comparison of Electronic Transport Measurements on Organic Molecules. *Advanced Materials* **15**, 1881–1890 (2003).

[36] L.A. Bumm, J.J. Arnold, T.D. Dunbar, D.L. Allara, P.S. Weiss, Electron Transfer through Organic Molecules. *Journal of Physical Chemistry B* **103**, 8122–8127 (1999).

[37] V.V. Zhirkov, R.K. Cavin, Molecular Electronics Chemistry of Molecules or Physics of Contacts? *Nature Materials* **5**, 11–12 jan 2006.

[38] J.G. Kushmerick, D.B. Holt, J.C. Yang, J. Naciri, M.H. Moore, R. Shashidhar, Metal-Molecule Contacts and Charge Transport across Monomolecular Layers: Measurement and Theory. *Physical Review Letters* **89**, 086802–1–086802–4 (2002).

[39] L.T. Cai, H. Skulason, J.G. Kushmerick, S.K. Pollack, J. Naciri, R. Shashidhar, D.L. Allara, T.E. Mallouk, T.S. Mayer, Nanowire-Based Molecular Monolayer Junctions: Synthesis, Assembly, and Electrical Characterization. *Journal of Physical Chemistry B* **108**, 2827–2832 (2004).

[40] W. Wang, T. Lee, M.A. Reed, Mechanism of Electron Conduction in Self-Assembled Alkanethiol Monolayer Devices. *Physical Review B* **68**, 035416 (2003).

[41] X.D. Cui, A. Primak, X. Zarate, J. Tomfohr, O.F. Sankey, A.L. Moore, T.A. Moore, D. Gust, G. Harris, S.M. Lindsay, Reproducible Measurement of Single-Molecule Conductivity. *Science* **294**, 571–574 (2001).

[42] Xing Lu, K. W. Hipps, Scanning Tunneling Microscopy of Metal Phthalocyanines: d6 and d8 Cases. *Journal of Physical Chemistry B* **101**, 5391–5396 (1997).

[43] D.I. Gittins; D. Bethell; D.J. Schiffrin; R.J. Nichols, A Nanometer-Scale Electronic Switch Consisting of a Metal Cluster and Redox-Adressable Groups. *Nature* **408**, 67–69 (2000).

[44] J. Park, A.N. Pasupathy, J.I. Goldsmith, C. Chang, Y. Yaish, J.R. Petta, M. Rinkoski, J.P. Sethna, H.D. Abruna, P.L. McEuen, D.C. Ralph, Coulomb Blockade and the Kondo Effect in Single-Atom Transistors. *Nature* **417**, 722–725 (2002).

[45] G.K. Ramachandran, T.J. Hopson, A.M. Rawlett, L.A. Nagahara, A. Primak, S.M. Lindsay, A Bond-Fluctuation Mechanism for Stochastic Switching in Wired Molecules. *Science* **300**, 1413–1416 (2003).

[46] Z. Huang, B. Xu, Y. Chen, M. Di Ventra, N. Tao, Measurement of Current-Induced Local Heating in a Single Molecule Junction. *Nano Letters* (2006).

[47] J.G. Simmons, Generalized Formula for the Electric Tunnel Effect between Similar Electrodes Separated by a Thin Insulating Film. *Journal of Applied Physics* **34**, 1793–1803 (1963).

[48] J.G. Simmons, Electric Tunnel Effect between Dissimilar Electrodes Separated by a Thin Insulating Film. *J. Appl. Phys.* **34**, 2581 (1963).

[49] J.K. Tomfohr, *Electron Tunneling Transport Theory for Molecules.* Ph.D. thesis, Arizona State University, 2002.

[50] B. Lüssem, *Molecular Electronic Building Blocks Based on Self-Assembled Monolayers.* Ph.D. thesis, RWTH-Aachen, 2006.

[51] G. Binning, H. Rohrer, Scanning Tunneling Microscopy. *Helvetica Physica Acta* **55**, 726–735 (1982).

[52] G. Binning, H. Rohrer, Scanning Tunneling Microscopy - from Birth to Adolescence. *Reviews of modern physics* **59**, 615–625 July 1987. lecture from dec 1986 on the occasion of the presentation of the Nobel Prize in Physics.

[53] G. Binning, C. F. Quate, C. Gerber, Atomic Force Microscope. *Physical Review Letters* **56**, 930–933 (1986).

[54] ed. by D. Bonnell *Scanning Probe Microscopy and Spectroscopy.* Wiley-VCH, 2001.

[55] Colton, Engel, Frommer, Gaub, Gewirth, Guckenberger, Heckl, Parkinson, Rabe, *Procedures in Scanning Probe Microscopy.* John Wiley & Sons, 1998.

[56] ed. by U. Hartmann. *Fortgeschrittenenpraktikum Rastersondenmikroskopie*, . Institute of Experimental Physics, University of Saarbruecken (2003).

[57] D.M. Eigler, E.K. Schweizer, Positioning Single Atoms with a Scanning Tunneling Microscope. *Nature* **344**, 524–526 (1990).

[58] Y. Shirai, A.J. Osgood, Y. Zhao, K.F. Kelly, J.M. Tour, Directional Control in Thermally Driven Single-Molecule Nanocars. *Nano Letters* **5**, 2330–2334 (2005).

[59] ed. by P. Samorì *Scanning Probe Microscopies Beyound Imaging.* Wiley-VCH, 2006.

[60] J. Tersoff, D.R. Hamann, Theory of the Scanning Tunneling Microscope. *Physical Review B* **31**, 805–813 (1985).

[61] B. Lüssem, L. Müller-Meskamp, S. Karthäuser, M. Homberger, U. Simon, R. Waser, Electrical and Structural Characterisation of Biphenylethanethiol SAMs. *Journal of Physical Chemistry C* **111**, 6392–6397 (2007).

[62] R.M. Feenstra, J.A. Stroscio, A.P. Fein, Tunneling Spectroscopy of the Si(111) 2x1 Surface. *Surface Science* **181**, 295–306 (1987).

[63] V.A. Ukraintsev, Data Evaluation Technique for Electron Tunneling Spectroscopy. *Physical Review B* **53**, 11176–11185 (1996).

[64] R.F. Carvalha, R.S. Freire, L.T. Kubotaa, Polycrystalline Gold Electrodes: A Comparative Study of Pretreatment Procedures Used for Cleaning and Thiol Self-Assembly Monolayer Formation. *Electroanalysis* **17**, 1251–1259 (2005).

[65] C. Chidsey, D. Loiacono, T. Selator, S. Nakahara, STM Study of the Surface Morphology of Gold on Mica. *Surface Science* **200**, 45–66 (1988).

[66] C.E.D. Chidsey, D.N. Loiacono, Chemical Functionality in Self -Assembled Monolayers: Structural and Electrochemical Properties. *Langmuir* **6**, 682 (1990).

[67] C.D. Bain, E.B. Troughton, Y.-T. Tao, J. Evall, G.M. Whitesides, R.G. Nuzzo, Formation of Monolayer Films by the Spontaneous Assembly of Organic Thiols from Solution onto Gold. *Journal of the American Chemical Society* **111**, 321–335 (1989).

[68] H.O. Finklea, S. Avery, M. Lynch, Blocking Oriented Monolayers of Alkyl Mercaptans on Gold Electrodes. *Langmuir* **3**, 409–413 (1987).

[69] N.G. Woodard, G.P. Lafayatis, Fabrication and Characterization of Extremely Smooth Large Area Gold Surfaces. *Journal of Vacuum Science Technology A* **14**, 332–335 (1995).

[70] G.E. Poirier, Mechanism of Formation of Au Vacancy Islands in Alkanethiol Monolayers. *Langmuir* **13**, 2019–2026 (1997).

[71] G. LeLay, The Au/Si(111) Interface: Growth Mode, Energetics, Structural and Electronic Properties. *Journal of Crystal Growth* **54**, 551–557 (1981).

[72] U. Höpfner, H. Hehl, L. Brehmer, Preparation of Ordered Thin Gold Films. *Applied Surface Science* **152**, 259 (1999).

[73] B. Lüssem, S. Karthäuser, H. Haselier, R. Waser, The Origin of Faceting of Ultraflat Gold Films Epitaxially Grown on Mica. *Applied Surface Science* **249**, 197–202 (2005).

[74] X.-Y. Zheng, Y. Ding, L.A. Bottomley, D.P. Allison, R.J. Warmack, Discontinuous Gold Islands Films on Mica. *Journal of Vacuum Science Technology B* **13**, 1320–1324 (1995).

[75] J. DeRose, T. Thundat, L.A. Nagahara, S.M. Lindsay, Gold Grown Epitaxially on Mica: Conditions for Large Area Flat Faces. *Surface Science* **256**, 102–108 (1991).

[76] J. Perdereau, J.P. Biberian, G.E. Rhead, Adsorption and Surface Alloying of Lead Monolayers on (111) and (110) Faces of Gold. *J. Phys. F* **4**, 798–806 (1974).

[77] U. Harten, A. M. Lahee, J.P. Toennies, Ch. Wöll, Observation of a Soliton Reconstruction of Au(111) by High-Resolution Helium-Atom Diffraction. *Physical Review Letters* **54**, 2619–2622 (1985).

[78] B.G. Frederick und F.M. Leibsle und S. Haq und N.V. Richardson, Evolution of Lateral Order and Molecular Reorientation in the Benzoate/Cu(110) System. *Surface Review and Letters* **3**, 1523–1546 (1996).

[79] P.E. Laibinis und G.M. Whitesides, ω-Terminated Alkanethioate Monolayers on Surfaces of Copper Siver, and Gold Have Similar Wettabilities. *Journal of the American Chemical Society* **114**, 1990 (1992).

[80] P.E. Laibinis, G.M. Whitesides, D.L. Allara, Y.-T. Tao, A.N. Parikh, R.G. Nuzzo, Comparison of the Structures and Wetting Properties of Self Assembled Monolayers of n-Alkanethiols on the Coinage Metal Surfaces, Cu, Ag, Au. *Journal of the American Chemical Society* **113**, 7152–7167 (1991).

[81] D.S. Martin und R.J.Cole und P. Weightman, Effects of Ion bombardment on the Optical and Electronic Properties of Cu(110). *Physical Review B* **72**, 354081–354088 (2005).

[82] D.S. Martin, A. Maunder, P. Weightman, Thermal Behavior of the Cu(110) Surface Studied byReflection Anisotropy Spectroscopy and Scanning Tunneling Microscopy. *Physical Review B* **63**, 1554031–1554038 (2001).

[83] R.G. Nuzzo, D.L. Allara, Adsorption of Bifunctional Organic Disulfides on Gold Surfaces. *Journal of the American Chemical Society* **105**, 4481–4483 (1983).

[84] M.D. Porter, T.B. Bright, D.L. Allara, C.E.D. Chidsey, Spontaneously Organized Molecular Assemblies. 4. Structural Characterization of n-Alkyl Thiol Monolayers on Gold by Optical Ellipsometry, Infrared Spectroscopy, and Electrochemistry. *Journal of the American Chemical Society* **109**, 3559–3568 (1987).

[85] L. Strong, G.M. Whitesides, Structures of Self-Assembled Monolayer Films of Organosulfur Compounds Adsorbed on Gold Single Crystals: Electron Diffraction Studies. *Langmuir* **4**, 546–558 (1988).

[86] C.E.D. Chidsey, G.-Y. Liu, P. Rowntree, G. Scoles, Molecular Order at the Surface of an Organic Monolayer Studied by Low Energy Helium Diffraction. *Journal of Chemical Physics* **91**, 4421–4423 (1989).

[87] N. Camillone III, C.E.D. Chidsey, G.-Y. Liu, G. Scoles, Superlattice Structure at the Surface of a Monolayer of Octadecanethiol Self-Assembled on Au(111). *Journal of Chemical Physics* **98**, 3503–3511 (1993).

[88] C. Vericat, M.E. Vela, G.A. Benitez, J.A. Martin Gago, X. Torrelles, R.C. Salvarezza, Surface Characterization of Sulfur and Alkanethiol Self-Assembled Monolayers on Au(111). *Journal of Physics: Condensed Matter* **18**, R867–R900 (2006).

[89] P. Fenter, P. Eisenberger, K.S. Liang, Chain-Length Dependence of the Structures and Phases of $CH_3(CH_2)_{n-1}SH$ Self-Assembled on Au. *Physical Review Letters* **70**, 2447–1450 (1993).

[90] R.G. Nuzzo, F.A. Fusco, D.L. Allara, Spontaneously Organized Molecular Assemblies 3. Preparation and Properties of Solution Adsorbed Monolayers of Organic Disulfides on Gold Surfaces. *Journal of the American Chemical Society* **109**, 2358–2368 (1987).

[91] A.L. Deering, S.M. Van Lue, S.A. Kandel, Ambient-Pressure Vapor Deposition of Octanethiol Self-Assembled Monolayers. *Langmuir* **21**, 10260–10263 (2005).

[92] G.E. Poirier, Characterization of Organosulfur Molecular Monolayers on Au(111) Using Scanning Tunneling Microscopy. *Chemical Review* **97**, 1117–1127 (1997).

[93] H. Kondoh, C. Kodama, H. Sumida, H. Nozoye, Molecular Processes of Adsorption and Desorption of Alkanethiol Monolayers on Au(111). *Journal of Chemical Physics* **111**, 1175–1184 (1999).

[94] S.B. Darling, A.W. Rosenbaum, Y. Wang, S.J. Sibener, Coexistence of the $(23 \times \sqrt{3})$ Au(111) Reconstruction and a Striped Phase Self-Assembled Monolayer. *Langmuir* **2002**, 7462–7468 (2002).

[95] N. Camillone III, P. Eisenberger, T.Y.B. Leung, P. Schwartz, G. Scoles, G.E. Poirier, M.J. Tarlov, New Monolayer Phases of n-Alkane Thiols Self-Assembled on Au(111): Preparation, Surface Characterization, and Imaging. *Journal of Chemical Physics* **101**, 11031–11035 (1994).

[96] G.E. Poirier, E.D. Pylant, The Self-Assembly Mechanism of Alkanethiols on Au(111). *Science* **272**, 1145–1148 (1996).

[97] G.E. Poirier, Butanethiol Self-Assembly on Au(001): The (1x4) Au Missing Row, c(2x8) Molecular Lattice. *Journal of Vacuum Science Technology B* **14**, 1453–1459 (1996).

[98] C. Munera, E. Barrena, C. Ocal, Chain-Length Dependance of Metastable Striped Structures of Alkanethiols on Au(111). *Langmuir* (2005).

[99] E. Delamarche, B. Michel, H.A. Biebuyck, C. Gerber, Golden Interfaces: The Surface of Self-Assembled Monolayers. *Advanced Materials* **8**, 719–729 (1996).

[100] L.A. Bumm, J.J. Arnold, L.F. Charles, T.D. Dunbar, D.L. Allara, P.S. Weiss, Directed Self-Assembly to Create Molecular Terraces with Molecularly Sharp Boundaries in Organic Monolayers. *Journal of the American Chemical Society* **121**, 8017–8021 (1999).

[101] E. Delamarche, B. Michel, H. Kang, C. Gerber, Thermal Stability of Self-Assembled Monolayers. *Langmuir* **10**, 4103–4108 (1994).

[102] J.-P. Bucher, L. Santesson, K. Kern, Thermal Healing of Self-Assembled Organic Monolayers: Hexane- and Octadecanethiol on Au(111) and Ag(111). *Langmuir* **10**, 979–983 (1994).

[103] L. Müller-Meskamp, Charakterisierung von in einer SAM Hostmatrix immobilisierten funktionalen Molekülen mittels Rastersondenmethoden. Diploma thesis, RWTH Aachen, Germany, 2004.

[104] X. Xiao, B. Wang, C. Zhang, Z. Yang, M.M.T. Loy, Thermal annealing effect of alkanethiol monolayers on Au(111) in air. *Surface Science* **472**, 41–50 (2001).

[105] V. Ganesh, V. Lakshminarayanan, Self-Assembled Monolayers of Alkanethiols on Gold Prepared in a Hexagonal Lyotropic Liquid Crystalline Phase of Triton X-100/Water System. *Langmuir* **22**, 1561–1570 (2006).

[106] G. Yang und N.A. Amro und Z.B. Starkewolfe und G. Liu, Molecular-Level Approach to Inhibit Degradations of Alkanethiol Self-Assembled Monolayers in Aqueous Media. *Langmuir* **20**, 3995–4003 (2004).

[107] P. Fenter, A. Eberhardt, K.S. Liang, P. Eisenberger, Epitaxy and Chainlength Dependent Strain in Self-Assembled Monolayers. *Journal of Chemical Physics* **106**, 1600–1608 (1997).

[108] E. Delamarche, B. Michel, Ch. Gerber, D. Anselmetti, H.-J. Güntherodt, H. Wolf, H. Ringsdorf, Real-Space Observation of Nanoscale Molecular Domains in Self-Assembled Monolayers. *Langmuir* **10**, 2869–2871 (1994).

[109] G. Yang, G.Y. Liu, New Insights for Self-Assembled Monolayers of Organothiols on Au(111) Revealed by Scanning Tunneling Microscopy. *Journal of Physical Chemistry B* **107**, 8746 (2003).

[110] M.F. Danisüman, G. Bracco, G. Scoles, Structural Investigation of Monolayers Prepared by Deposition of (CH3S)2 on the (111) Face of Single-Crystal Gold. *Journal of Physical Chemistry B* **106**, 11771–11777 (2002).

[111] G.E. Poirier, M.J. Tarlov, The c(4x2) Superlattice of n-Alkanethiol Monolayers Self Assembled on Au(111). *Langmuir* **10**, 2853–2856 (1994).

[112] H.S. Kato, J. Noh, M. Hara, M. Kawai, An HREELS Study of Alkanethiol Self-Assembled Monolayers on Au(111). *Journal of Physical Chemistry B* **106**, 9655–9658 (2002).

[113] T. Fukuma, T. Ichii, K. Kobayashi, H. Yamada, K. Matsushige, Molecular-Scale Noncontact Atomic Force Microscopy Contrasts in Topography and Energy Dissipation on c(4x2) Superlattice Structures of Alkanethiol Self-Assembled Monolayers. *Journal of Applied Physics* **95**, 1222–1226 (2004).

[114] J. Noh, M. Hara, Molecular-Scale Growth Processes of Alkanethiol Self-Assembled Monolayers on Au(111). *RIKEN Review* **38**, 49–51 (2001).

[115] K. Kobayashi, H. Yamada, T. Horiuchi, K. Matsushige, The Molecular Arrangements of Alkanethiol Self-Assembled Monolayers on Au(111) Studied by Scanning Tunneling Microscopy. *Japanese Journal of Applied Physics* **37**, 6183–6185 (1998).

[116] B. Lüssem, L. Müller-Meskamp, S. Karthäuser, R. Waser, A New Phase of the c(4x2) Superstructure of Alkanethiols Grown by Vapor Phase Deposition on Gold. *Langmuir* **21**, 5256–5258 (2005).

[117] C.A. Alves, E.L. Smith, M.D. Porter, Atomic Scale Imaging of Alkanethiolate Monolayers at Gold Surfaces with Atomic Force Microscopy. *Journal of the American Chemical Society* **114**, 1222–1227 (1992).

[118] J. Noh, M. Hara, Final Phase of Alkanethiol Self-Assembled Monolayers on Au(111). *Langmuir* **18**, 1953–1956 (2002).

[119] V. De Renzi, R. Di Felice, D. Marchetto, R. Biagi, U. Del Pennino, A. Selloni, Ordered (3 x 4) High-Density Phase of Methylthiolate on Au(111). *J. Phys. Chem. B* **108**, 16–20 (2004).

[120] D. Fischer, A. Curioni, W. Andreoni, Dekanthiols on Gold: The Structure of Self-Assembled Monolayers Unraveled with Computer Simulations. *Langmuir* **19**, 3567–3571 (2003).

[121] M.V. Vargas, P. Giannozzi, A. Selloni, G.J. Scoles, Coverage-Dependent Adsorption of CH_3S and $(CH_3S)_2$ on Au(111): a Density Functional Theory Study. *J. Phys. Chem. B* **105**, 9509–9513 (2001).

[122] A. Riposan, G.-Y. Liu, Significance of Local Density of States in the Scanning Tunneling Microscopy Imaging of Alkanethiol Self-Assembled Monolayers. *Journal of Physical Chemistry B* **110**, 23926–23937 (2006).

[123] K.C. Langry, T.V. Ratto, R.E. Rudd, M.W. McElfresh, The AFM Measured Force Required to Rupture the Dithiolate Linkage of Thioctic Acid to Gold Is Less than the Rupture Force of a Simple Gold-Alkyl Thiolate Bond. *Langmuir* (2005).

[124] N. Camillone III, C.E.D. Chidsey, G.-Y. Liu, T.M. Putvinski, G. Scoles, Surface Structure and Thermal Motion of n-Alkane Thiols Self-Assembled on Au(111) Studied by Low Energy Helium Diffraction. *Journal of Chemical Physics* **94**, 8493–8501 (1991).

[125] J. Noh, H.S. Kato, M. Kawai, M. Hara, Surface Structure and Interface Dynamics of Alkanethiol Self-Assembled Monolayers on Au(111). *Journal of Physical Chemistry B* (2006).

[126] R.L. McCarley, D.J. Dunaway, R.J. Willicut, Mobility of the Alkanethiol-Gold(111) Interface Studied by Scanning Probe Microscopy. *Langmuir* **9**, 2775–2777 (1993).

[127] R.G. Nuzzo, B.R. Zegarski, L.H. Dubois, Fundamental Studies of the Chemisorption of Organosulfur Compounds on Au(111). Implications for Molecular Self-Assembly on Gold Surfaces. *Journal of the American Chemical Society* **109**, 733–740 (1987).

[128] P. Fenter, A. Eberhardt, P. Eisenberger, Self-Assembly on n-Alkyl Thiols as Disulfides on Au(111). *Science* **266**, 1216–1218 (1994).

[129] M.S. Yeganeh, S.M. Dougal, R.S. Polizzotti, P. Rabinowitz, Interfacial Atomic-Structure of a Self-Assembled Alkyl Thiol

Monolayer Au(111)- A Sum-Frequency Generation Study. *Physical Review Letters* **74**, 1811–1814 (1995).

[130] P. Fenter, F. Schreiber, L. Berman, G. Scoles, P. Eisenberger, M.J. Bedzyk, On the Structure and Evolution of the Buried S/Au Interface in Self-Assembled Monolayers: X-ray Standing Wave Results. *Surface Science* **412/413**, 213–235 (1998).

[131] C. Vericat, M.E. Vela, G.A. Andreasen, R.C. Salvarezza, F. Borgatti, R. Felici, T.-L. Lee, F. Renner, J. Zegenhagen, J.A. Martin-Gago, Following Adsorption Kinetics at Electrolyte/Metal Interfaces through Crystal Truncation Scattering: Sulfur on Au(111). *Physical Review Letters* **90**, 075506 (2003).

[132] Y. Cao, Q. Ge, D.J. Dye, L. Wang, Steric Effects on the Adsorption of Alkylthiolate Self-Assembled Monolayers on Au (111). *Journal of Physical Chemistry B* **107**, 3803–3807 (2003).

[133] M. Tachibana, K. Yoshizawa, A. Ogawa, H. Fujimoto, R. Hoffmann, Sulfur-Gold Orbital Interactions which determine the Structure of Alkanethiolate /Au(111) Self-Assembled Monolayer Systems. *The Journal of Physical Chemisty B* **106**, 12727–12736 (2002).

[134] L. Zhang, W.A. Goddard III, S. Jiang, Molecular Simulation Study of the c(4x2) Superlattice Structure of Alkanethiol Self-Assembled Monolayers on Au(111). *Journal of Chemical Physics* **117**, 7342–7349 (2002).

[135] M. Yu, N. Bovet, C.J. Satterley, S. Bengio, K.R.J. Lovelock, P.K. Milligan, R.G. Jones, D.P. Woodruff, V. Dhanak, True Nature of an Archetypal Self-Assembly System: Mobile Au-Thiolate Species on Au(111). *Physical Review Letters* **97**, 166102–1–166102–4 (2006).

[136] C. Schönenberger, J.A.M. Sondag-Huethorst, J. Jorritsma, L.G.J. Fokkink, What are the "Holes" in Self-Assembled Monolayers of Alkanethiols on Gold? *Langmuir* **10**, 611–614 (1994).

[137] O. Cavalleri, A. Hirstein, K. Kern, Ostwald Ripening of Vacancy Islands at Thiol Covered Au(111). *Surface Science* **340**, L960–L964 (1995).

[138] L.B. Picraux, C.D. Zangmeister, J.D. Batteas, Preparation and Structure of a Low-Density, Flat-Lying Decanethiol Monolayer from the Densely Packed, Upright Monolayer on Gold. *Langmuir* **22**, 174–180 (2006).

[139] L. Müller-Meskamp, B. Lüssem, S. Karthäuser, S. Prikhodovski, M. Homberger, U. Simon, R. Waser, Molecular Structure of Ferrocenethiol Islands Embedded Into Alkanethiol Self-Assembled Monolayers Studied by UHV-STM. *Physical status solidi (a)* **203**, 1448–1452 (2006).

[140] L. Müller-Meskamp, B. Lüssem, S. Karthäuser, M. Homberger, U. Simon, R. Waser, Self Assembly of Mixed Monolayers of Mercaptoundecyl-ferrocene and Undecanethiol studied by STM. *Journal of Physics: Conference Series* **61**, 852 (2007).

[141] M.C. Lennartz, Selbstorganisation von Alkanthiolen und Carboxylaten auf Au(111) und Cu(110)-Oberflächen. Diploma thesis, RWTH Aachen, 2007.

[142] Y. Cao, New Insights for Self-Assembled Monolayers of Organothiols on Au(111) Revealed by Scanning Tunneling Microscopy. *Journal of Physical Chemistry B* **107**, 3803–3807 (2003).

[143] V.B. Engelkes, J.M. Beebe, C. D. Frisbie, Length-Dependent Transport in Molecular Junctions Based on SAMs of Alkanethiols and Alkanedithiols: Effect of Metal Work Function and Applied Bias on Tunneling Efficiency and Contact Resistance. *Journal of the American Chemical Society* **126**, 14287–14296 (2004).

[144] E. Wierzbinski, K. Slowinski, In Situ Wiring of Single Molecules into an Electrical Circuit via Electrochemical Distance Tunneling Spectroscopy. *Langmuir* (2006).

[145] Y. Yasutake, Y. Azuma, K. Nagano, Y. Majima, Tunneling Current-Distance Characteristic of Scanning Vibrating Probe/ 1-Alkanethiol Self-Assembled Monolayer (SAM)/ Au (111) Structure. *Mat. Res. Soc. Symp. Proc.* **782**, 17–21 (2004).

[146] L. Müller-Meskamp, B. Lüssem, S. Karthäuser, R. Waser, Rectangular $(3 \times \sqrt{(}3))$Superlattice of a Dodecanethiol Self-Assembled Monolayer on Au(111) Observed by Ultra-High-Vacuum Scanning Tunneling Microscopy. *Journal of Physical Chemistry B* **109**, 11424–11426 (2005).

[147] T.J. Kealy, P.L. Pauson, A New Type of Organo-Iron Compound. *Nature* **168**, 1039–1040 (1951).

[148] G. Wilkinson, The Long Search for Stable Transition Metal Alkyls. In *Nobel Lecture*, 1973.

[149] R.R. Gagne, C.A. Koval, G.C. Lisensky, Ferrocene as Internal Standard for Electrochemical Measurements. *Inorganic Chemistry* **19**, 2854–2855 (1980).

[150] C.E.D. Chidsey, C.R. Bertozzi, T.M. Putvinski, A.M. Mujsce, Coadsorption of Ferrocene-Terminated and Unsubstituted Alkanethiols on Gold: Electroactive Self-Assembled Monolayers. *Journal of the American Chemical Society* **112**, 4301–4306 (1990).

[151] J.F. Smalley, S.W. Feldberg, C.E.D. Chidsey, M.R. Linford, M.D. Newton, Y.-P. Liu, The Kinetics of Electron Transfer through Ferrocene-Terminated Alkanethiol Monolayers on Gold. *Journal of Physical Chemistry* **99**, 13141–13149 (1995).

[152] C.E.D. Chidsey, Free-Energy and Temperature Dependance of Electron-Transfer at the Metal-Electrolyte Interface. *Science* **251**, 919–922 (1991).

[153] L.Y.S. Lee, T.C. Sutherland, S. Rucareanu, R.B. Lennox, Ferrocenylalkylthiolates as a Probe of Heterogeneity in Binary Self-Assembled Monolayers on Gold. *Langmuir* **22**, 4438–4444 (2006).

[154] K. Uosaki, Y. Sato, H. Kita, Electrochemical Characteristics of a Gold Electrode Modified with a Self -Assembled Monolayer of Ferrocenylalkanethiols. *Langmuir* **7**, 1510–1514 (1991).

[155] T. Auletta, F.C. van Veggel, D.N. Reinhoudt, Self-Assembled Monolayers on Gold of Ferrocene-Terminated Thiols and Hydroxyalkanethiols. *Langmuir* **18**, 1288–1293 (2002).

[156] J.P. Collman, N.K. Devaraj, C.E.D. Chidsey, Clicking Functionality onto Electrode Surfaces. *Langmuir* **20**, 1051–1053 (2004).

[157] T. Ohtsuka, Y. Sato, K. Uosaki, Dynamic Ellipsometry of a Self-Assembled Monolayer of a Ferrocenylalkanethiol during Oxidation-Reduction Cycles. *Langmuir* **10**, 3658–3662 (1994).

[158] A.S. Viana, L.M. Abrantes, G. Jin, S. Floate, R.J. Nichols, M. Kalaji, Electrochemical, Spectroscopic and SPM Evidence for the Controlled Formation of Self-Assembled Monolayers and Organised Multilayers of Ferrocenyl Alkyl thiols on Au(111). *Physical Chemistry, Chemical Physics* **3**, 3411–3419 (2001).

[159] X. Yao, J. Wang, F. Zhou, J. Wang, N. Tao, Quantification of Redox-Induced Thickness Changes of 11-Ferrocenylundecanethiol Self-Assembled Monolayers by Electrochemical Surface Plasmon Resonance. *Journal of Physical Chemistry B* **108**, 7206–7212 (2004).

[160] C.B. Gorman, R.L. Carroll, R.R. Fuierer, Negative Differential Resistance in Patterned Electroactive Self-Assembled Monolayers. *Langmuir* **17**, 6923–6930 (2001).

[161] A.V. Tivanski, G.C. Walker, Ferrocenylundecanethiol Self-Assembled Monolayer Charging Correlates with Negative Differential Resistance Measured by Conducting Probe Atomic Force Microscopy. *Journal of the American Chemical Society* **127**, 7647–7653 (2005).

[162] J. He, S.M. Lindsay, On the Mechanism of Negative Differential Resistance in Ferrocenylundecanethiol Self-Assembled Monolayers. *Journal of the American Chemical Society* **127**, 11932–11933 (2005).

[163] N.R. Armstrong, C. Carter, C. Donley, A. Simmonds, P. Lee, M. Brumbach, B. Kippelen, B. Domercq, S. Yoo, Interface Modification of ITO Thin Films: Organic Photovoltaic Cells. *Thin Solid Films* **445**, 342–352 (2003).

[164] Q. Li, S. Surthi, G. Mathur, S. Gowda, V. Misraa, T.A. Sorenson, R.C. Tenent, W.G. Kuhr, S. Tamaru, J.S. Lindsey, Z. Liu, D.F. Bocian, Electrical Characterization of Redox-Active Molecular Monolayers on SiO_2 for Memory Applications. *Applied Physics Letters* **83**, 198–201 (2003).

[165] J.K. Gimzewski, . Personal Communication at the ICN+T , 2006.

[166] B. Lüssem, L. Müller-Meskamp, S. Karthäuser, R. Waser, M. Homberger, U. Simon, STM Study of Mixed Alkanethiol/Biphenylthiol Self-Assembled Monolayers on Au(111). *Langmuir* **22**, 3021–3027 (2006).

[167] S. Wakamatsu, U. Akiba, M. Fujihira, Electronic Tunneling Through a Single Molecule Embedded in Self-Assembled Monolayer Matrices. *Colloids and Surfaces A* **198**, 785–790 (2002).

[168] M.T. Cygan, T.D. Dunbar, J.J. Arnold, L.A. Bumm, N.F. Shedlock, T.P. Burgin, L. Jones II, D.L. Allara, J.M. Tour, P.S.

Weiss, Insertion, Conductivity, and Structures of Conjugated Organic Oligomers in Self-Assembled Alkanethiol Monolayers on Au(111). *Journal of the American Chemical Society* **120**, 2721–2732 (1998).

[169] T. Ishida, W. Mizutani, H. Tokumoto, N. Choi, U. Akiba, M. Fujihira, Insertion Process and Electrical Conduction of Conjugated Molecules in n-Alkanethiol Self-Assembled Monolayers on Au(111). *Journal of Vacuum Science Technology A* **18**, 1437–1442 (2000).

[170] L. Li, S. Cheng, S. Jiang, Molecular-Scale Mixed Alkanethiol Monolayers of Different Terminal Groups on Au(111) by Low-Current Scanning Tunneling Microscopy. *Langmuir* **19**, 3266–3271 (2003).

[171] S.V. Arte, B. Liedberg, D.L. Allara, Chain Length Dependence of the Structure and Wetting Properties in Binary Composition Monolayers of OH- and CH3-Terminated Alkanethiolates on Gold. *Langmuir* **11**, 3882–3893 (1995).

[172] R.K. Smith, S.M. Reed, P.A. Lewis, J.D. Monnel, R.S. Clegg, K.F. Kelly, L.A. Bumm, J.E. Hutchison, P.S. Weiss, Phase Separation Within a Binary Self-Assembled Monolayer on Au(111) Driven by an Amide-Containing Alkanethiol. *Journal of Physical Chemistry B* **105**, 1119 (2001).

[173] L. Scudiero, D.E. Barlow, K.W. Hipps, Physical Properties and Metal Ion Specific Scanning Tunneling Microscopy Images of Metal(II) Tetraphenylporphyrins Deposited from Vapor onto Gold (111). *Journal of Physical Chemistry B* **104**, 11899–11905 (2000).

[174] C. Waldfried, D. Welipitya, C.W. Hutchings, H.S.V. de Silva, G.A. Gallup, P.A. Dowben, W.W. Paii, J. Zhang, J.F. Wendelken, N. M. Boag, Preferential Bonding Orientations of Ferrocene on Surfaces. *Journal of Physical Chemistry B* **101**, 9782–9789 (1997).

[175] P. Kruse, E.R. Johnson, G.A. DiLabio, R.A. Wolkow, Patterning of Vinylferrocene on H-Si(100) via Self-Directed Growth of Molecular Lines and STM-Induced Decomposition. *Nano Letters* **2**, 807–810 (2002).

[176] B. Voigtlaender, J. Myslivecek, . Personal Communication , 2006.

[177] K.-F. Braun, V. Iancu, N. Pertaya, K.-H. Rieder, S.-W. Hla, Decompositional Incommensurate Growth of Ferrocene Molecules on a Au(111) Surface. *Physical Review Letters* **96**, 246102 (2006).

[178] K. Wedeking, Z. Mu, G. Kehr, R. Fröhlich, G. Erker, L. Chi, H. Fuchs, Tetradecylferrocene: Ordered Molecular Array of an Organometallic Amphiphile in the Crystal and in a Two-dimensional Assembled Structure on a Surface. *Langmuir* **22**, 3161–3165 (2006).

[179] K. Wedeking, Z. Mu, G. Kehr, J.C. Sierra, C.M. Lichtenfeld, S. Grimme, G. Erker, R. Froehlich, L. Chi, W. Wang, D. Zhong, H. Fuchs, Oligoethylene Chains Terminated by Ferrocenyl End Groups: Synthesis, Structural Properties, and Two-Dimensional Self-Assembly on Surfaces. *Chemistry, a European Journal* **12**, 1618–1628 (2006).

[180] Y.-T. Kim, R.L. McCarley, A.J. Bard, Scanning Tunneling Microscopy Studies of Au(111) Derivatized with Organothiols. *Journal of Physical Chemistry* **96**, 7416–7421 (1992).

[181] J D. Dunitz, L.E. Orgel, A. Rich, The Crystal Structure of Ferrocene. *Acta Crystallographica* **9**, 373–375 (1956).

[182] P. Seiler, J.D.Dunitz, A New Interpretation of the Disordered Crystal Structure of Ferrocene. *Acta Crystallographica* **B35**, 1068 (1979).

[183] S.W. Han, H. Seo, Y.K. Chung, K. Kim, Electrochemical and Vibrational Spectroscopic Characterization of Self-Assembled Monolayers of 1,1'-Disubstituted Ferrocene Derivatives on Gold. *Langmuir* **16**, 9493–9500 (2000).

[184] G.R. Knox, P.L. Pauson, Ferrocene Derivatives .7. Some Sulfur Derivatives. *Journal of the American Chemical Society* **692** (1958).

[185] N. Camillone III, T.Y.B. Leung, P. Schwartz, P. Eisenberger, G. Scoles, Chain Length Dependence of the Striped Phases of Alkanethiol Monolayers Self-Assembled on Au(111): An Atomic Beam Diffraction Study. *Langmuir* **12**, 2737–2746 (1996).

[186] R. Staub, M. Toerker, T. Fritz, T. Schmitz-Huebsch, F. Sellam, K. Leo, Flat Lying Pin-Stripe Phase of Decanethiol Self-Assembled Monolayers on Au(111). *Langmuir* **14**, 6693–6698 (1998).

[187] P.G. Piva, G.A. DiLabio, J.L. Pitters, J. Zikovsky, M. Rezeq, S. Dogel, W.A. Hofer, R.A. Wolkow, Field Regulation of Single-Molecule Conductivity by a Charged Surface Atom. *Nature* **435**, 658–661 (2005).

[188] S. Wakamatsu, U. Akiba, M. Fujikira, Electronic Tunneling through Self-Assembled Monolayers of Phenylene Oligomers on Au(111). *Japanese Journal of Applied Physics* **41**, 4998–5002 (2002).

[189] V.N. Nemykin, R.G. Hadt, Influence of Hartree-Fock Exchange on the Calculated Moessbauer Isomer Shifts and Quadrupole Splittings in Ferrocene Derivatives Using Density Functional Theory. *Inorganic Chemistry* **45**, 8297–8307 (2006).

[190] Y.S. Sohn, D.N. Hendrickson, H.B. Gray, Electronic Structure of Metallocenes. *Journal of the American Chemical Society* **93**, 3603–3612 (1971).

[191] S.M. Barlow, R. Ravel, Complex Organic Molecules at Metal Surfaces: Bonding, Organisation and Chirality. *Surface Science Reports* **50**, 201–341 (2003).

[192] L. Pranger, R. Tannenbaum, Self-Assemby of 1,4-Phenylene Diisocyanide and Terephthalic Acid on Ni, Cu and Pt. *Journal of Colloid and Interface Science* **292**, 71–78 (2005).

[193] N. Atodiresei, *First Principles Theory of Organic Molecules on Metal surfaces : Formate, 3-Thiophene-carboxylate and Glycinate on Cu(110).* Ph.D. thesis, RWTH-Aachen, 2005.

[194] P. Stone, S. Poulston, R.A. Bennet, N.J. Price, M. Bowker, An STM, TPD and XPS Invesigation of Formic Acid Adsorption on the Oxygen-Precovered c(6x2) Surface of Cu(111). *Surface Science* **418**, 71–83 (1998).

[195] J. Lee, D.B. Dougherty, J.T. Yates, Penyl Species Formation and Preferential Hydrogen Abstraction in the Decomposition of Chemisorbed Benzoate on Cu(110). *Journal of Physical Chemistry B* **110**, 9939–9946 (2006).

[196] B.G. Frederick, Q. Chen, F.M. Leibsle, M.B. Lee, K.J. Kitching, N.V. Richardson, Long-Range Periodicity in c(8x2) Benzoate/Cu(110): a Combined STM, LEED, HREELS Study. *Surface Science* **394**, 1–25 (1997).

[197] O. Karis, J. Hasselstroem, N. Wassdahl, M. Weinelt, A. Nilsson, M. Nyberg, L.G.M. Petterson, J. Stoehr, M.G. Samant, The Bonding of Simple Carboxylic Acids on Cu(110). *Journal of Chemical Physics* **112**, 8146–8155 (2000).

[198] B.G. Frederick, Q. Chen, F.M. Leibsle, S.S. Dhesi, N.V. Richardson, Electron-Stimulated Disordering in c(8x2) Benzoate/Cu(110): a Combined STM, LEED and HREELS Study. *Surface Science* **394**, 26–46 (1997).

[199] Q. Chen, C.C. Perry, B.G. Frederick, N.V. Richardson, Structural Aspects of the Low-Temperature Deprotonation of Benzoic Acid on Cu(110) Surfaces. *Surface Science* **446**, 63–76 (2000).

[200] D.S. Martin, R.J. Cole, S. Haq, Creating a Functionalized Surface: The Adsorption of Terephthalic Acid onto Cu(110). *Physical Review B* **66**, 1554271–1554278 (2002).

[201] S. Stepanow, T. Strunskus, M. Lingenfelder, A. Dimitriev, H. Spillman, N. Lin, J.V. Barth, C. Woell, K. Kern, Deprotonation-Driven Phase Transformations in Terephthalic Acid Self-Assembly on Cu(100). *Journal of Physical Chemistry B* **108**, 19392–19397 (2004).

[202] J. Lahann, S. Mitragotri, T. Tran, H. Kaido, J. Sundaram, I.S. Choi, S. Hoffer, G. A. Somorjai, R. Langer, A Reversibly Switching Surface. *Science* **299**, 371–374 (2003).

Schriften des Forschungszentrums Jülich
Reihe Information / Information

1. **Ferrocenes as Potential Building Blocks for Molecular Electronics**
   Self-Assembly and Tunneling Spectroscopy
   by L. Müller-Meskamp (2008), 153 pages
   ISBN: 978-3-89336-509-8

The fast and continous development of modern information technology has reached extreme dimensions of density and performance. To enhance the properties of classical silicon based semiconductor technologies, new concepts and materials become increasingly important. One promising technology is the use of organic electronics starting from bulk property-based organic light-emmission and cheap, printable electronics on flexible substrates. Upon further development, organic electronics have the potential to be used in highly ordered organic thin films and new quantum effect based circuits, employing the properties of single molecules. In this thesis self-assembly as a nanoscale integration method and the resulting structural properties of monolayers are studied for alkanethiols and ferrocenylalkanethiols on gold and for carboxylates on copper. The structural properties of these monolayers have been studied with molecular resolution by scanning tunneling microscopy, gaining new insights into molecular self-assembly. Especially mixed systems of alkanethiols and the electroactive ferrocenylalkanethiols have been studied in detail, achieving a better understanding of the layer formation and a thorough characterization of the electronic behaviour of embedded ferrocenylalkanethiols.

Band | Volume 1
ISBN 978-3-89336-509-8

JÜLICH
FORSCHUNGSZENTRUM